A computational modeling of aortic adaptation to vascular lesions

Živić, Josip

University of Zagreb

Faculty of Mechanical Engineering and Naval Architecture

Josip Živić

A COMPUTATIONAL MODELING OF AORTIC ADAPTATION TO VASCULAR LESIONS

DOCTORAL DISERTATION

Zagreb, 2024.

Sveučilište u Zagrebu
Fakultet strojarstva i brodogradnje

Josip Živić

RAČUNALNO MODELIRANJE ADAPTACIJE AORTE PRI POJAVI VASKULARNIH LEZIJA

DOKTORSKI RAD

Mentor:
Prof. dr. sc. Igor Karšaj

Zagreb, 2024.

BIBLIOGRAPHY DATA

UDC: 616.132:519.6

Key words: abdominal aortic aneurysm, intraluminal thrombus, growth and remodeling, fluid-solid growth, blood flow; FEAP®, OpenFOAM®.

Scientific area: Technical sciences
Scientific field: Mechanical engineering
Institution: Faculty of Mechanical Engineering and Naval
Thesis supervisor: Dr. sc. Igor Karšaj, Full professor

Number of pages: 116

Number of pages (in total): 153

Number of figures: 53

Number of tables: 4

Number of references: 107

Date of examination: January 9, 2025.

Thesis defense committee:

Dr. sc. Željko Tuković, Full professor - *Chairman of the defense commission*

Dr. sc. Mislav Vrsalović, Full professor – *member*

Dr. sc. Lana Virag, Assistant professor - *member*

Archive: Faculty of Mechanical Engineering and Naval Architecture

ACKNOWLEDGMENTS

I want to express my sincere gratitude to my supervisor, Prof. Igor Karšaj, for his trust and for giving me the opportunity to work under his guidance. His support, encouragement, and constructive feedback have been invaluable throughout these years. In addition, I would like to thank prof. Željko Tuković, prof. Mislav Vrsalović and assistant prof. Lana Virag for their valuable feedback and time spent reviewing this thesis.

I would like to express my deep appreciation to Lana, Nino, and the rest of our lab group for their invaluable help, support, and insightful discussions during the writing of this thesis and throughout work at the University. They were a huge part of it! I also extend my gratitude to prof. Tuković and Ivan Batistić for their contributions to the "incompressible" section of the thesis.

Many thanks go to my “Pan-Pek” friends, as well as Ivana, Toni, and others who made challenging days brighter with their company during lunch and coffee breaks at the university. I am also grateful to my 'Parkside' friends for the great times we've shared over the years, as well as to many others who have supported me along the way with their advice, encouragement, and long conversations.

I have to mention my Invers prog bandmates for the music and magic, the 3B JJ club and the most powerful group of friends, as well as Moto Gymkhana Croatia and the fastest CBR racing team from CZ!

For the end, my biggest thanks goes to my mother, father, and brother for their continuous patience, love, and support during all my life and studies. I could not achieve this without you, and I will be forever grateful.

SPECIAL ACKNOWLEDGMENT

I wish to express my sincere gratitude to the Croatian Science Foundation for supporting the research conducted in this thesis through the project “Numerical assessment of an uncomplicated type B aortic dissection rupture risk” (IP-2020-02-401, I. Karšaj) and the project Training of New Doctoral students (DOK--2018-01-5224).

Josip Živić

Zagreb, April 2024

CONTENTS

LIST OF FIGURES

LIST OF TABLES

NOMENCLATURE

Blood vessel modeling

Mark	Description
a, b, c, d, e	Elastin degradation parameters
C(s)	Net ratio of vasoconstrictors
C	Stiffness of the wall
$\mathrm{C},\ \mathrm{C}^{k}_{n(\tau)}$	Cauchy-Green tensors
$c_1^k, c_2^k, c_3^k, c_4^k, c_e$	Material parameters
d_1, d_2, d_3	Neck diameters
$D_{\max}$	Maximal diameter
Ddr	Diameter-diameter ratio
$\mathbf{e}_\theta$	Unit vector in circumferential direction
$f_1(s),\ f_2(z),\ f_3(\vartheta)$	Elastin degradation over time, in axial and circumferential direction
$\mathrm{F},\ {}^{s}_{0}\mathrm{F}, \mathrm{F}^{k}_{n(\tau)}$	Deformation gradient
$\mathbf{G}^k_h$	Homeostatic prestretch of fiber *k*
G^k	Scalar value of fiber prestretch
$\mathbf{G}^k$	Prestretch tensor of constituent *k*
h	Wall thickness
h_1, h_2, h_3	Heights for neck diameters
H	Aneurysmal height
$H_{D_{\max}}$	Maximal diameter height
$H_{\sigma_{22,\max}}$	Maximal circumferential stress height
I_1	First invariant (trace) of Cauchy-Green tensor
I_4	Forth invariant of Cauchy-Green tensor
K	Decay parameter
K^k_q	Rate-type parameter of mass removal for const *k*

Mark	Description
K_σ^k	Rate-type parameters of stress-driven mass production
K_σ^c	Stress-mediated gain parameter
K_C^k	Rate-type parameters of gain-type rate parameters
k_1	Stress-like parameter
$k_{1,\mathrm{lum}}$, $k_{1,abl}$	Stiffness parameters for luminal and abluminal layers
k_2	Dimensionless material parameter
L	Aneurismal length
m_B^k	Basal production rate
$\mathbf{m}^k$	Unit vector that represents the orientation of the fiber
$\dot{m}^k$	Mass production of each constituent k
$q^k(\mathrm{s}-\tau)$	Survival function
Q^e	Elastin degradation function
$Q^k(\mathrm{s})$	Survival function for mass existing in the initial G&R time
r	Pearson's correlation coefficient
r_i	Inner radius
$r_{\max}$	Maximal radius
s_f	G&R time of aneurysm formation
S	Aneurismal surface area
$r_{\max}$	Maximal inner radius
T	Aneurismal tortuosity
T_m	Maximal actively generated stress
V_{ILT}	ILT Volume
W^k	Specific stored energy function
W_{ILT}	ILT strain energy
z_{down} , z_{up}	Maximum and minimum height of elastin degradation
Δz_{MED}	Elastin degradation belt size

Mark	Description
ϑ	Circumferential direction
λ_M	Circumferential stretch
λ_0	Circumferential stretch when the active stress is zero,
μ	stress-like parameter
ρ	Density
$\boldsymbol{\sigma}^k$	Cauchy stress
$\boldsymbol{\sigma}_{\mathrm{h}}$	homeostatic stress
$\left\|\boldsymbol{\sigma}_{\mathrm{h}}^k\right\|$	Homeostatic state in wall stress
$\sigma_{22,\max}$	Maximal stress in radial direction
σ^{active}	Active stress contribution from smooth muscle
τ_w	Wall shear stress
$\tau_{w,h}$	Homeostatic value of wall shear stress
$\tau_{1/2}^e$	Elastin half-life
$\phi_{\mathrm{rem}}^e = 0.2$	Remaining elastin after degradation
ϕ^{SMC}	Mass fraction of muscle cells
Φ	Elastic degradation function

Computer fluid simulation and FVM

Mark	Description
a	Coefficient for Bird-Carreau viscosity model
C_μ	Turbulence constant
f	Volume force
I	Turbulence intensity
J	Jacobian matrix
k	Turbulence kinetic energy
L	Reference length scale
m	Constant for Casson viscosity model
p	Pressure
$\mathbf{u}$	Velocity
$\|\mathbf{u}\|$	Initial velocity magnitude
γ	Shear rate
$\dot{\gamma}$	Shear rate deformation
μ	Dynamic viscosity
ν_0 , ν_∞	Kinematic viscosity at zero and infinite shear for BC
$\nu_{\min}$, $\nu_{\max}$	Minimum and maximal kinematic viscosities for Casson model
ρ	Density
τ	Shear stress
τ_0	Threshold stress
ω	Turbulence dissipation

Incompressibility

Mark	Description
C	Material parameter
$p(\xi)$	Pressure change in element
u	Displacement
W	Free deformation energy
$\theta(\xi)$	Volume change in element
μ	Compressibility with a constant distribution
ν	Poisson's factor
σ^{α} , ε^{α}	Nonphysical values in incompressibility equation
$\phi_{\alpha}(\xi)$, $\psi_{\alpha}(\xi)$	Interpolation for finite element

ABBREVIATIONS

Acronym	Full description
AAA	Abdominal aortic aneurysm
BC	Bird-Carreau
CFD	Computational fluid dynamics
CMP	Composite morphological parameter
CT	Computed Tomography
CY	Carreau-Yasuda
CVD	Cardiovascular diseases
3D	Three Dimension
ECAP	Endothelial cell activation potential
FSG	Fluid solid growth
FSI	Fluid structure interaction
FVM	Finite volume method
G&R	Growth and Remodeling
GRPI	Geometrical rupture potential index
HGO	Holzapfel-Gasser-Ogden
HIST	Family history
ILT	Intraluminal thrombus
NAL	Normalized aneurysm length
NORD	Normalized local diameter
OSI	Oscillatory shear index
PISO	Pressure implicit split operator
PLAP	Platelet Activation Potential
RANS	Reynolds averaged Navier-Stokes equations
RBC	Red blood cells
RPI	Rupture potential index
RRT	Relative residence time
SEM	Scanning electron microscopy
SEX	Patient's gender
SIMPLE	Semi implicit method for pressure linked equations

SMC	Smooth muscle cells
SST	shear stress transport
TASR	time averaged shear rate
TAWSS	Time averaged wall shear stress
TFP	Thrombus formation potential
WSS	Wall shear stress

ABSTRACT

An abdominal aortic aneurysm (AAA) is just one of several vascular abnormalities, including aneurysmal changes, dissection, and atherosclerosis. AAA refers to a localized enlargement of the blood vessel, exceeding 50% of its diameter, typically resulting from an imbalance in the production and degradation of elastin and collagen. More than 75% of AAA exhibit intraluminal thrombus (ILT), which impacts the aneurysm in multiple ways. Thrombus aids in reducing peak wall stress within the aneurysm, yet it also weakens its structural integrity by degrading the aortic wall. When dealing with vascular abnormalities, a tool that guides clinicians in determining the appropriate treatment based on available diagnostic assessments and medical history would prove invaluable. This work is primarily dedicated to developing a comprehensive Fluid Solid Growth (FSG) model aimed at studying aortic diseases, with a specific focus on AAA. The initial component of the model involves applying the Growth and Remodeling (G&R) model to both the blood vessel and intraluminal thrombus. The criteria for thrombus deposition rely on the analysis of blood flow patterns and the corresponding stress. A crucial aspect of this research centers around seeking an optimal criterion for the ILT deposition, addressing a substantial gap in current research. A Computational Fluid Dynamics (CFD) model is utilized for blood analysis, incorporating diverse rheological properties. The integration of these two components is performed iteratively at each time step, ensuring the generation of authentic and precise results. Both the blood vessel and ILT exhibit incompressibility, and this is incorporated into the G&R model. Another problem is that AAAs frequently remain asymptomatic until they rupture, an event associated with a significant mortality risk. Despite numerous histological, experimental, and computational endeavors aimed at identifying more dependable rupture criteria, the prediction of rupture and medical interventions still heavily rely on factors such as maximum diameter and the clinical expertise of healthcare professionals. In the final phase of this study, numerous cases of AAA underwent comprehensive examination to establish an optimal aneurysm rupture potential index. This index is intended to support healthcare professionals in predicting the likelihood of rupture, a potentially life-threatening event.

Key words: Abdominal Aortic Aneurysm, Intraluminal Thrombus, Growth and Remodeling, Fluid-Solid Growth, Blood flow; FEAP®, OpenFOAM®.

PROŠIRENI SAŽETAK

UVOD

Aorta je najveća arterija u ljudskom tijelu te igra ključnu ulogu u kardiovaskularnom sustavu. Smještena na izlazu iz lijeve klijetke srca, aorta djeluje kao glavni distribucijski kanal, prenoseći krv obogaćenu kisikom i hranjivim tvarima iz srca do ostalih dijelova tijela. Zdrava arterijska stijenka se odlikuje svojom kompleksnom troslojnom strukturom, koja se sastoji od intime, medije i adventicije. Svaki od ovih slojeva ima specifičnu ulogu i sastav, omogućavajući aorti da efikasno obavlja svoju funkciju, ali i pruža otpornost i elastičnost potrebnu za održavanje stabilnog protoka krvi kroz kardiovaskularni sustav.

Unutarnja ovojnica (intima) sastoji se od jednog sloja endotelnih stanica (tj. endotelija). Srednja ovojnica (medija) odvojena je od unutarnje i vanjske ovojnice unutarnjim i vanjskim elastičnim lamelama te sadrži stanice glatkog mišića, elastin i kolagen. Vanjska ovojnica (adventicija) sastoji se uglavnom od kolagena i elastina. Također sadrži različite stanice poput fibroblasta, koji osiguravaju konstantnu produkciju i obnovu kolagena. Endotel je osjetljiv na promjene u protoku krvi, odnosno na posmična naprezanja (WSS) koji se stvara nastrujavanjem krvi na stijenku. Promjena WSS-a može povećati proizvodnju vazoaktivnih molekula koje utječu na kontrakciju glatkih mišića kako bi se održala homeostatska vrijednost WSS-a kratkoročno ili kako bi se obnovilo glatko mišićno tkivo dugoročno.

Aorta može biti zahvaćena različitim bolestima ili lezijama, a jedno od značajnih stanja su aneurizme abdominalne aorte (AAA). To je fokalna dilatacija krvne žile za više od 50% u promjeru. Medicinska struka klasificira aortu aneurizmom ako njezin promjer prelazi 30 mm. Poznato je da većina aneurizmi sadrži intraluminalni tromb (ILT) [1], trombotični materijal koji se obično nakuplja unutar područja proširene aorte, posebno u infrarenalnom segmentu. Formiranje ILT-a započinje kada je endotel oštećen za 80% ili više [2], [3]. Endotel, koji reagira na promjene u protoku krvi, obično je oštećen zbog povišenog posmičnog naprezanja (WSS) na stijenci aorte. Taloženje ILT-a može se koncipirati kao proces u četiri faze, kako je navedeno u [4]. U prvoj fazi (vrlo svjež), cijeli ILT uglavnom se sastoji od eritrocita iz krvotoka

pomiješanih s nekom labavom mrežom fibrina, leukocita ili trombocita u niskim postotcima. U drugoj fazi (mlad), mreže fibrina počinju rasti kao veliki postotak labave mreže fibrina, kao i eritrocita. U trećoj (intermedijalnoj) i četvrtoj (kasnijoj) fazi taloženja ILT-a, eritrociti i proteini se razgrađuju, ostavljajući kondenzirane mreže fibrina i guste ostatke proteina. Ove kasnije faze nemaju značajnu važnost za trenutno područje istraživanja, koje se uglavnom bavi formiranjem i početnim stadijem razvoja aneurizmi, te obično ne napreduju do kasnijih faza.

Glavni cilj ovog istraživanja je formulacija sveobuhvatnog i naprednog *fluid-solid-growth* (FSG) modela, koji je zamišljen kao potencijalno revolucionaran alat za medicinske stručnjake, posebno u području kardiologije, pružajući im sofisticirani uvid i potencijalnu strategiju za liječenje bolesti poput AAA. Inovativni aspekt FSG modela leži u njegovoj sposobnosti da integrira dinamički napredak tromba u aneurizmi, uzimajući u obzir njegovo nekompresibilno ponašanje i iterativne parametre protoka krvi. Ovaj iterativni pristup odražava stvarne obrasce rasta aneurizmi, nudeći prediktivnu sposobnost koja ima potencijal informirati o nužnim pravovremenim intervencijama i time značajno doprinijeti smanjenju smrtnosti povezane s kardiološkim bolestima.

Cjeloviti FSG model mora uključivati cijeli proces razvoja aorte do AAA u kojoj je taložen tromb, koristeći *Growth and remodelling* (G&R) teoriju, koja je implementirana u numerički 3D model. G&R teorija obuhvaća teorije rasta i razvoja tkiva, gdje teorija rasta govori da tkivo nije materijalno konstantno, već mijenja masu, odnosno da se istovremeno odvijaju procesi produkcije i degradacije. Teorija razvoja objašnjava kako zasebni elementi tkiva, iako su povezani u jednu strukturu te imaju jednake pomake, imaju različite vrijednosti naprezanja, što dovodi do različitih deformacija u njihovim elementima. Zbog prisutnih velikih deformacija i nelinearnog ponašanja, numeričko modeliranje krvnih žila vrlo je izazovan zadatak. Također, nužno je uzeti u obzir nestlačivost krvne žile kako ne bi došlo do pogreške modela. Razumijevanje kompleksnog procesa rasta i razvoja AAA nije moguće bez utjecaja strujanja krv i zbog njenog velikog utjecaja na morfologiju AAA, te još većeg utjecaj na složeni proces taloženja tromba. Proces formiranja tromba se analizira pomoću parametara koji direktno ovise o strujanju krvi kroz lumen, te se ova analiza vrši korištenjem C*omputer Fluid Dynamics* (CFD) simulacija. Iterativni proces rasta AAA i taloženja ILT-a iterativno se analizira nakon svakog srčanog ciklusa, te sveobuhvatni model simulira interakciju strujanja krvi i stijenke žile, zajedno

tvoreći FSG model. Ideja ovog istraživanja je popuniti praznine u području istraživanja koje trenutno postoje, razviti sveobuhvatni FSG model koji može opisati razvoj lezija na aorti s posebnim naglaskom na AAA, čime se stvara novi okvir za razumijevanje i liječenje ovih bolesti.

Dob, muški spol, hipertenzija, pušenje, kardiovaskularni i plućni poremećaji samo su neki od faktora rizika za razvoj AAA, iako patofiziologija još uvijek nije do kraja shvaćena. Osim toga, AAA često mogu biti asimptomatska do rupture, čiji je ishod popraćen velikom stopom smrtnosti. Predviđanje mogućnosti rupture i medicinska intervencija i dalje se temelje prvenstveno na maksimalnom promjeru i iskustvu kliničara, unatoč raznim histološkim, eksperimentalnim i računalnim naporima da se pronađu pouzdaniji kriteriji za rupturu. Osim toga, trenutačno korišteni kriteriji ne pružaju dovoljno informacija o stvarnoj potrebi za kirurškim zahvatom. Iako su studije koje procjenjuju rupturu aneurizme na temelju geometrijskih karakteristika s CT snimkama [5] pokazale neke obećavajuće rezultate, još uvijek se ne primjenjuju u praksi. Osim toga, neki parametri navedeni u dosadašnjim istraživanjima teško se mjere i mogu pružiti pogrešne informacije ukoliko se nepravilno upotrijebe.

PREGLED LITERATURE

G&R

Mehanika krvnih žila kompleksno je područje koje postavlja izazove u matematičkom modeliranju zbog složene prirode stijenke arterije, kao i svog nelinearnog, anizotropnog i pseudoelastičnog ponašanja. Prvi G&R model predstavio je Rodriguez sa suradnicima [6], čime je omogućio ključan napredak u biomehaničkom razumijevanju promjena tkiva u pogledu mase (rasta) i promjene u strukturi (remodeliranje). Njegov model predložio je opću kontinuiranu formulaciju za kinematski rast mekih tkivima, ističući ključni utjecaj mehaničkog stresa. Humphrey i Rajagopal [7] dali su značajan doprinos području biomehanike uvođenjem modela spregnutih smjesa za G&R teoriju mekih tkiva. Prema tome, cjelovitu masu čini svaki pojedinačni gradivni element koji nastaje u zasebno vrijeme, te mogu imati zasebne vrijednosti naprezanja ali uz to imaju zajedničke vrijednosti deformacija koje su jednake deformaciji smjese. Također, njihov model se fokusira na adaptivne mehanizme kao odgovor na mehaničke podražaje svih pojedinih konstituenata. Holzapfel i suradnici [8] razvili su hiperelastični konstitutivni model (HGO model) za arterijske stijenke koji uzima u obzir promjene u

elastičnim svojstvima uzrokovane rastom. Model koristi formulaciju ojačanu vlaknima, prema kojoj se pretpostavlja da je arterijski zid sastavljen od matrice i udruženih kolagenskih vlakana čija se orijentacija i distribucija mogu mijenjati zbog rasta i razvijanja. Holzapfelov model korišten je u brojnim studijama kako bi se istražili učinci različitih čimbenika poput starenja, hipertenzije i aneurizme na mehanička svojstva i rast arterijskih stijenki. Valentin je sa suradnicima [9] prvi implementirao model spregnutih smjesa u 3D kôd konačnih elemenata, ističući njegov potencijal za modeliranje različitih tkiva i bolesti, uključujući ozdravljenje tetiva, miokardijalnu hipertrofiju i prilagodbe arterija. Karšaj i suradnici [10] postigli su značajan napredak razvojem 3D G&R modela koji omogućuje detekciju promjene u geometriji i strukturi arterija kao odgovor na utjecaj hemodinamike, uključujući protok krvi i tlak. Horvat i suradnici [11] su proširili taj model uključivanjem troslojnog modela arterije te ga je kasnije implementirao u 3D kôd konačnih elemenata. Time je omogućio sveobuhvatne analize promjena u radijalnom, aksijalnom i cirkularnom smjeru unutar aksimetričnog i asimetričnog računalnog modela AAA. Model je korišten za ispitivanje utjecaja disperzije kolagena na ishod AAA [12], te utjecaja geometrijskih parametara modela na morfologiju naprezanja u stijenci i vjerojatnost rupture [13], što je kasnije prošireno kako bi se opisao proces taloženja tromba [14]. Cyron i suradnici [15] predstavili su novi homogeni model koji kombinira kinematički model s modelom spregnutih smjesa kako bi se dobio novi G&R model.

ILT

Ranih 1990-ih, Inzoli i suradnici [16] su predložili novi koncept sugerirajući da tromb može djelovati kao zaštitna barijera od naprezanja na stijenci aorte, smanjujući tako rizik od rupture aneurizme. Naknadna istraživanja [17], [18], [19] pružila su daljnje dokaze koji potvrđuju utjecaj tromba na čvrstoću aorte. S druge strane, nedavna istraživanja [20], [21] pokazala su proteolitičku aktivnost tromba, otkrivajući njegovu sposobnost da razgrađuje i oslabljuje stijenku aorte. Nakon opsežnih testova uniaksijalnog istezanja, Wang i suradnici [22] su utvrdili da ILT pokazuje izotropne karakteristike s nehomogenom strukturom, pokazujući pojačanu čvrstoću i krutost unutar luminalne regije, koristeći dvoparametarski, izotropni model materijala. Daljnje poboljšanje predstavio je Tong sa suradnicima [4], koji su pokazali jasne naznake mehaničke anizotropije u nekoliko luminalnih slojeva, sugerirajući da luminalni sloj ILT-a općenito nije izotropan. Virag i suradnici [23] razvili su 3D numerički model AAA, koji, za razliku od prethodnih računalnih modela koji su se fokusirali isključivo na mehaniku stijenke, integrira biomehanički, mehaničkobiološki te biokemijski model stijnke s uključenim modelom tromba. Horvat i suradnici [14] proširili su ranije predloženi model aneurizme

dodajući model tromba, koristeći 3D G&R model konačnih elemenata uz teoriju spregnutih sila.

CFD

Strujanje krvi igra ključnu ulogu u taloženju tromba, te je samim time ključno za istraživanje patogeneze različitih kardiovaskularnih bolesti, prije svega aneurizme. Zambrano i Byron [24] su među prvima koji su istraživali utjecaj TAWSS-a na formiranje tromba, te su zaključili da niske i srednje vrijednosti potiču njegovo formiranje i predložili kritične vrijednosti. Također su pokazali da brzina rasta aneurizme direktno utječe na brzinu rasta tromba, te da aneurizme s trombom imaju niže vrijednosti TAWSS-a, potvrđujući ovisnost taloženja tromba i TAWSS-a. DiAchille i suradnici [25] uveli su oscilacijski indeks smičnog naprezanja (OSI) i potencijal aktivacije endotelnih stanica (ECAP) kao dva dodatna parametra za taloženje tromba. Međutim, za sada ne postoje kritične vrijednosti za praktičnu uporabu i numerički model, što predstavlja nedostatak u istraživanju. U najnovijem istraživanju, DiAchille i suradnici [26] su predstavili novu, kompleksnu fenomenološku metriku, potencijal stvaranja tromba (TFP), koja se može koristiti kao napredni parametar u predviđanju formiranja tromba u određenom aneurizmalnom području.

FSG

Humphrey i Taylor [27] prvi su istaknuli nedostatke u postojećim istraživanjima, naglašavajući potrebu za razvojem nove klase modela te su predložili novi FSG model, objedinjavajući rast i remodeliranje krvnih žila, stvaranje tromba i utjecaje hemodinamike - područja koja su u velikoj mjeri bila zanemarena u većini postojećih istraživanja. Figueroa i suradnici [28] predlažu FSG računalni okvir relevantan za simulaciju bolesti poput aneurizmi, gdje je interakcija između protoka krvi i zida krvne žile, zajedno s rastom i remodeliranjem zida, ključna za razumijevanje napredovanja bolesti. Watton i suradnici [29] predstavljaju računalni okvir koji istražuje odnos između razvoja cerebralne aneurizme i hemodinamičkih podražaja na endotelnim ćelijama, koristeći model evolucije aneurizme i 3D hemodinamička rješenja. Dva primjera pokazuju kako odstupanja od standardnih vrijednosti smičnog naprezanja mogu dovesti do degradacije elastina, nudeći osnovu za proučavanje patologije aneurizmi. Wu i Sadden [30] razvili su FSG okvir s pacijentu prilagođenom geometrijom, pružajući uvid u parametre rasta pod utjecajem stresa i mehaniku fluida krvi na rast vaskularnog tkiva. Grytsan i suradnici [31] su predložili računalni FSG okvir, gdje je arterijski zid modeliran kao ojačani materijal s dva sloja, a progresija bolesti simulirana je putem G&R modela potaknutog

odstupanjima mehaničkih podražaja od homeostatskih razina. Okvir se primjenjuje za modeliranje evolucije aneurizme i otkriva utjecaj transmuralnog G&R na razvoj aneurizme, uključujući evoluciju transmuralno heterogenih naprezanja na elastin i kolagen. FSG Modeli korišteni su za modeliranje razvoja intrakranijskih aneurizmi, počevši od idealizirane zdrave arterija [32] i kliničkih slučajeva [33]. Osim toga, preliminarni nalazi modela FSG pokazali su da je specifično modeliranje za pojedinog pacijenta koje povezuje hemodinamiku s mehanobiologijom obećavajući pristup za istraživanje napretka aneurizme uzlazne torakalne aorte [34]. Nedavno je predložen model i FSG model za *in vivo* razvoj tkivno inženjerskog vaskularnog transplantata [35].

CILJEVI ISTRAŽIVANJA

Cilj istraživanja je razvoj realističnog numeričkog modela adaptacije aorte kod pojave vaskularnih lezija (aneurizma, disekcija, ateroskleroza). Razvit će se FSG model u paketu za kontrolne volumene koji može opisati utjecaj međudjelovanja deformabilne stijenke i strujanja krvi, pri srčanom ciklusu, na dugoročnu promjenu strukture stijenke aorte (G&R), mjereno u danima i godinama.

Hipoteze:
1. Moguće je razviti metodu koja osigurava nestlačivo ponašanje čvrstih tijela pri velikim deformacijama u kontrolnim volumenima
korištenjem spregnutog postupka rješavanja.
2. Moguće je opisati rast i promjenu strukture stijenke aorte korištenjem metode kontrolnih volumena.

REZULTATI

Parametri korišteni u FSG okviru morali su biti pažljivo odabrani kako bi pružili najbolji mogući rezultat simulacija. "Standardni" set parametara za G&R model odabran je ranije te se može vidjeti u TabliciTable **2**, također korištenoj u objavljenoj radu "The risk of rupture and abdominal aortic aneurysm morphology: A computational study" [13]. Međutim, nekoliko

parametara dodatno je moralo biti odabrano kako bi se do kraja definirao FSG model, a to su karakteristike strujanja CFD-a (viskoznost krvi i turbulentni model) te kriteriji taloženja tromba. Nužno je napomenuti da su postavke modela bile promatrane i na pojedinačnim geometrijama i u sklopu FSG modela. Potencijalno akumulirana razlika tijekom vremena je dovoljno značajna da ima bitan utjecaj na rezultate, te je stoga bilo bitno osloniti se na rezultate dobivene pomoću FSG simulacija. Određivanje modela viskoznosti krvi samo po sebi je izazovno zbog ovisnosti o smičnoj brzini, koja se mijenja s brzinom.

Modeli viskoznosti koji su korišteni u simulacijama bili su: Newtnovski model viskoznosti s tri vrijednosti u rasponu: $\nu = 4\times10^{-6}\,\mathrm{m^2/s}$, do $\nu = 6\times10^{-6}\,\mathrm{m^2/s}$, Cassonov model te Bird-Carreauov model. Očito je da s većom viskoznosti dolazi do povećanih vrijednosti smičnih naprezanja na stijenci aneurizme. Posljedično tome, budući da je kao kriterij taloženja tromba korišten TAWSS, veća viskoznost zahtijeva mnogo veću dilataciju AAA lumena da bi se postigla kritična vrijednost taloženja i slijedeći korak u rastu tromba. Rezultati potvrđuju ovu tvrdnju, te se jasno vidi kako se debljina tromba smanjuje s rastom koeficijenta viskoznosti za Newtnovske modele, dok se Cassonov i Bird-Carreuaov modeli nalaze između vrijednosti Newtnovskih modela, što dodatno daje potvrdu o inicijalno dobro odabranim vrijednostima. Međutim, mogu se primijetiti značajne razlike u volumenu i obliku tromba između navedenih modela.

Ispitivanje različitih modela turbulencije na pojedinačnim geometrijama nije pokazalo značajnu razliku. Međutim, kod FSG modela ta je razlika očita u kasnijim stadijima aneurizme s većim maksimalnim promjerom, gdje se objektivno češće pojavljuju turbulencije. Nakon početnog taloženja tromba, različiti modeli rezultiraju različitim procesima formiranja tromba što se primarno očituje drugačijim mjestom nastanka tromba po visini te njegovim oblikom. Turbulentni modeli potiču rast tromba u gornjem dijelu, dok laminarni modeli potiču rast u donjem dijelu lumena. To se odražava na vrijednosti maksimalnih naprezanja po visini aneurizme te njenog drugačijeg rasporeda po debljini stijenke. U usporedbi s literaturom, Zambrano [24] je pokazao da se tromb počinje taložiti na donjem dijelu aneurizme, a zatim se širi prema gornjem dijelu, što je bliže rezultatima dobivenim iz turbulentnog modela. Važno je napomenuti da su početne faze rasta slične, što pruža čvrstu osnovu za vjerovanje u legitimnost modela.

Nakon završetka implementiranja FSG modela, zadnji korak bio je ispitivanje kriterija taloženja tromba i njihovih kritičnih vrijednosti. Budući da ne postoje definirane vrijednosti u literaturi, usporedba vrijednosti OSI-a i ECAP-a s odgovarajućim kritičnim vrijednostima TAWSS-a vodila se primarno uspoređujući volumen tromba. Kako bi se vrijednosti podudarale sa standardnim kritičnim vrijednostima TAWSS-a od 0,4 Pa, odabrane su referentne vrijednosti OSI=0,4575 i ECAP=1,54. Parametar TAWSS, unatoč svojoj jednostavnosti, pokazao se kao robustan i široko primjenjiv, pružajući čvrst oslonac za daljnju analizu. Opće prihvaćena vrijednost od 0,4 Pa pokazala je očekivano zadovoljavajuće rezultate, učinkovito usmjeravajući taloženje tromba na očekivana područja. Konkretno, kada je TAWSS korišten kao kriterij taloženja, tromb je imao tendenciju početka rasta na donjem dijelu aneurizme. Nasuprot tome, drugi kriterij taloženja, OSI, pokazao je suprotni trend, taložeći tromb previsoko od središta AAA i zdravog lumena, što se smatra nepoželjnom pojavom. Budući da naprezanja izravno ovise o debljini tromba, njihove koncentracije su također na suprotnim stranama, ovisno o taloženom trombu. Samim time, kritična područja aneurizme su suprotna te se potencijalna ruptura može očekivati na drugim stranama što svakako dovodi u pitanje legitimnost modela. ECAP je parametar koji objedinjuje TAWSS i OSI po svojoj definiciji, i to u recipročnom omjeru. Gledajući vrijeme nastanka tromba, njegov volumen, lokaciju te kritična naprezanja u nekoliko trenutaka, može primijetiti da je po rezultatima znatno sličniji rezultatima dobivenim korištenjem TAWSS-a nego OSI-ja. Ta tendencija može se primijetiti i za gotovo sve ostale promatrane parametre, a ne samo za visinu maksimalnog promjera te visinu maksimalnog naprezanja na aneurizmi. Međutim, tome može biti više razloga te se ti parametri svakako mogu smatrati marginaliziranim vrijednostima.

ZAKLJUČAK

Računalna biomehanika postaje sve važniji alat za istraživanje kompleksnih fenomena u području vaskularnog zdravlja. Upotreba računalnih analiza mogla bi liječnicima i kliničarima pružiti ogromnu prednost u boljem razumijevanju procesa nastanka i razvoja bolesti. Kako bi se točno opisalo ponašanje krvnih žila, sveobuhvatan model trebao bi uključivati širok raspon parametara, te bi svaki trebao biti pažljivo analiziran i implementiran. Proces nastanka aneurizme primarno je uzrokovan degradacijom elastina. Većina aneurizmi sadrži intraluminalni tromb, čiji je proces taloženja izravno povezan sa slikom strujanjem krvi unutar lumena aneurizme. Odabir odgovarajućeg reološkog i viskoznog modela te kriterija taloženja

tromba igraju ključnu ulogu u formiranju i taloženju intraluminalnog tromba, što zauzvrat utječe na čvrstoću krvne žile.

Ovo istraživanje imalo je cilj razviti sveobuhvatan nestlačivi 3D FSG numerički model koji bi uključivao G&R model stijenke i ILT-a, CFD analizu protoka krvi te pronalaženje najboljih kriterija za formiranje i taloženje intraluminalnog tromba temeljen na CFD analizi. FSG model trebao bi imati sposobnost opisivanja kompletnog procesa ponašanja krvnih žila, uključujući promjene na stijenci aneurizme i rast aneurizme te formiranje tromba. Takav sveobuhvatan model ne postoji u literaturi do sada te se može se smatrati velikim napretkom u pokušaju boljeg razumijevanja promjena krvnih žila. U cilju postizanja što vjernijih rezultata i njihove usporedbe, analizirani su dodatni parametri kako bi postiglo maksimalno poklapanje s literaturom. G&R parametri su već analizirani i potvrđeni ranije, te je glavni fokus bio na dodatnim FSG parametrima: reološkom i turbulentnom modelu te kriteriju taloženja tromba.

Analiza smičnih brzina na dvama različitim geometrijama upućuje da je najprikladniji model viskoznosti Casson, budući da vrijednosti ulaze u Cassonov raspon prema [36]. Vrijednosti smičnih brzina Cassonovog te Bird-Carreau viskoznih modeli nalaze se u rasponu Newtonovih modela s najprikladnijim koeficijentima viskoznost za pripadajuće slučajeve. Dodatnu potvrdu za odabir Cassonovog modela daje i činjenica da većina analiziranih parametara dijeli tendencije za Newtnovski i Cassonov model. S obzirom na to da se povećanjem lumena očekuje promjena koeficijenata viskoznosti, Newtnovski model nije adekvatan za detaljnu analizu, što posebice utječe na taloženje tromba tijekom kasnijih stadija bolesti. Značajan utjecaj modela viskoznosti na tijek rasta aneurizme zahtijeva posebna istraživanja kako bi se dobile preciznije vrijednosti.

U svojim istraživanjima, Zambrano [24] je pokazao kako se tromb počinje taložiti na donjem dijelu aneurizme te se naknadno širi prema gornjem dijelu, što je sličnije rezultatima dobivenim koristeći turbulentni model. S rastom lumena, povećava se mogućnost nastanka turbulencija, čineći problem nestacionarnim prilikom određivanja modela. Konačno određivanje modela turbulencije strujanja zahtijeva dodatne podatke, uključujući eksperimentalna istraživanja, budući da numerički modeli mogu pokazivati značajne razlike, posebice u kasnijim stadijima bolesti. Ipak, razlike među modelima su vrlo male u početnim stadijima formiranja tromba, što pruža čvrstu osnovu za vjerovanje u relevantnost modela.

Detaljna analiza različitih kriterija taloženja tromba može se smatrati najvećim doprinosom ovog rada, posebice što slična ne postoji do sada. U dosadašnjim postojećim radovima i numeričkim modelima, jedini korišteni parametar bio je TAWSS. TAWSS je dao očekivano dobre rezultate te je korišten kao polazišna točka za daljnja razmatranja i određivanje kritičnih vrijednosti ostalih parametara. Analizirani su različiti indikatori te su rezultati i geometrija aneurizme i tromba uspoređivani s literaturom. Dva dodatna korištena parametra su OSI i ECAP. OSI predstavlja oscilatorno ponašanje koje je vrlo važno u formiranju ILT-a prema Bhagavanu [26], dok ECAP objedinjuje TAWSS i OSI po svojoj definiciji. OSI se nije pokazao kao zasebno dobar parametar nastanka tromba zbog nepodudaranja rezultata s literaturom. ECAP je pokazao izuzetno obećavajuće rezultate, ističući se kao robustan parametar za modeliranje taloženja tromba iz razloga što pokazuje bolje podudaranje s drugim rezultatima i spoznajama iz literature. Važno je napomenuti da je ECAP dao rezultate približne onima dobivenima korištenjem TAWSS-a, posebno u kasnijim fazama rasta aneurizme. To potvrđuje da ECAP, svojim objedinjavanjem utjecaja i TAWSS-a i OSI-a, pruža širi, robusniji pogled na proces taloženja tromba. ECAP se može smatrati kao najkompletniji kriterij od svih navedenih, učinkovito objedinjavajući oba zasebna kriterija.

Određeni nedostaci istraživanja moraju biti spomenuti, a najveća potencijalna opasnost leži u nedostatku robusnosti modela. Činjenica je da čak i manje izmjene vrijednosti parametara mogu rezultirati značajnim razlikama u rezultatima zbog akumuliranja pogreške. Slično tome, promjena modela viskoznost, modela turbulencije ili geometrijskih parametara aneurizme čini značajnu razliku u ishodima rezultata. Također, bitno je reći da se ni jedan parametar taloženja tromba, uključujući ECAP, ne može smatrati optimalnim kriterijem te konačnim ciljem, što ukazuje na potrebu istraživanja dodatnih opcija. Važno je napomenuti da idealizirana geometrija aorte korištena u FSG okviru ne odražava precizno moguće kompleksnosti anatomije stvarnog svijeta, što potencijalno dovodi do varijacija u rezultatima modela. Ipak, postizanje idealnih postavki parametara modela za ove slučajeve ostaje neizvediv pothvat za koji bi u budućnosti trebalo biti ponuđeno rješenje.

Kao dodatak ovom radu, korištenjem G&R modela provedeno je istraživanje o geometrijskim značajkama aneurizmi koje su podložnije rupturi, uzevši u obzir trenutno najkorištenije kriterije: maksimalni promjer i iskustvo kliničara. Razmatrajući sveobuhvatan popis od 25 geometrijskih značajki, cilj je bio predložiti složeniji i pouzdaniji indikator koji će upućivati na opasnosti od rupture aneurizme, uvidjevši da pojedinačni sami po sebi nisu dovoljni. Kroz

obimne simulacije i analize podataka, otkrivena su ograničenja tradicionalnih geometrijskih kriterija te su predloženi novi: Geometrijski indeks potencijala puknuća (GRPI) i normalizirana duljina aneurizme (NAL). Nakon provedene analize, postalo je jasno da su oba indeksa postala pouzdaniji indikatori rupture, što je i dodatno potvrđeno statističkom analizom.

Zaključno, ovo istraživanje ne samo da duboko ulazi u složenost područja biomehanike i vaskularnog zdravlja, već također usmjerava prema budućnosti u kojoj inovativni modeli i kriteriji omogućuju značajno unaprjeđenje dijagnostike i liječenja. Kroz pomnu analizu i numeričke simulacije, ovo istraživanje otvara vrata dosad neistraženim mogućnostima i rješenjima, pružajući vrijedan doprinos području biomehanike koje je u ubrzanom razvoju.

ZNANSTVENI DOPRINOS

1. 3D FSG numerički okvir prilagođen za simulaciju lezija, posebno aneurizmi, uključujući dinamiku ILT-a, i nestlačivo ponašanja.
2. Analiza parametara taloženja ILT-a i njihove predložene kritične vrijednosti.
3. Uvođenje dva indikatora koji predviđaju rupturu aneurizme, uz statističku analizu njihove pouzdanosti i točnost

1. INTRODUCTION

1.1. Motivation

Aorta is the largest artery in the human body. It originates from the left ventricle, and it serves as a conduit for the transportation of blood to other vascular structures, which subsequently facilitates the distribution of oxygen and nutrients to individual cells in the organism. In general, healthy arterial walls are composed of three layers: *tunica intima*, *tunica media* and *tunica adventitia*, each of which contains different constituents and their ratios.

Tunica intima is an inner layer consisting of a monolayer of endothelial cells (i.e., endothelium). *Tunica media* is separated from intima and adventitial by internal and external elastic laminae, respectively This middle layer, contains smooth muscle cells, elastin, collagen. Finally, the outer layer *tunica adventitia* consists mostly of collagen and elastin. It also contains various cells like fibroblasts, that ensure constant production (or turnover) of collagen. Endothelium is sensitive to the changes in blood flow, or rather to the wall shear stress (WSS) induced by the blood flow on the wall. A change in WSS can enhance the production of vasoactive molecules which affect smooth muscle contraction to maintain the homeostatic value of WSS in short-term or turnover of SMC in long-term. Aortic wall with its constituents and layers is shown in Figure 1.1.

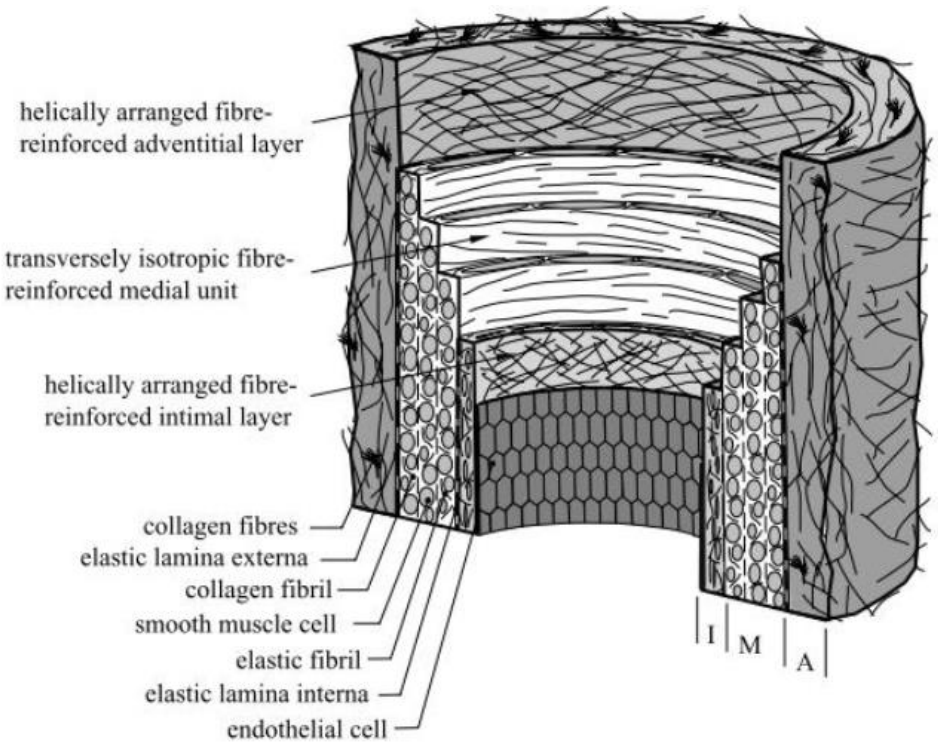

Figure 1.1 Layered structure taken from [37]

The aorta can be affected by various diseases or lesions, and one notable condition is abdominal aortic aneurysms (AAA). It is a focal dilatation of the blood vessel for more than 50% in diameter. Medical workers consider aorta to be an aneurysm if it exceeds 30 mm in diameter. Most of the AAAs are known to contain intraluminal thrombus (ILT) [1], a thrombotic material that typically accumulates within the dilation of the aorta, particularly in the infrarenal segment. ILT formation initiates when the endothelium is damaged by 80% or more [2], [3]. The endothelium, responsive to alterations in blood flow, is typically damaged due to elevated wall shear stress (WSS). The ILT deposition can be conceptualized as a four-phase process, as stated in [4]. In the first phase (very fresh), the whole ILT consists mostly of erythrocytes from the blood stream mixed with some loose fibrin network, leucocytes, or thrombocytes in low percentages. In the second phase (young), while ILT is still young, fibrin networks start to grow as a large percentage of loose fibrin network as well as erythrocytes. In the third (intermediate) and fourth (subsequent) phase of ILT deposition, erythrocytes and proteins disintegrate, leaving condensed fibrin networks and dense protein residues, respectively. These stages hold limited pertinence to the current analysis, which is primarily concerned with the genesis and initial development of aneurysms, typically not progressing to these advanced phases. All four stages are shown in Figure 1.2.

Figure 1.2 Layered structure of intraluminal thrombus, from [38]

The driving ambition behind this research is the formulation of an all-encompassing fluid solid growth (FSG) model. This advanced model is envisioned to be a transformative tool for medical practitioners, particularly in the realm of cardiology, providing them with refined insights and strategies to treat conditions such as AAA. The innovative aspect of the FSG model lies in its ability to integrate the dynamic progression of aneurysms' ILT, considering its incompressible behavior and iterative blood flow parameters. This iterative approach reflects the real-time growth patterns of aneurysms, offering a predictive capability that has the potential to inform timely interventions and thus contribute significantly to the reduction of mortality associated with cardiac diseases. This research aims to fill a significant gap by developing a novel FSG model for cardiac diseases, particularly abdominal aortic aneurysms, offering a new approach currently lacking in the field.

Aortic wall will be modeled using the G&R theory, which accounts for the aorta's composite structure, active smooth muscle stress, and the nonlinear and anisotropic behavior of its constituents, adding complexity to the numerical modeling process. The complexity of the modeling extends to the ILT, which is also simulated using the G&R theory. This approach unravels the intricate relationship between ILT formation, its deposition, and the significant impact of blood flow dynamics on which these processes crucially depend. Blood flow not only significantly affects AAA growth but also has a profound impact on ILT formation, with the size and shape of ILT being direct consequences of the blood stream's interaction with the AAA [39]. In addition, several novel blood parameters will be employed and investigated to optimize and accurately simulate the ILT formation process withing FSG model. Additionally, the aortic wall has an almost ideal incompressible behavior, and it necessitates the integration of into the

G&R model to achieve a realistic and accurate FSG model. Various finite volume method-based techniques, which ensure incompressibility for small deformations [40] are pivotal in this context and will be utilized in the G&R model to better understand and represent the disease's progression.

1.2. Literature review

The development of AAA involves three primary factors: aortic wall growth and remodeling, blood flow, and ILT formation and deposition. Blood flow plays a crucial role in the ILT deposition and consequently influences the progression and direction of AAA disease. Over time, various mathematical models have been created to represent one or more of these aspects and their interplay. These models have grown more sophisticated with the availability of new experimental and histological data, offering deeper insights into AAA's complex mechanobiological processes. This section will provide a summary of existing numerical models and discuss previous studies focused on analyzing and describing AAAs.

G&R

The inception of G&R models in arterial tissue mechanics represents a pivotal moment in biomedical engineering and biomechanics. Skalak et al. [41] proposed G&R model where the biological and mechanical aspects of arterial tissues is concerned, conceptualized as a time-dependent displacement field. This approach treats growth as a spatial distribution of mass sources and defines a growth rate tensor, akin to a strain rate tensor. Skalak's model provides a foundational framework for understanding the biological and mechanical aspects of soft tissue growth and remodeling, relevant to fields like arterial tissue mechanics. The first G&R model was introduced by Rodriguez et al. [6], representing a pivotal advancement in the biomechanical understanding of tissue changes in terms of both mass (growth) and structure (remodeling). Their model proposed a general continuum formulation for finite volumetric growth in elastic tissues, highlighting the critical influence of mechanical stress on these processes. This model was notable for aligning the growth-rate tensor with the stress tensor in stressed tissues, demonstrating a qualitative alignment with experimental data, which was crucial for the better understanding of kinematics of growth in soft tissues and contributed significantly to the development of the theory of finite volumetric growth. In 2002, Humphrey and Rajagopal et al. [7] made a significant contribution to the field of biomechanics with the

introduction of a constrained mixture model for the G&R of soft tissues. This innovative approach combined elements of classical mixture and homogenization theories to provide a comprehensive analysis of the biomechanical properties of soft tissues, particularly focusing on their adaptive mechanisms in response to mechanical stimuli. The model was particularly noteworthy for its detailed representation of the arterial wall, conceptualizing it as a composite of collagen fibers and ground substance. It incorporated a constraint equation to regulate the overall volume fraction and included sophisticated equations to simulate the G&R processes influenced by mechanical and biological factors. This model has since been instrumental in enhancing the understanding of how variables like blood pressure, wall shear stress, and inflammation can impact the growth and remodeling of arterial walls, offering vital insights into vascular diseases and therapies. Holzapfel's contribution to arterial wall modeling is represented in his development of a hyperelastic constitutive model [8], integral to the Holzapfel-Gasser-Ogden (HGO) framework. This model, focusing on the growth-induced alterations in the arterial wall's elastic properties, employs a fiber-reinforced approach. It conceptualizes the arterial wall as being made up of a matrix material intertwined with a network of collagen fibers. Central to the HGO model, this design allows for the fibers' orientation and distribution to evolve in response to the processes of growth and remodeling, offering a comprehensive understanding of arterial mechanics. The HGO model has been used in numerous studies to investigate the effects of various factors, such as aging, hypertension, and aneurysm, on the mechanical properties and growth of arterial walls. Valentin et al. [9] pioneered the implementation of the constrained mixture G&R model in a 3D finite element code, highlighting its potential for modeling various tissues and diseases, including tendon healing, myocardial hypertrophy, and arterial adaptations. Cyron et al. [15] presented a novel temporally homogenized model that combines kinematic and constrained mixture approaches for growth and remodeling of load-bearing soft tissues. The model demonstrates effective description of cell-mediated tissue adaptation and aneurysm progression, highlighting the connection between growth, remodeling, and viscoelasticity, enabling seamless integration within existing simulation frameworks.

Karšaj et al. [10] made significant progress by developing a 3D growth and remodeling (G&R) model capable of capturing alterations in artery geometry and structure in response to changes in hemodynamics, including blood flow and pressure. This model was extended to include three-layered arteries and was subsequently implemented into a 3D finite element code by Horvat et al. [11] , enabling comprehensive analyses of radial, axial, and circumferential

changes within an axisymmetric and asymmetric computational model of AAA. The model was used to examine the influence of collagen dispersion on AAA outcome [12], and geometrical model parameters on the stress morphology in the stack and the probability of rupture [13]. It has also been expanded to describe thrombus deposition [14]. Yet, in that work, two scenarios were considered: fully and partially thrombosed aneurysm with thrombus growth up to the predefined luminal diameter. In this work we expand the work further to include hemodynamically driven deposition of intraluminal thrombus.

ILT

While the precise mechanisms behind the ILT formation remain elusive, it is commonly thought to be linked with the dynamics of blood flow within aneurysms. Notably, ILTs are observed in over 75% of AAAs. The role of ILT in the progression of aneurysms is multifaceted, encompassing complex biological, chemical, and mechanical aspects [42]. This complexity plays a substantial role in influencing the outcomes of AAAs [1]. In the early 1990s, Inzoli et al. [16], [43] proposed a novel concept suggesting that ILT could serve as a protective barrier against aortic wall stress, thereby reducing the risk of rupture, which has been confirmed by Behr-Rasmussen studies [20]. Subsequent investigations, [17], [18], [19] have provided further and similar evidence supporting the influence of ILT on AAA mechanics. In contrast, the research by Burke and FitzGerald [21] highlights the biochemical ILT impact, specifically emphasizing oxidative stress's role in vascular health deterioration. The study illuminates the involvement of enzyme activities in vascular damage, suggesting their potential contribution to the development and progression of AAA, thus indicating a significant biochemical influence alongside mechanical factors in ILT and AAA. Following extensive uniaxial extension tests, Wang et al. [22] determined that ILT exhibits isotropic characteristics with a nonhomogeneous structure, displaying enhanced strength and stiffness within the luminal region, using a two-parameter, isotropic material model. Vande Geest et al. [44] used non-linear hyperelastic isotropic constitutive model with the strain energy, generally used for rubber-like materials. Further improvement was done by Tong et al. [4] who found clear indications of mechanical anisotropy in several luminal layers, suggesting that the luminal layer of the ILT is generally not isotropic. Di Achille et al. [25] suggested that the ILT likely plays a significant role in influencing the complex biomechanical and pathological characteristics of certain vascular abnormalities. Virag et al. [23] developed a 3D numerical model of AAA, which unlike previous computational models that focused solely on wall mechanics or hemodynamics without considering ILT, integrates the biomechanics, mechanobiology, and biochemistry of

thrombus-laden AAAs. By incorporating the diverse effects of ILT, including its biochemical properties and biomechanical behavior, the model reveals that the presence of ILT can either arrest or contribute to the rupture of AAAs, depending on factors such as the release of proteases and stiffness of fibrin. Horvat et al. [14] extended a previously proposed model for AAAs by incorporating the role of ILT in AAA growth using a 3D finite element constrained mixture G&R model.

CFD

The onset and progression of many cardiovascular diseases (CVDs) are often associated with blood flow dynamics, which also plays a key role in the ILT development [45], [46]. Wall shear stress (WSS), a critical factor in vascular hemodynamics, is hypothesized to influence endothelial cell function and trigger platelet activation. These processes are essential in the formation of blood clots. The study by Di Achille et al. [25] elaborates on this concept, explaining the significant role of WSS in these initial stages of thrombus development. For example, atherosclerosis, the most developed vascular disease overall, but also the most common cause of other CVDs [47], is believed to be caused by low wall shear stresses. Low WSS allow increased platelet deposition and production of platelet derived growth factors that are myogenic for smooth muscle and fibroblasts; it also increases endothelial cell turnover and its permeability. Thus, the low wall shear stress appears to change the character of endothelial cells from atheroprotective to atherogenic [48]. Understanding the relationship between blood flow and ILT deposition is crucial for exploring the pathogenesis of various cardiovascular diseases, AAA in the first place, and developing effective prevention and treatment strategies. The hemodynamics of blood flow, including flow velocity, shear stress, and turbulence settings, significantly influence ILT formation and growth. Low wall shear stress in injured endothelium promotes ILT formation as it allows platelets to accumulate. Zambrano et al. [24] was among the first who concluded that low time averaged wall shear stress (TAWSS) promotes ILT formation and the one who set a value for critical threshold. He analyzed and showed computational results for 10 carotid arteries, 2 per every patient, where regions of low WSS are crucial for ILT deposition. In addition, Zambrano sets the threshold value for TAWSS ILT deposition criteria. Shadden et al. [49] investigated relationship between fluid flow and mechanical platelet activation, necessary for thrombus deposition, in stenosed artery. They proposed index named platelet activation potential (PLAP), a non-dimensional scalar that represents the magnitude of shear rates that a fluid particle accumulates while travelling throughout the fluid domain.

DiAchille et al. [25] introduces oscillatory shear index (OSI) and endothelial cell activation potential (ECAP), as two additional ILT deposition parameters. Later, he suggested thrombus formation potential (TPF), a combination of TAWSS, OSI, and PLAP, as a very promising criterium for describing the ILT formation. TPF identifies local regions of the wall that were simultaneously exposed to pro-thrombotic WSS stimuli and a flow rich in activated platelets. However, there is no mentioned any threshold value for practical use and numerical model, which remains gap in the research. Several studies focused on determination of local hemodynamic parameters that influence ILT formation and growth, by computing their variations between two follow-ups. Arzani et al. [50] quantified TAWSS, OSI, and mean exposure time at baseline. He concluded that regions of low OSI had the strongest correlation with ILT growth, however prominent regions of high OSI and low TAWSS did not appear to coincide with locations of thrombus deposition. Yet, Zambrano et al. [24] observed a relationship between low TAWSS and the ILT accumulation. Tzirakis et al. [51] observed a relationship between ILT growth and time-averaged wall shear stress (TAWSS) and oscillatory shear index (OSI) but not with relative residence time (RRT) or any combination of the three parameters. In the latest research, DiAchille et al. [52] presented a new phenomenological metric, thrombus formation potential (TFP), which can be used for advanced predict of ILT formation in a specific aneurysmal area.

FSG

In their seminal paper, Humphrey and Taylor [27] explored the nuances between intracranial and abdominal aortic aneurysms, emphasizing the need for advanced computational models to accurately represent their complex dynamics. They stressed the importance of the biomechanical environment, highlighting how the interplay between blood flow and the aortic wall is crucial in understanding aneurysm progression. Recognizing a gap in existing research, they articulated the need for a new class of models capable of detailing the evolving geometry, nonlinear wall properties, and hemodynamics. These elements are pivotal in dictating cellular mechanobiology and matrix turnover. To address these complexities, they proposed the FSG model, which aims to be the most comprehensive modelling approach, incorporating G&R of blood vessels, the formation of ILT, and hemodynamic impacts—areas notably lacking in much of the current research. This vision by Humphrey and Taylor set the groundwork for future explorations in aneurysm research and treatment strategies, marking a significant contribution to the field. The pioneering work in the field of reactive mixtures comprising charged solid and

fluid constituents was introduced by Ateshian et al. [17]. This seminal, but overall study, marked a significant advancement in the comprehensive understanding and modeling of such systems, laying the foundation for subsequent research in this area. Figueroa et al. [28] propose a computational framework that integrates fluid dynamics, solid mechanics, and biological growth to model cardiovascular phenomena. This framework is especially relevant for simulating diseases like aneurysms, where the interaction between blood flow and the vessel wall, along with the growth or remodeling of the wall, is crucial for understanding disease progression. Watton et al. [29] presented a computational framework that explores the relationship between cerebral aneurysm development and hemodynamic stimuli on endothelial cells, using an aneurysm evolution model and 3D hemodynamic solutions. Two examples show how deviations from normotensive values of WSS can lead to elastin degradation, offering a basis for studying aneurysmal disease etiology.

FSG models have been used to study evolving AAAs on patient-specific aneurysms with updated hemodynamic load; some studies treated aortic wall as membrane [30], [53], others modelled artery as a thick wall [31]. The main disadvantage of these models is that they do not consider G&R process but only study the aneurysm at a certain time and shape; what is called snapshot analysis. Sheidaei et al. [53] in their study explored the interrelation between WSS changes and arterial wall evolution, revealing the role of low WSS in elastin degradation, elevated wall stress, and accelerated AAA enlargement while membrane G&R model was used to describe the aortic wall. Wu and Sadden [30] made a patient-specific geometry FSG model framework, offering insights into the influence of stress-mediated growth parameters and blood flow mechanics on vascular tissue growth. Grytsan et al. [31] proposed a thick-walled FSG computational framework, where the arterial wall is modeled as a fiber-reinforced material with two layers, and disease progression is simulated through G&R driven by deviations of mechanical stimuli from homeostatic levels. The framework is applied to model AAA evolution and reveals the influence of transmural G&R on aneurysm development, including the evolution of transmurally heterogeneous elastin and collagen strains. FSG models have been used for modelling intracranial aneurysm progression, starting idealized healthy artery [32] and clinical cases [33]. Additionally, preliminary FSG model findings showed that patient-specific computational modelling coupling hemodynamics with mechanobiology is a promising approach to explore ascending thoracic aortic aneurysm progression [34]. Recently, a FSG model of *in vivo* development of a tissue engineered vascular graft was proposed in [35].

Until now, the establishment of a comprehensive FSG model that integrates G&R of the blood vessel wall, ILT modeling, and analysis of blood flow using non-Newtonian fluids remains an unresolved challenge in the field of biomechanics. Moreover, the existing AAA rupture risk assessment models predominantly rely on the parameter of TAWSS, while other proposed parameters such as OSI and ECAP have not been extensively incorporated into these models. Therefore, there is a significant opportunity for improvement in this area, particularly by incorporating additional parameters for ILT deposition criteria.

1.3. Objectives and Thesis hypothesis

The proposed research endeavors to create a comprehensive FSG numerical model for aneurysms laden with thrombus. This model will integrate the G&R model of the arterial wall and ILT with the CFD analysis of blood flow. Additionally, criteria for ILT deposition will be carefully selected and implemented. The behavior of the blood vessel and ILT, characterized by incompressibility, will be accurately incorporated into the model.

The hypotheses stated for this research are:

1. It is possible to develop a method that ensures the incompressible behavior of large strain solid materials in finite volume environment by using block-coupled solution procedure.

2. It is possible to describe growth and remodeling of aortic wall by using the finite volume method.

1.4. Thesis Outline

Chapter 1

The initial chapter serves as an introduction to the thesis, offering a comprehensive overview of its underlying motivation and clearly defining its objectives. Within this section, the literature

review not only reinforces the thesis's motivation but also provides additional context to elucidate its overarching goals.

Chapter 2

Chapter "Methodology" delineates the three pivotal components (G&R of the wall and ILT, CFD of blood stream, incompressibility of blood vessel) of the thesis and the methodology behind it. After that, it provides a detailed exposition of the FSG model, offering comprehensive insights into its structure and functionalities, giving more attention to ILT deposition process and iterative system for AAA growth.

Chapter 3

Chapter "Influence of geometry on AAA rupture" explores the geometric features of AAA and their influence on aneurysmal rupture. Leveraging applied G&R theory, the analysis aims to make a scientific contribution in an area that is relatively unexplored. The chapter delves into patient-specific numerical stress analysis based on G&R models, addressing assumptions about wall structure, and introducing new parameters to enhance predictive capabilities.

Chapter 4

Chapter "CFD simulations of aortic blood flow" focuses on the best CFD simulation settings: Selecting the viscosity model and turbulence regime on a fixed geometry. Shear rate analysis on two geometries revealed variations in shear rate due to pulsatile flow, leading to the selection of viscosity model. Their differences highlighted the challenge of determining viscosity coefficients accurately. The choice of a laminar flow regime was made due to the complexity of the model and computational cost. Despite seemingly subtle differences, the chapter emphasizes the importance of minimizing errors in the FSG model, particularly in ILT deposition criteria.

Chapter 5

Chapter "FSG model settings" is the axis of this research, and it unites all the presented parts and theories into a comprehensive FSG model. This chapter investigates how every numerical setting influences the model and discusses the impact on its sensitivity and stability. It shows differences in results and highlights the right choices for blood viscosity, ILT deposition criteria and turbulence model. In addition, here is presented and discussed OSI and ECAP thresholds values that were introduced as addition to the field.

Chapter 6

The concluding chapter marks progress in numerical modeling of AAA, highlighting both the strengths and limitations of the FSG model. It provides insights into the obtained rupture indices and discusses potential avenues for enhancing the model in future research.

2. METHODOLOGY

2.1. Growth and remodeling model

2.1.1. Growth and remodeling model of the wall

Growth and remodeling theory provides a framework for understanding the fundamental mechanisms by which changes in the mechanical environment influence biological tissues. It aims to improve understanding of biochemical and biomechanical processes, as well as predict disease progression. It is assumed that there are three different constituents out of which the blood vessel wall is made of: elastin, fibrillar collagens fibers orientated along four specific directions (axial, circumferential, and two symmetrically oblique directions), and smooth muscle cells SMC. The model simplifies the actual wall structure to three layers and only mechanical essential constituents are modeled in each. G&R theory combines two interconnected branches of study: growth process and remodeling process. The concept of growth involves changes in the mass or volume of biological materials over time. This can include cell proliferation, extracellular matrix deposition, and other mechanisms that contribute to an increase in overall tissue size. On the other hand, remodeling focuses on structural changes within the material, such as alterations in the organization, composition, or properties of the tissue. At the same time, G&R theory is anchored in two fundamental concepts. The first concept, known as constrained mixture theory, conceptualizes soft tissues as a mixture of different constituents, each with its own individual properties and behaviors. In this model, the growth and remodeling of tissues are constrained by the interactions between these constituents. The model accounts for how different components of a tissue contribute and respond to mechanical stimuli, such as stress and strain. This approach allows for a more detailed and dynamic understanding of how soft tissues evolve over time, both in normal physiological conditions and in response to various pathologies. The theory of evolving configurations offers a dynamic perspective on the behavior of biological tissues. It introduced the concept that the structural and compositional state of a tissue is not fixed but continuously changes over time. This change is driven by biological processes such as growth and remodeling in response to various stimuli. Unlike conventional models that assume a constant reference state for tissues, this theory proposes that the reference configuration of a tissue evolves, reflecting the history of its adaptations, growth, and the remodeling processes it has undergone.

The constituents of the aortic wall, namely elastin, smooth muscle cells (SMC), and collagen, play crucial roles in maintaining vascular integrity. Understanding the variations in the mass of constituents, including their production and degradation, holds significant importance due to its direct influence on stress. Therefore, accurate modeling of these dynamic processes is crucial in this context. Elastin is a flexible and resilient material that can withstand mechanical stresses from different directions due to its isotropic nature. However, its production is restricted to the prenatal period, and cannot be produced in adult age, even when it is being decomposed due to aging or some disease. It has a half-life of 40 years, contributing to its long-term presence and functionality. On the other hand, SMC and collagen exhibit different properties. SMC, which are vital for vascular contractility and remodeling, have a relatively short half-life of 70-80 days. Collagen, organized in four families along axial, circumferential, and symmetrically oblique directions, provides structural support to the aortic wall.

Homeostasis can be conceptualized as the physiological process by which the body maintains a state of dynamic equilibrium, particularly in terms of the structural and functional integrity of the aortic wall. In a healthy aorta, aortic wall experiences and withstands various mechanical stresses while maintaining its structural integrity and can be seen as vascular homeostasis. Homeostasis in this context underscores the delicate balance between various biomechanical forces acting upon the aortic wall and the intrinsic physiological mechanisms that strive to preserve the wall's integrity against these forces. In an AAA, however, the presence of the ILT alters the normal stress distribution, potentially disrupting this homeostasis. The altered mechanical environment can lead to further degradation of the aortic wall, exacerbating the aneurysm. Maintaining homeostasis in the aortic wall involves a balance between the production and degradation of collagen and SMC, thereby preserving their overall mass. This emphasizes how important it is to follow the production or removal of individual and common ratio of constituents. However, external stimuli can disrupt this homeostasis. Increased stresses in the aortic wall trigger heightened production and degradation of these constituents, while elevated wall shear stress due to increased blood flow leads to a reduction in mass production. There are many reasons for the process of growth and remodeling in the human body.

As people age, the structure of the aorta undergoes changes. These changes can include alterations in the size, shape, and mechanical properties of the aorta. The aorta may become less elastic, more rigid, and may increase in diameter and length. These alterations are often

attributed to the gradual breakdown of elastin fibers and an increase in collagen content, which affects the aortic wall's ability to stretch and recoil. In populations with a high prevalence of hypertension and atherosclerosis, the aging process of the aorta might be accelerated [54]. Hypertension increases the mechanical stress on the arterial wall, potentially speeding up the degradation of elastin and promoting the stiffening of the aorta. Atherosclerosis can lead to further structural changes, including thickening of the arterial wall and narrowing of the arterial lumen. Aging, development, diseases, or injuries are the most common events that cause changes in material composition while continual constituents' turnover is a phenomenon that happens all the time. The relatively short half-life of collagen and SMC makes their production and degradation processes critical factors influencing stress within the system. Therefore, it is of utmost importance to accurately model these dynamic processes to better understand their impact on stress levels. These aspects underscore that the aging of elastin in the aorta is a complex process influenced by its initial mass, the rate of degradation, and its mechanical properties. This complexity is crucial in understanding the biomechanical changes that occur in the aortic wall with aging and in disease states like AAAs.

It's important to note that the aging of elastin is characterized by more than just its mechanical properties; its initial mass and prestretch are also significant factors. Additionally, all original constituents were deposited in the vessel wall at a G&R initial time, $\tau = 0$ with prestretch $\mathbf{G}^k(0)$, while new materials are deposited at a certain time $\tau = \langle 0, s]$, implying prestretch $\mathbf{G}^k(s)$ for the time. Figure 2.1 shows a development over time of aortic G&R model of wall and corresponding deformation gradient $\mathbf{F}$ with pre-stretch $\mathbf{G}$ over time τ. Loss of elastin begins to occur in time $\tau = 0$, which corresponds to a 40-year-old patient, at which time elastin degradation starts due to aging and half-life duration. In this context, time $\tau = 0$ marks the start of the simulation, representing the moment when the aged aorta experiences a sudden but minimal loss of elastin. The time τ serves as a general point in time when new constituents are formed and integrated into either the ILT or the aortic wall. The time $\tau = s$ corresponds to the present time in the simulation, at which point the various quantities are analyzed. It is also important to note that each constituent has its own unique, stress-free natural configuration. In this model, it is assumed that $\mathbf{G}^k(\tau)$ remains constant throughout the entire time τ, although it may differ in cases of disease.

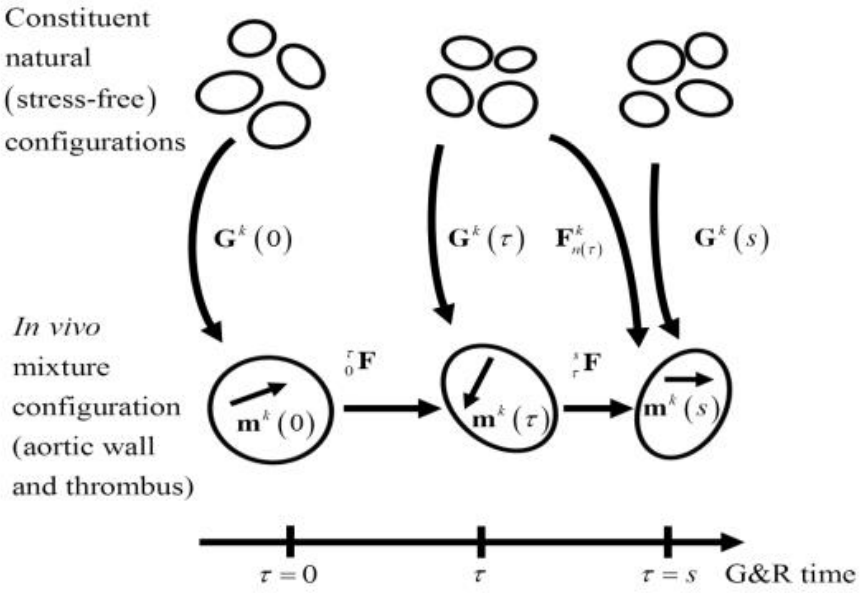

Figure 2.1 Schematic representation of G&R related configurations and deformations [10]

Each constituent in the aorta tissue, such as elastin, collagen, and smooth muscle, possesses a specific mass. This mass refers to the quantity of each constituent present within the aorta at two key points in time: the initial and the current time. This comparison helps in understanding how these constituents change in quantity over time, reflecting the dynamic process of tissue growth, remodeling, or degeneration. Rates of production and degradation play a crucial role in defining the turnover of collagen and smooth muscle cells. The G&R models are based on the fundamental concept that soft tissues undergo a continuous turnover of their constituents. Specifically, collagen and smooth muscle experience degradation, while new tissue is continuously deposited. This dynamic process of mass turnover is essential in understanding the aging and remodeling behavior of the aorta and is critical for comprehending how its mechanical properties are affected over time. Mathematically, current mass is calculated as

$$M^k(s) = M^k(0)\,Q^k(s) + \int_0^s \dot{m}^k(\tau)\,q^k(s-\tau)\,\mathrm{d}\tau, \tag{1}$$

where $M^k(s)$ and $M^k(0)$ are total (integration pointwise) masses of constituent *k* at the current time *s* and initial time 0, respectively. Unlike collagen and smooth muscle, elastin is produced only in prenatal age, meaning production rate $\dot{m}^{\mathrm{e}}(\tau) = 0$. That simplifies equation to

$$M^{\mathrm{e}}(s) = M^{\mathrm{e}}(0) Q^{\mathrm{e}}(s), \tag{2}$$

Mass production rate is denoted by $\dot{m}^k(\tau)$ and $q^k(\mathrm{s}-\tau)$ is the survival function defining the percentage of constituent mass produced in a time τ that survived till the current G&R time *s*. Survival function for mass existing in the initial G&R time $\tau = 0$, $q^k(\mathrm{s}-0)$, is labeled as $Q^k(\mathrm{s})$. Survival function can be written as

$$q^k(s-\tau) = \exp\left(-\int_{\tau}^{s} K_q^k\left(\tilde{\tau}\right) d\tilde{\tau} \right), \tag{3}$$

where K_q^k rate-type parameter describes mass removal.

Homeostasis is considered every process that tends to maintain its original function and form. Often, such complex, biological processes like G&R of the aortic wall tend to have changes in mass and structure. G&R changes in the aortic wall are caused, as assumed, mostly due to deviation from the homeostatic state $\left\|\boldsymbol{\sigma}_{\mathrm{h}}^k\right\|$ in wall stress. Homeostatic state $\left\|\boldsymbol{\sigma}_{\mathrm{h}}^k\right\|$ represents the homeostatic Cauchy stress tensor.

The mechanobiologically driven rate of mass production $\dot{m}^k(\tau)$ of each constituent *k* was thus defined as a function of the basal production rate m_B^k and changes in Cauchy stress $\boldsymbol{\sigma}^k(\tau)$ relative to the homeostatic value:

$$\dot{m}^k(\tau) = m_B^k \left(1 + K_\sigma^k \frac{\left\|\boldsymbol{\sigma}^k(\tau)\right\| - \left\|\boldsymbol{\sigma}_h^k\right\|}{\left\|\boldsymbol{\sigma}_h^k\right\|} + K_C^k \frac{\tau_w(\tau) - \tau_{w,h}}{\tau_{w,h}} \right), \tag{4}$$

K_σ^k and K_C^k are rate parameters governing constituent level stress-driven mass production and gain-type rate parameters responsible for constrictor-mediated changes, respectively; τ_w, $\tau_{w,h}$ are wall shear stress in the instant time τ and homeostatic value of wall shear stress. The Cauchy stress within the aortic wall is defined under the assumption of a constrained mixture, i.e., assuming that overall stored energy function can be calculated as $W = \sum_k W^k$, as

$$\boldsymbol{\sigma} = \frac{2}{\det(\mathbf{F})} \mathbf{F} \frac{\partial W\left(\mathbf{C}_{n(\tau)}^k\right)}{\partial \mathbf{C}} \mathbf{F}^T + \sigma^{\mathrm{active}} \mathbf{e}_\theta \otimes \mathbf{e}_\theta, \tag{5}$$

with $\mathbf{F}$ the overall deformation gradient, $\mathbf{C}=\mathbf{F}^{\mathrm{T}}\mathbf{F}$ is the right Cauchy-Green tensor, and σ^{active} is the active stress contribution from smooth muscle contractility in the circumferential direction $\mathbf{e}_\theta$. Moreover, the specific stored energy functions W^k for collagen and smooth muscle is given by

$$W^k(s)=\frac{M^k(0)}{\sum_k M^k(s)}\hat{W}^k\left(\mathbf{C}^k_{n(0)}(s)\right)Q^k(s)+\int_0^s\frac{\dot{m}^k(\tau)}{\sum_k M^k(s)}\hat{W}^k\left(\mathbf{C}^k_{n(\tau)}(s)\right)q^k(s-\tau)\,\mathrm{d}\tau, \tag{6}$$

with $\mathbf{C}^k_{n(\tau)}(s)$ the right Cauchy-Green tensor for constituent *k*, calculated by $\mathbf{C}^k_{n(\tau)}(s)=\left(\mathbf{F}^k_{n(\tau)}(s)\right)^{\mathrm{T}}\mathbf{F}^k_{n(\tau)}(s)$, where $\mathbf{F}^k_{n(\tau)}(s)$ is the deformation gradient from the natural configuration to the current configuration at the time *s* for constituent *k* produced at a time τ. It depends on the prestretch tensor $\mathbf{G}^k(\tau)$ of the constituent at the moment of its deposition τ and deformation gradient of the aortic wall (mixture) ${}^s_\tau\mathbf{F}$ from time of deposition to current time *s*, i.e.

$$\mathbf{F}^k_{n(\tau)}(s)={}^s_\tau\mathbf{F}\mathbf{G}^k(\tau), \tag{7}$$

New fiber, produced at a certain time τ, is deposited in an extracellular matrix with an initial prestretch $\mathbf{G}^k(0)$ in order to maintain the homeostatic stress $\boldsymbol{\sigma}_{\mathrm{h}}$. It is assumed that the initial prestretch of the newly produced collagen fiber does not depend on changes in the overall geometry and stress of the wall. Tensor $\mathbf{G}^k(\tau)$ is a deposition stretch tensor that describes the change in geometry from the natural unloaded configuration of the collagen created at a time τ to its loaded geometry when it is placed in the extracellular matrix at any instant $\tau\in[0,s]$:

$$\mathbf{G}^k(\tau)=G^k\mathbf{m}^k(\tau)\otimes\mathbf{m}^k(\tau), \tag{8}$$

where G^k is a scalar value of fiber prestretch, while $\mathbf{m}^k$ is a unit vector that represents the orientation of the fiber. Collagen and smooth muscle were modeled as fiber-like behavior without significant compressive stiffness, as in most prior G&R models. Isotropic elastin is modeled as a neo-Hookean material, while the stored energy function per unit mass for the fiber structures is defined (according to Humphrey and Rajagopal [55]) as an exponential function

$$\hat{W}^k=\frac{c_2^k}{4c_3^k}\left[\exp\left(c_3^k(I_4-1)^2\right)-1\right], \tag{9}$$

where c_2^k and c_3^k are material parameters, and I_4 the fourth invariant of right Green-Cauchy tensor ($I_4 = \mathbf{m}^k(\tau)\mathbf{C}^k_{n(\tau)}\left(\mathbf{m}^k(\tau)\right)^T$. Note that to maintain the same homeostatic stress in collagen, for lower values of prestretch G^k, stiffness parameter c_2^k must increase, and vice versa.

Collagen turnover plays a fundamental role in the progression of AAA, and the alteration in collagen stiffness significantly impacts the AAA geometry. When collagen becomes stiffer, it results in reduced dilatations in the circumferential direction[56]. Additionally, this change in collagen stiffness is also associated with a decrease in the length of the aneurysm. Collagen fibers have the potential to reorient themselves in the cylindrical plane, but unfortunately, the same phenomenon has not been thoroughly examined in the radial direction due to the limited availability of data on this aspect. If such reorientation were to occur, it would result in the entire compressive radial stress being borne by elastin. However, in the context of AAA disease, the loss of elastin may lead to a complete absence of elastin, further affecting the biomechanical properties of the aneurysm.

Smooth muscle cells, beside passive contribution, have the impact on the active stress with the contribution of

$$\boldsymbol{\sigma}^{active}(s) = T_m \phi^{SMC}(s)\left(1-e^{-C(s)^2}\right)\lambda^{SMC(active)}(s)\left[1-\left(\frac{\lambda_M-\lambda^{m(active)}(s)^2}{\lambda_M-\lambda_0}\right)\right], \tag{10}$$

Where the T_m represents the maximum actively generated stress, λ_M is the circumferential stretch when the active stress is maximal, λ_0 is the circumferential stretch when the active stress is zero, ϕ^{SMC} mass fraction of muscle cells, *C(s)* is the net ratio of vasoconstrictors and $\lambda^{m(\text{active})}(\tau) = \frac{\lambda^{SMC}(\tau)}{\lambda^A(\tau)}$. There are minor modifications from the original [9], where $\lambda^{m(\text{active})}$ was defined as $\lambda^{m(\text{active})}(\tau) = \frac{r^{SMC}(\tau)}{r^A(\tau)}$ where *r* represents radius. Typically, the AAA geometry is not constrained to remain axially symmetric, and as a result, the radius is not strictly defined. Moreover, to achieve a more comprehensive model, the concept of radius is substituted with stretch, which allows for a more generalized approach. Active stress values are not changed for the cylindrical geometry by this change. Stretch λ^A grows by first order rate equation, like the original

$$\frac{d\lambda^A}{\mathrm{d}s} = K^{act}\left[\lambda^{SMC}(\tau) - \lambda^A(\tau)\right] \tag{11}$$

Where $\lambda^A(0) = \lambda^{SMC}(0)$ is present in the healthy blood vessel.

2.1.2. G&R model of the ILT

Thrombus undergoes a continuous cycle of mass production and deposition in a constantly changing manner, expanding through the ongoing transformation of regularly replenished fibrinogen present in the bloodstream into fibrin. In its initial state, the blood vessel lacks any ILT, effectively attributing a mass of zero to it. As the AAA advances, the ILT mass progressively grows through a continuous deposition process. As time elapses, the thrombus undergoes a gradual transformation, organizing itself into a multi-layered structure. Three structurally distinct layers of the thrombus, each characterized by unique mechanical and proteolytic properties, can be delineated. The freshest luminal layer lies closest to the blood flow, followed by the acellular medial layer, while the oldest abluminal layer features an unorganized fibrin structure along the vessel wall. ILT is a very complex, multi-layered, continuously evolving structure composed of fibrin fibres and blood cells embedded into the fibrin mesh [57]. By employing scanning electron microscopy (SEM), Matusik et al. [7] have revealed that prevailing areas consist predominantly of a compact fibrin network, with erythrocytes being scarce within the context of AAAs.

Each thrombus layer (luminal, medial and abluminal) was histologically analysed and mechanically tested by J. Tong et al. [4]. They developed constitutive model with strain energy function defined as

$$W_{\mathrm{ILT}} = \mu(I_1 - 3) + \frac{k_1}{k_2}\left(\exp\left(k_2(I_1 - 3)^2\right) - 1\right) \tag{12}$$

with I_1 being the trace of Cauchy-Green tensor, μ and k_1 stress-like parameters and k_2 a dimensionless material parameter. Based on study by Vande Geest [44], it is assumed that the luminal layer is 2 mm thick. However, it is difficult to differentiate between medial and abluminal layers. Thus, all ILT stiffness parameters are changed with the depth of thrombus d from luminal values to abluminal ones. For example, the parameter k_1 is defined as a constant $k_{1,\mathrm{lum}}$ in the luminal layer (i.e., for $d \leq d_{\mathrm{lum}}$=2mm), and in deeper layers can be calculated as

$$k_2(d) = k_{2,\text{abl}} + \left(k_{2,\text{lum}} - k_{2,\text{abl}}\right)\exp\left[-K\left(d - d_{\text{lum}}\right)\right] \tag{13}$$

where $k_{2,\text{lum}}$ and $k_{2,abl}$ are stiffness parameters for luminal and abluminal layers, respectively, and K is a decay parameter chosen to allow for a realistic thickness of the medial layer, as measured in [4].

2.2. Numerical implementation of G&R in FEAP

The main goal of the thesis is to make a comprehensive model that can give insight into disease development, including aneurismal growth and bloods impact on the aortic wall. The complete FSG model has been implemented using two software packages: FEAP and OpenFOAM. FEAP is used for G&R simulations of the aortic wall, including ILT deposition and calculating the distribution of the wall stress, with documentation described in [58]. It is a fully open source, finite element analysis program for general use. It can be used for one, two or three dimension meshes with a wide variety of options for linear and nonlinear algorithms, linear and nonlinear elements library, shell and plate elements, thermal elements, and many others. There are several constitutive models that include linear and finite elasticity, elastoplasticity, viscoelasticity with damage. The biggest advantage is that it allows us to arbitrarily define a new material. The G&R model was incorporated into FEAP using user-defined material subroutines, providing a substantial degree of flexibility and control. These subroutines require the definition of Cauchy stress tensor and elasticity tensors at each integration point. Computational expenses come mostly from the fact that every integration point needs to be followed over time. Every constituent's kinematics and kinetics vary over time and effect blood vessel properties, so its history is important to follow. For example, production and degradation of every constituent must be known over a total time in order to be possible to know the absolute mass. A comprehensive set of 70 variables must be ascertained at every integration point, and this process is essential across different time instances to accurately capture the evolving behavior of the system.

Two types of computational models were used in this thesis for AAA modeling. The first model is a two-degree three-layered cylindrical segment with a total length of 250 mm. Initial geometry is discretized with 720 non-uniformly distributed elements (120 in axial and 6 in

radial direction through the thickness of the wall). To restrict axial lengthening or shortening of the wall, proximal–distal symmetry was assumed.

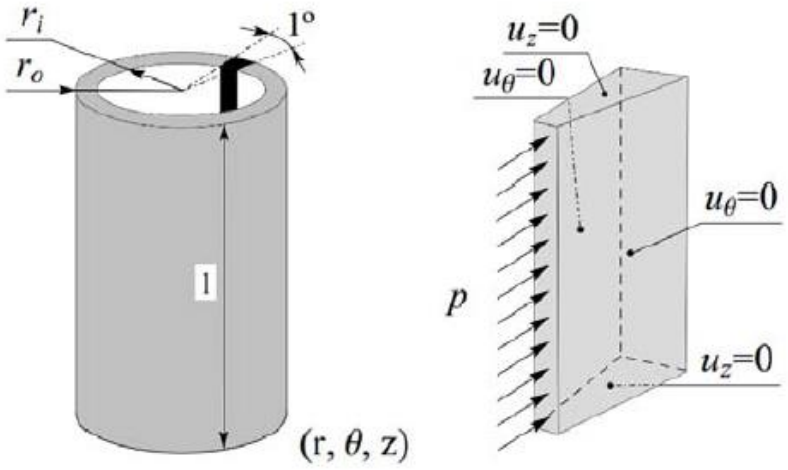

Figure 2.2 Two-degree three-layered axisymmetric cylindrical segment, *a*) as part of the whole geometry and *b*) boundary conditions

As seen from Figure 2.2, boundary conditions are set simply. On the bottom and top plane, displacement is limited to axial direction, while on sides displacement is limited to circumferential direction, due to asymmetrical boundary condition. Pressure is set from the inner side, while the p=0 is set from the outer side of the blood vessel.

Second model was used for simulation of fusiform, non-symmetric AAA, represented by a 180° three-layered cylindrical segment with total height of 350 mm. Model was discretized with 6 elements in radial, 120 elements in axial and 50 elements in circumferential direction. In the Figure 2.3 axisymmetric and asymmetric fusiform aneurysm is shown with 120x50x6 elements. The connectivity and boundary conditions set on ILT finite elements and were described in detail in [14].

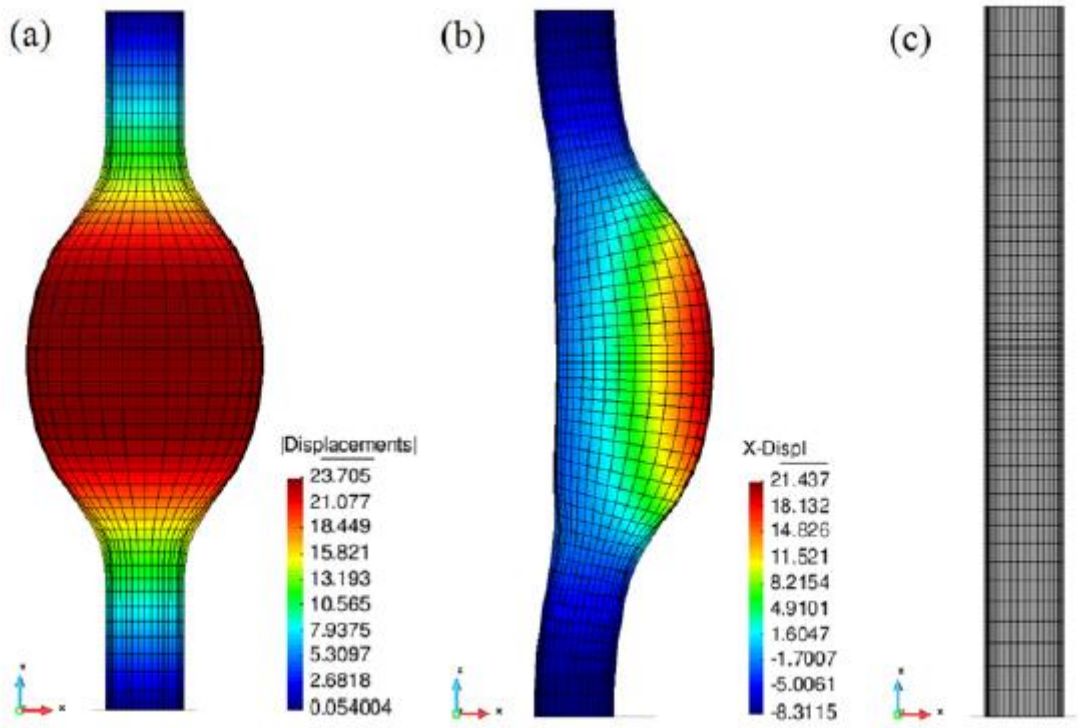

Figure 2.3 180° three-layered cylindrical segment used for saccular aneurysm simulation, *a)* symmetrical geometry, *b)* asymmetrical geometry and *c)* initial mesh in the beginning of simulation, taken from [59]

Boundary conditions are similar to axisymmetric case, but due to full 3D geometry, there is no circumferential constraint at the sides. Finally, there are displacement only at the bottom and top planes where the displacement is restricted in both directions, axial and circumferential. Both cases were discretized with the same 3D hexahedral elements, Q1P0.

2.3. Computer fluid dynamics (CFD)

2.3.1. Blood in general and its properties

Blood plasma is a yellowish liquid that is obtained by removing blood cells, and it mostly consists of water (about 90%), while the other 10% is made up of proteins, glucose, and inorganic salts. Precisely because of the large proportion of blood plasma, blood and water have certain physical similarities properties. Blood plasma contains about 5% of the total body mass of an adult. In addition to plasma, the properties of blood are given by blood cells, mainly red

and white blood cells, and platelets. Red blood cells (erythrocytes) are the most numerous and largest of the three cellular constituents and make up almost half of the blood volume. These cells are filled with hemoglobin, which enables them to carry oxygen from the lungs and deliver it to all body tissues. White blood cells (leukocytes) are contained in significantly lower numbers: one white blood cell for every 660 red blood cells. There are five main types of white blood cells, and they are key to the immune system and provide the body with a mechanism to fight infections, including the creation of antibodies. Blood platelets (platelets) are cell fragments without a nucleus that are produced in the bone marrow. They are part of the protective mechanism to stop bleeding, they collect at the site of injury where they are activated and start the process of blood coagulation. The ratio of blood plasma and blood cells is shown in Figure 2.4.

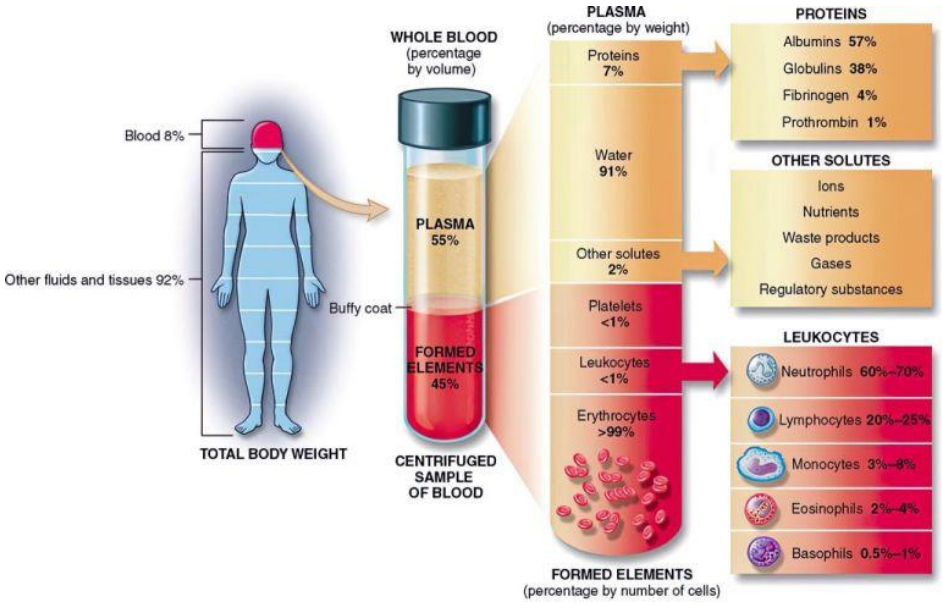

Figure 2.4 Blood components, taken from [60]

The heart is the central part of the cardiovascular system. It is a muscular organ about the size of a human hand. It is in the central part of the chest cavity, between the two lungs, as shown in Figure 2.5. It is made of a special type of muscle tissue - cardiac muscle tissue consists of left and right halves. Each half consists of chambers called ventricle (larger) and atrium (smaller). Between the atrium and the ventricle are heart valves that prevent the return of blood in the opposite direction. The heart works throughout life without stopping, pumping blood alternating contraction and relaxation of the atria and ventricles. The speed of work depends on the needs of the organism. The work of the heart accelerates due to physical effort when the body's need for nutrients and oxygen. In a state of rest, the average number of beats is 60-80

times in minutes. Blood flow at the entrance and pressure at the exit have a pulsating character due to the way the heart works.

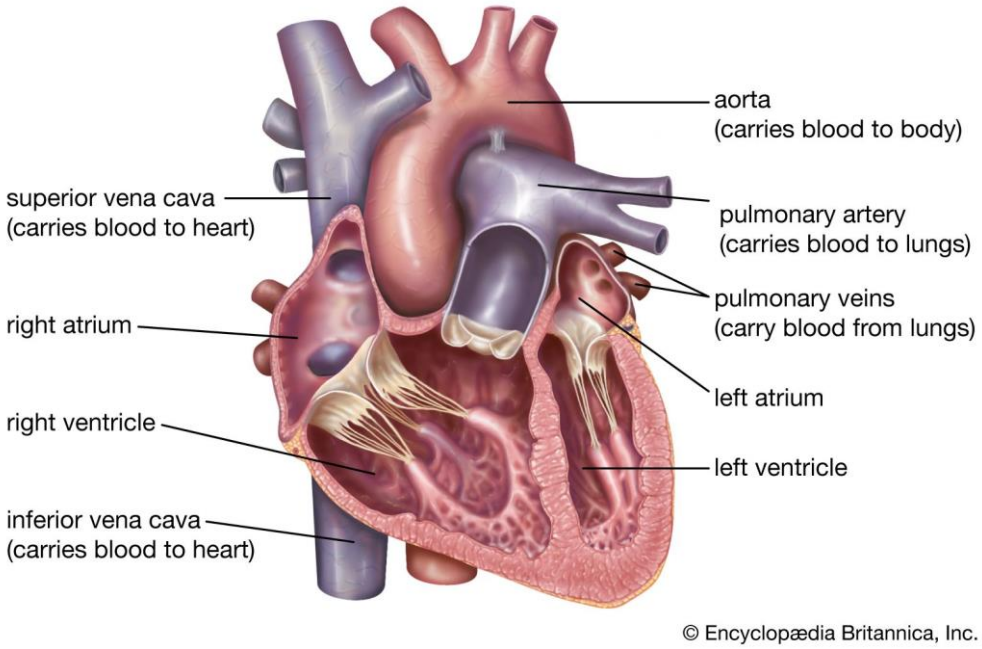

Figure 2.5 Heart anatomy, taken from [61]

Human blood flow has extremely unsteady and complex behavior so therefore mathematically describing blood flow is a very complex task. In addition, aorta and other blood vessels have extremely irregular geometry due to several curvatures and branching. Determining the blood flow model depends on a case-by-case basis. Blood in larger blood vessels (arteries) shows different behavior than in small ones because of non-uniform distribution of red blood cells (RBC), erythrocytes and blood flow velocity. In addition, sex, diet, use of anticoagulants, and even the time of the day affects blood properties. According to Yamamoto et al. [36] blood flow models can be divided into three regions: Casson (non-Newtonian), transient and Newtonian range, based on shear rate. For shear rate $\gamma < 140\ \mathrm{s}^{-1}$ Casson blood viscosity model is optimal, transient model should be used for shear rates $140\ \mathrm{s}^{-1} < \gamma < 160\ \mathrm{s}^{-1}$, and Newtonian fluid range for shear rates $\gamma > 140\ \mathrm{s}^{-1}$. Blood kinematic viscosity is known to vary in range of $\left[3\cdot10^{-6}\ \mathrm{m}^2/\mathrm{s} - 6\cdot10^{-6}\ \mathrm{m}^2/\mathrm{s}\right]$ for the certain velocity but it also changes from shear rate depending on the geometry. Since the wall shear stress is directly correlated to viscosity; it may bring major changes to the model. On the other hand, for situations when viscosity forces are dominated over inertia, like in smaller blood vessels, non-Newtonian blood model is more suitable. Additionally, the presence of strong temporal variations necessitates the use of non-

Newtonian rheological models to better capture the effects of temporal variation phenomena, which can be crucial. In addition, non-Newtonian rheological models, such as Casson may show better results for accounting low shear-rates.

Most used, Newtonian viscosity model is defined with a linear relationship between viscosity coefficient and shear rate value. That means that small difference in viscosity coefficient can cause difference in wall shear stress.

$$\tau = \mu \frac{du}{dy} = \mu \dot{\gamma} \,, \tag{14}$$

where τ is shear stress, μ is dynamic viscosity and $\frac{du}{dy}$ or $\dot{\gamma}$ is rate of shear deformation. The drawback of employing the Newtonian viscosity model lies in its sensitivity to shear rate, making it essential to determine the shear rate beforehand. Furthermore, viscosity variations are observed based on factors such as gender, the use of anticoagulants, and the time of day. Despite these differences, both males and females, with or without anticoagulants, exhibit a substantial increase in viscosity for shear rate values below 100 s^{-1}, as shown in Figure 2.6.

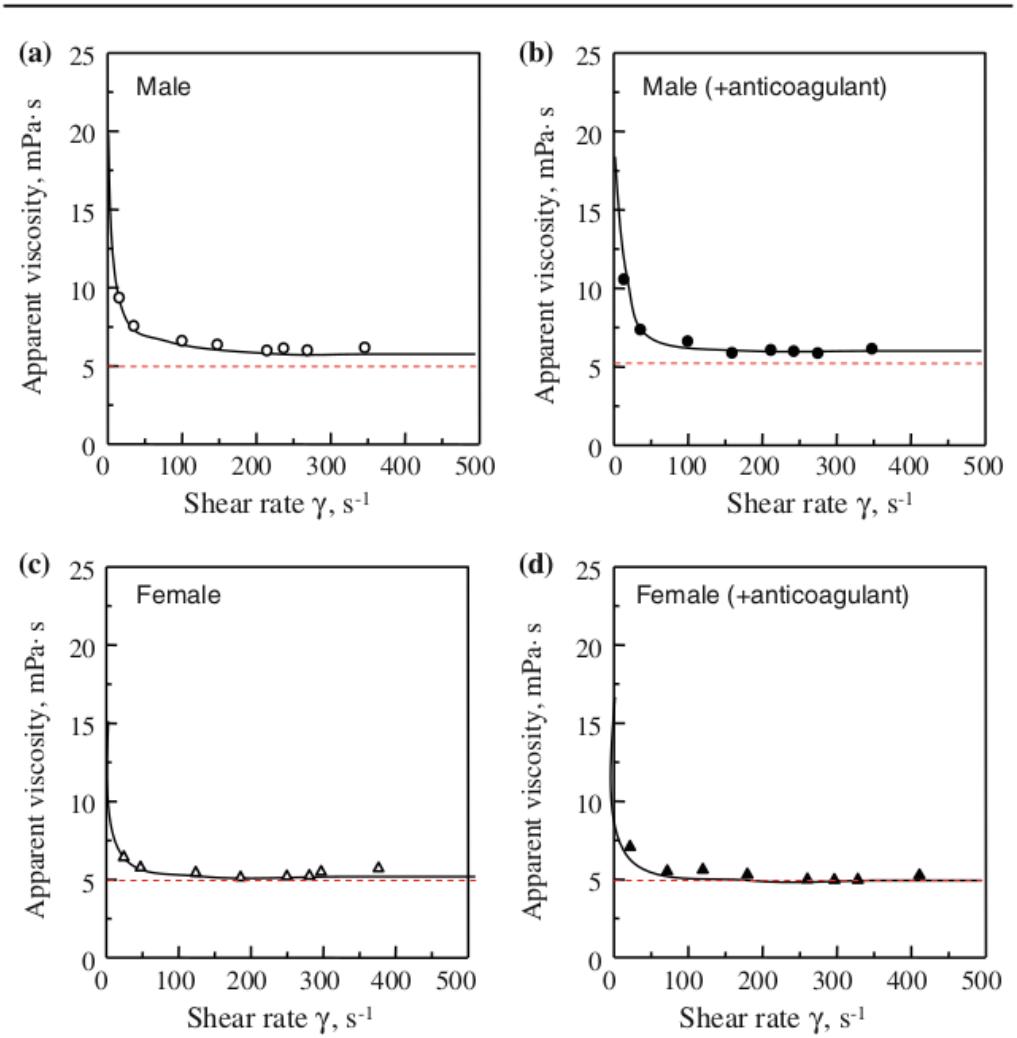

Figure 2.6 Viscosity and shear rate dependence for Male without coagulant *a*), Male with coagulant *b*), Female without coagulant *c*), Female with coagulant *d*), taken from [36]

In this scope of work, two additional rheological models will be considered. First is the basic and most popular rheological model, Casson. Casson model specifies minimum and maximal kinematic viscosities, $\nu_{\min}$ and $\nu_{\max}$. Beyond a threshold in strain-rate corresponding to threshold stress τ_0. The viscosity is described by a square-root relationship. The model is mathematically described as:

$$\nu = \left(\sqrt{\tau_0 / \dot{\gamma}} + \sqrt{m}\right)^2 \qquad \nu_{\min} \le \nu \le \nu_{\max}, \tag{15}$$

where *m* is the constant index. The Casson model is a three-parameter model with a yield stress and two rheological parameters. A Casson fluid is a shear-thinning liquid which is assumed to

have an infinite viscosity at zero rate of shear, a yield stress below which no flow occurs, and a zero viscosity at infinite shear rate.

Another rheology model that is often used is Bird-Carreau. This is a four-parameter model that is valid over the complete range of shear rates. It comes to significance when the shear rate is very high or very low, and then it becomes significant to essential to incorporate the values of viscosity at zero shear ν_0 and infinite shear, ν_∞. The mathematical formula for Bird-Carreau viscosity model is written as

$$\nu = \nu_\infty + (\nu_0 - \nu_\infty) \times \left[1 + (k \cdot \dot{\gamma})^a\right]^{(n-1)/a}, \tag{16}$$

where the coefficient *a* has a default value of *a*=2 and it corresponds to the change from linear behavior to power law.

The correct choice of the viscosity model is crucial as it directly influences the blood flow patterns on the aneurysmal surface, impacting the initiation of ILT formation. The ILT formation process initiates when damage occurs to the blood vessel's endothelium, primarily attributed to sustained high wall-shear stress over time. After the initial endothelium tearing, low wall shear stress is needed for platelets activation to start ILT formation. Additionally, ILT grows because the renewed blood fibrinogen turns into fibrin. According to that, ILT is deposited continuously with its mass changing up to fill potentially big AAAs (over 50mm in diameter). Quite simplified, one of the most used ILT formation criterion is time-average wall shear stress (TAWSS) through the cardiac circle, used by Di Achille et al. [25] which is calculated as

$$\mathrm{TAWSS} = \frac{1}{T}\int_0^T |\tau_\mathrm{W}|\, dt, \tag{17}$$

where is duration of one cardiac cycle, although time of several cycles can also be chosen. They stated 0.4 Pa as a critical value bellow which ILT starts to deposit. This will serve as the starting point s the ILT deposition criteria for the upcoming FSG simulations. The same group analysed several other criteria, such as oscillatory shear index, successful in identifying atheroprone regions of the vasculature, defined as

$$\mathrm{OSI} = \frac{1}{2}\left(1 - \frac{\left|\int_0^T \tau_W dt\right|}{\int_0^T |\tau_W| dt}\right), \tag{18}$$

Additionally, by combining these two parameters they obtain parameter endothelium cell activation potential (ECAP), defined as the ratio of the previous two parameters,

$$\mathrm{ECAP} = \frac{\mathrm{OSI}}{\overline{\overline{\mathrm{TAWSS}}}}, \tag{19}$$

In equation (19) , is a point-wise normalized value of time averaged wall shear stress by the mean value of TAWSS in descending (i.e., healthy) aorta, as defined in Bhagavan et al. [26]. For OSI and ECAP there is no suggested threshold value to use connected to ILT deposition.

Blood originally belongs to the non-Newtonian fluid because of the many blood cells contained, but according to Skiadopoulos et al. [62], Newtonian viscosity model is suitable for describing blood flow when wall shear stress and blood velocity have generally greater values. On the other hand, one negative thing is that using the Newtonian model overestimates the occurrence of diseases. According to Liepsch et al. [63], average differences in blood flow between the Newtonian and non-Newtonian models of about 12%. But the difference between difference in slow speed regime is much more, 20% to even 63%. However, Jahangiri et al. [64] concluded that there is not significant difference in rheological models when carried out a numerical test of a pipe flow and non-Newtonian models (Carreau, Carreau-Yasuda, modified Casson, Power law, generalized power law, and Walburn-Schneck) showed very similar results in axial velocity profile and WSS. The only exception was the generalized power law model. Lately, Mendieta et al. [65] made a comparison between 4 rheological models with focus on the wall shear stress. The Newtonian model was compared to several non-Newtonian. The OSI exhibited the most significant disparity, particularly in terms of maximum and mean values. Surprisingly, the difference in TAWSS was less than 6%. In conclusion, the Newtonian viscosity model proves suitable for regions with high TAWSS, while the non-Newtonian model becomes necessary for low TAWSS. Zambrano's findings suggest a correlation between ILT deposition and low TAWSS values.

2.3.2. Turbulence properties

Turbulent flow represents a form of fluid motion marked by recirculation, the formation of eddies, and seemingly random fluctuations, introducing irregular and chaotic behavior. This contrasts with laminar flow, where the fluid moves in orderly, smooth paths or parallel layers. The Reynolds number, indicating the ratio of inertial forces to viscous forces, is a crucial parameter in determining the nature of the flow. Unsteady laminar flow involves changing velocities, yet the fluctuations in velocity differ from the turbulent flow, where the fluctuations exhibit a more complex and erratic pattern.

The blood flow regime within the blood vessel system is riddled with uncertainties, given the diverse array of blood components, intricate blood vessel geometry, and the pulsatile nature of the flow. Determining a single model becomes challenging due to the complex interplay of these factors. The intricate geometry leads to the formation of vortices, activating platelets in high WSS regions and causing their accumulation in low WSS areas. Consequently, turbulence effects may play a role and should be considered. While laminar models are commonly employed in healthy aortas, the presence of geometrical irregularities in vascular diseases suggests the existence of a turbulent flow regime. Although laminar flow is frequently used in research, particularly with standard shear rheometers, it may not fully capture the complexities associated with vascular diseases. In addition, it was noted by Agarwal et al. [66], that the shear-rate is precisely specified as it is and exclusively depends on rotational speed. Molla and Paul [64], in contrast, observed turbulent flow in a constricted channel and computations. In their study, the researchers compared five distinct rheological models, analyzing parameters such as pressure, regions of re-circularization, turbulent kinetic energy, as well as mean and peak shear-rate results. Their findings indicated a reduction in post-stenotic recirculation regions for the various rheological viscosity models, accompanied by a decrease in turbulent flow kinetic energy downstream of the stenosis. Initially assuming laminar blood flow characteristics in larger-diameter blood vessels, they observed a contrary trend, with turbulent blood flow being more prevalent in smaller blood vessels. Furthermore, the smaller blood vessel radius was associated with more regular geometry and fewer fluctuations, resulting in reduced turbulence overall. This examination will be extended to larger AAA in a subsequent stage to approach the turbulent nature of the flow. The selected geometry for this analysis will be consistent with the example in which shear-rate was examined, as detailed chapter 5.2. Given a maximal radius of 15 mm, the potential for turbulence becomes more pronounced.

The solver used in OpenFOAM package is PIMPLE algorithm, which combines PISO and SIMLE algorithms. PISO uses a pressure-implicit split-operator while SIMLE uses semi-implicit method for solving pressure-linked equations. Both algorithms use iterative procedures for solving coupling equations for momentum and mass conservation. PIMPLE is a transient solver for incompressible, turbulent flow of Newtonian fluids on a moving mesh. The solver is used to solve the continuity equation and momentum equation. Continuity equation is written following

$$\nabla \cdot \mathbf{u} = 0, \tag{20}$$

and the momentum equation

$$\frac{\partial}{\partial t}(\mathbf{u}) + \nabla \cdot (\mathbf{u} \otimes \mathbf{u}) = -\nabla p, \tag{21}$$

Where the **u** is velocity vector and p is pressure. Algorithms solve pressure equations until given time or solution, to secure mass conservation. Securing momentum conservation equation is obtained by explicit velocity equation and each step begins by solving the momentum equation.

k-ω SST turbulent model was used for turbulence modeling. It is a combination of the k-ω turbulent model and shear stress transport (SST) equations. k-ω turbulence model belongs to the vastly used two-partial-equation turbulence model. They present simplified Reynolds-averaged Navier–Stokes equations (RANS equations). There are two variables: k represents turbulence kinetic energy and ω represents dissipation specific rate that represents how much turbulence kinetic energy is converted to thermal energy. k-ω model has the advantage of computing turbulences both in the inner part of lumen and near the wall, so the model is possible to use all the way till the boundary layers close to wall. For isotropic turbulence, the turbulence energy is written as

$$k = \frac{3}{2}\left(I\,|\mathbf{u}|\right)^2, \tag{22}$$

where the I is the turbulence intensity and the $|\mathbf{u}|$ is the initial velocity magnitude. Turbulence dissipation is written,

$$\omega = \frac{\sqrt{k}}{C_{\mu}^{0.25} L}, \tag{23}$$

where the $C_{\mu} = 0.09$ is a constant and L is a reference length scale.

2.4. Numerical implementation of CFD in OpenFOAM

The blood flow and CFD analyses are conducted using the OpenFOAM v2012 software, an open-source program developed in the C++ programming language by Weller [67]. Like FEAP, OpenFOAM is a comprehensive open-source program offering extensive capabilities for integrating custom user functions. It is founded on the finite volume method (FVM), encompasses a range of solvers with varying accuracy levels, both first and higher order. The program incorporates multiple built-in viscosity models to describe blood flow, including the Newtonian viscosity model, as well as Bird-Carreau and Casson's. The ILT criteria are directly derived from the interaction of blood with the wall, exerting a substantial influence on the model. Therefore, ILT formation criteria, TAWSS, OSI and ECAP, had to be subsequently implemented. The initial phase of constructing the CFD and FSG model involves a thorough investigation to identify optimal model assumptions. Critical decisions include determining whether blood flow in AAA leans toward a laminar or turbulent regime, assessing the suitability of viscosity models, and selecting parameters for the FSG model. The complexity arises from the interdependence of these assumptions, making it challenging to isolate a single factor without considering the others.

In this study, a second-order Crank–Nicolson scheme with a blend coefficient of 0.9 was employed for time discretization to balance accuracy and stability. Spatial gradients were computed using a least squares gradient scheme, while convective terms for velocity and turbulence variables (k and ω) were discretized with a *linear-upwind* approach in combination with least squares. Diffusive terms were handled using a linear Gauss scheme, and the Laplacian terms were resolved with the Gauss linear corrected scheme. Finally, a linear interpolation scheme was applied to maintain consistency and accuracy.

2.4.1. Finite volume elements

The OpenFOAM mesh is generated directly from the FEAP wall geometry after each timestep. The luminal surface is exported as an STL file, from which a new mesh is automatically generated using the *blockMesh* tool. As the current FSG model is designed for axisymmetric cases, wedge elements are utilized, and the mesh is more finely distributed in the middle height area and near the wall to capture wall-shear-stress more effectively. The final mesh consists of 121 elements in the axial direction and 30 in the radial direction, with a cell expansion ratio set to 0.2 in the radial direction. The mesh has been thoroughly verified to ensure mesh independence on the mesh elements. While OpenFOAM is primarily designed for three-dimensional analyses, it can effectively handle asymmetrical problems by employing special boundary conditions on patches in planes normal to the direction of interest, as stated in [68]. Specifically, this problem will utilize the wedge patch type, as illustrated in the Figure 2.7.

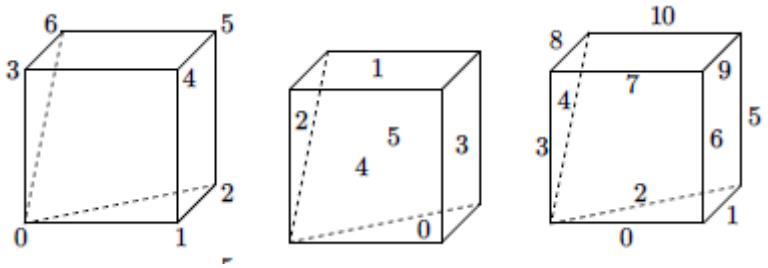

Figure 2.7 OpenFOAM wedge elements, taken from [68]

Figure 2.8 The model showcases a lumen with a maximal inner radius of 15mm and length of 250mm, dimensions that are utilized in a representative CFD analysis case.

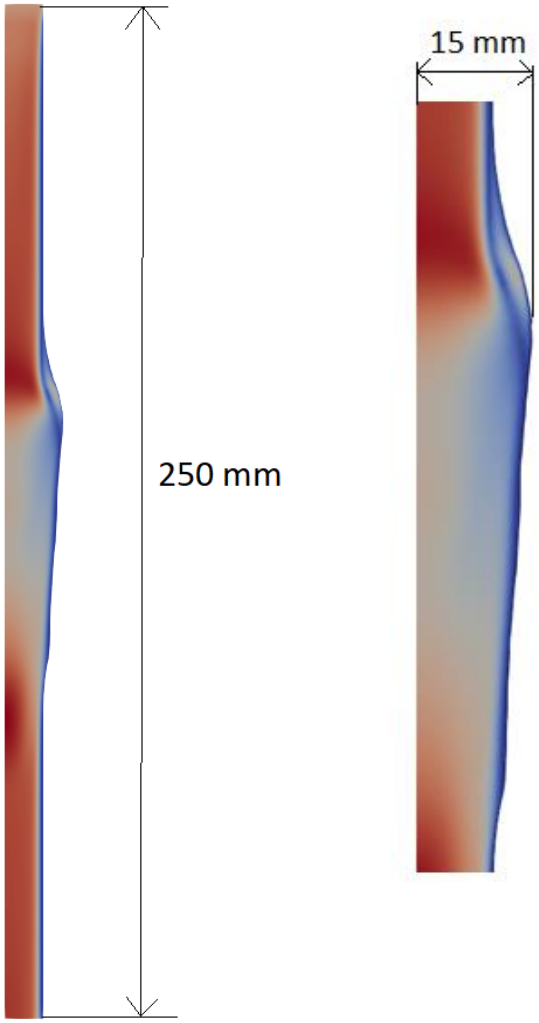

Figure 2.9 Blood vessel geometry and dimensions used in CFD analysis

Details from the OpenFOAM mesh used in the FSG simulation, with the maximal inner radius 15 cm is shown in Figure 2.10.

The CFD geometry can be described as semi-idealized; it starts as a regular cylinder and undergoes transformations over time. However, due to the flat surfaces of the elements and their stacking, geometry cannot be considered fully realistic. With each ILT deposition, new elements are introduced into each G&R simulation. However, this iterative process does not necessarily result in a geometry that accurately mimics that of an actual patient.

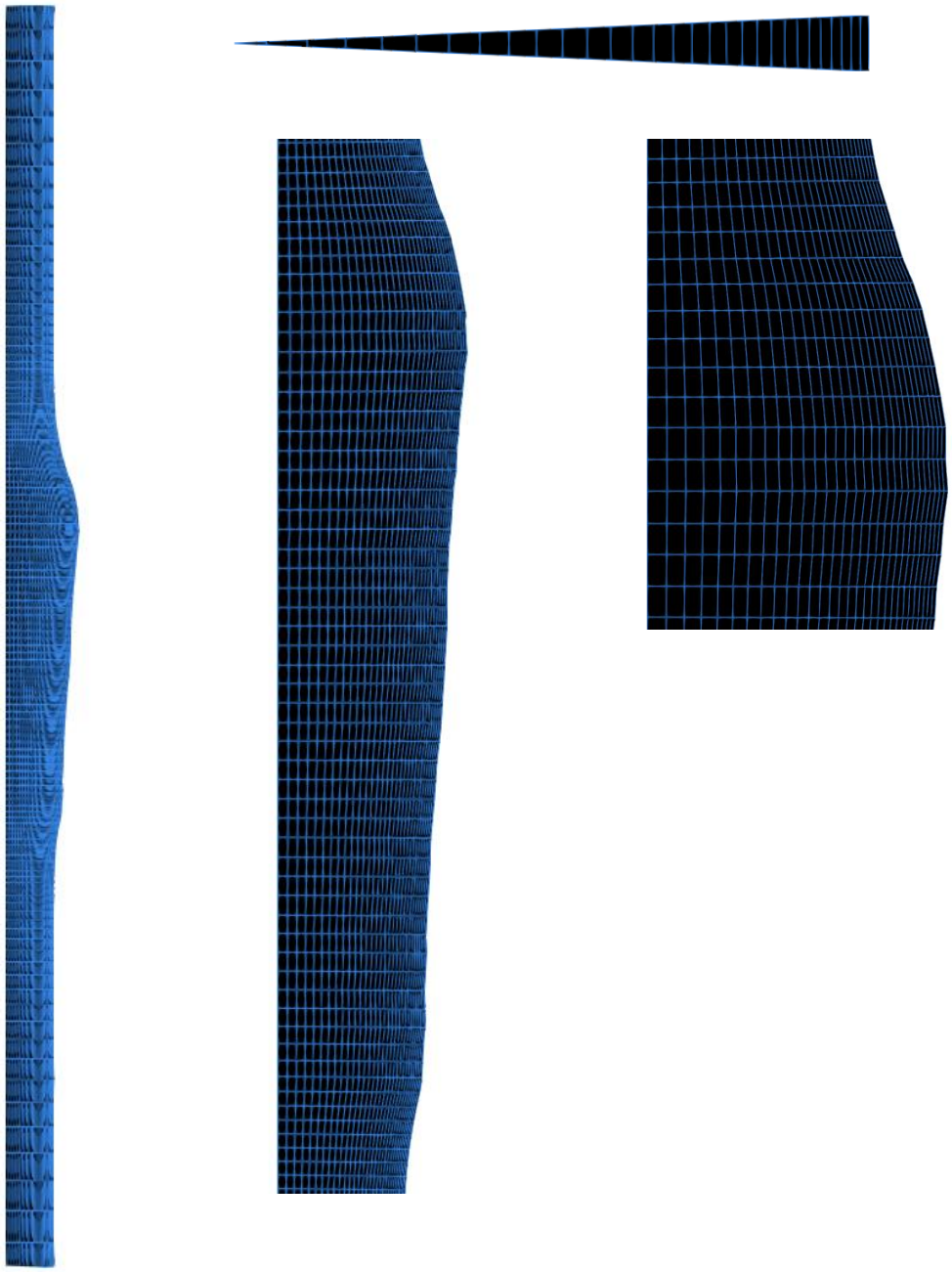

Figure 2.10 Wedge elements mesh; 121 axial and 30 radial elements with 0.2 cell expansion ratio in radial direction.

Each simulation settings and boundary conditions used are explained in chapter 4.1.

2.5. Incompressibility

2.5.1. Introduction on incompressibility

Numerical modeling of blood vessels is highly challenging due to the need to consider a dynamic and complex structure that evolves over time, often with an incompletely known composition. For numerical modeling of such materials, it is necessary to use assumptions of large deformations and non-linear behavior of the material. Moreover, the incompressible behavior of the blood vessel wall adds another layer of complexity to numerical modeling. Simulating blood flow through the vessel wall requires employing FSI numerical simulations, posing further challenges. To enhance the efficiency of numerical FSI simulations, it is demonstrated that incorporating models of blood vessel behavior into control volume packages is essential. OpenFOAM package will be used, although the formulation is not limited to it. One of the problems that appears during the formulation of the numerical model is ensuring the incompressibility of the blood vessel wall. The focus here is to show the influence of incompressibility on the obtained results through a G&R and to develop a formulation that ensures the accuracy of the results for incompressible materials. Currently, the standard OpenFOAM package lacks a built-in model for simulating incompressible behavior, necessitating the need for implementation. The implementation of incompressible behavior was done through two steps; first in a linear elastic model which was subsequently extended for nonlinear material behavior. Henry and Collins [69] described a numerical procedure for solving axisymmetric problems on incompressible materials with the aim of stress analysis for the blood flow problem. Bijelonja, Demirdžić i Muzaferija [40] successfully developed a formulation of the control volume method that eliminated the previous shortcomings, and this formulation was implemented in the OpenFOAM library.

2.5.2. Incompressibility in FEAP

For G&R simulations in FEAP program package, 8-node, 3D hexahedral element (Q1P0) was used with three degrees of freedom at each node. Displacement, enhanced, and mixed strain formulations enable solid elements in FEAP. Aortic wall shows incompressible behaviour, so appropriate, locking free finite element formulation was used: mixed formulation using Hu-Washizu variation principle. Hu-Washizu is based on principle where displacement is present

up to first derivatives, but stress and strains are present without any derivatives. It follows that displacement will have the values of C^0, while stress and strain will have C^{-1} in the terms of continuity conditions. The following are interpolations for each element as

$$u(\xi) = N_I(\xi)\mathbf{u}^I(t), \tag{24}$$

$$\sigma(\xi) = \phi_\alpha(\xi)\sigma^\alpha(t), \tag{25}$$

$$\varepsilon(\xi) = \psi_\alpha(\xi)\varepsilon^\alpha(t), \tag{26}$$

where $\phi_\alpha(\xi)$ and $\psi_\alpha(\xi)$ represents continuous interpolations in each element. Parameters σ^α and ε^α may not have physical meaning because they are not necessarily notal values. Now, the change in pressure and volume in each element can be described as following

$$p(\xi) = \phi_\alpha(\xi)\, p^\alpha(t), \tag{27}$$

$$\theta(\xi) = \phi_\alpha(\xi)\theta^\alpha(t), \tag{28}$$

where the same approximating function is used for pressure and volume. Using the linear elastic material will fully satisfy the constitutive equation in every point of the element domain. For more complex material models, constitutive equations will be approximately satisfied.

2.5.3. Incompressibility in FVM

This chapter focuses on implementing the finite volume method for modeling the blood vessel wall. To achieve this, the existing G&R model was simplified, and numerical simulations were conducted using simplified examples. In essence, the influence of fiber structures (collagen and smooth muscle cells) was neglected in the composition of the wall. Consequently, only elastin degradation is considered, while its production is excluded. The free deformation energy can then be written as

$$W = C(I_1 - 3) + p(J - \Phi)^2, \tag{29}$$

Where the C is material parameter, $\Phi = e^{-t/\tau}$ is the elastin degradation function, J is the Jacobian matrix, I_1 is the first Cauchy-Green stress tensor, defined as

$$I_1 = \mathbf{G} \cdot \mathbf{C} \cdot \mathbf{G}\,, \tag{30}$$

Where the G is elastin pre-stretch tensor and C is the right Cauchy-Green tensor. Material model was implemented into OpenFOAM package. The library that was used for analysis is *solidFoam* and can be used for many different models.

During the work on incompressible models, there was a need to implement a model that can provide the accuracy of the results for nearly incompressible deformation. The initial phase involved implementing the incompressibility model for small displacements and deformations in the *elasticSolidFoam* library. This library is used for analyzing material strength issues within the linear-elastic range. By introducing specific constitutive relations for stress in the momentum equation and considering the assumption of incompressibility with a constant distribution μ, the moment equation took the following form:

$$\frac{\partial}{\partial t}\int_\Omega \rho \frac{\partial \mathbf{u}}{\partial t}\,\mathrm{d}\Omega = \int_\Omega \nabla \cdot \left|\mathrm{grad}\mathbf{u}\right|\mathrm{d}\Omega - \int_\Omega \nabla \mathbf{p}\,\mathrm{d}\Omega + \int_\Omega \rho \mathbf{f}\,\mathrm{d}\Omega \tag{31}$$

Where **u** is the displacement vector, ρ is density and f are volume force.

2.5.4. Numerical example - aging of the aorta

Elastin is produced only in prenatal period and has a significantly longer half-life compared to collagen and muscle cells. As the vessel ages, it loses elastin, which cannot be replaced, and as a result, the healthy blood vessel expands. As an example, the case of simplified breakdown of elastin in the vessel without the creation of a new one will be shown, and the influence of collagen and smooth muscle cells will be ignored. A mean constant pressure of p=100 mmHg is taken as the load on the blood vessel. We model the blood vessel wall as a single-layer model with an inner radius r_i=10 mm and a wall thickness h=1.2 mm. The stiffness of the wall is represented by the material parameter C=55kPa, according to [23]. Additionally, an elastin prestretch of 40% in circular and axial directions was assumed, determining the half-life of elastin for numerical simulation of its decomposition. To assess the impact of incompressibility, the results obtained through the FVM were compared with the semi-analytical solution from

[70]. Numerical simulations in OpenFOAM were performed for different cases of compressibility ($\nu = 0,495$ and $\nu = 0,4995$).

In the first step, an aging simulation was made where elastin pre-stretch was neglected. Figure 2.11 shows the dilation of the blood vessel, characteristic of aging. When comparing the results obtained by the FVM with the semi-analytical solution, a smaller deviation is noticeable. Moreover, there is a noticeable deviation in the solutions for different Poisson's factors. A more significant difference in the change of the radius is observed for larger time steps, with a noticeable discontinuity for the material with a Poisson's factor, $\nu = 0,4995$ is also visible.

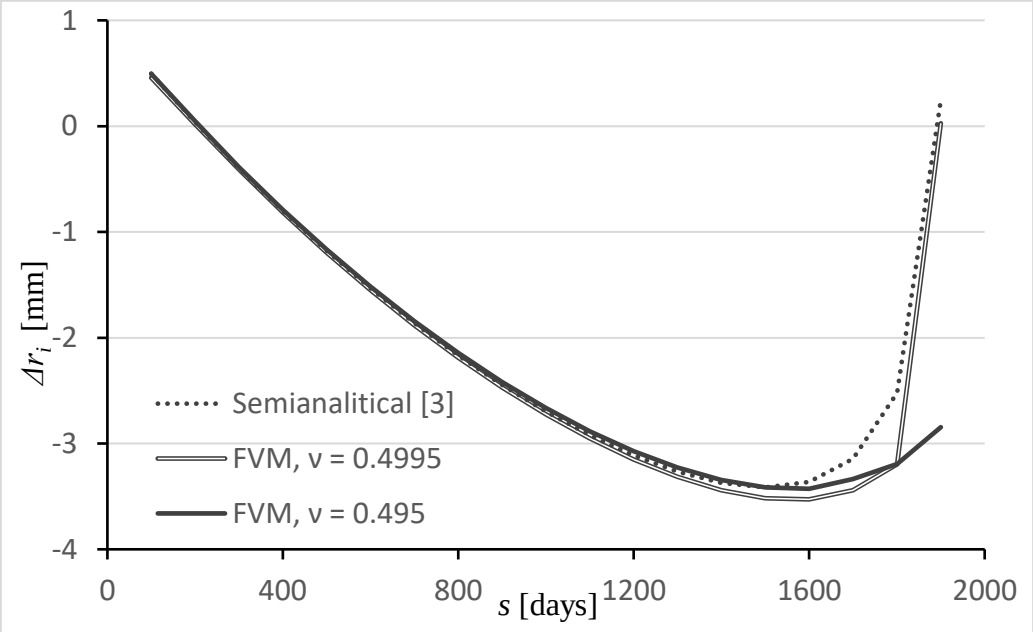

Figure 2.11 inner radius dilatation for the case without elastin pre-stretch

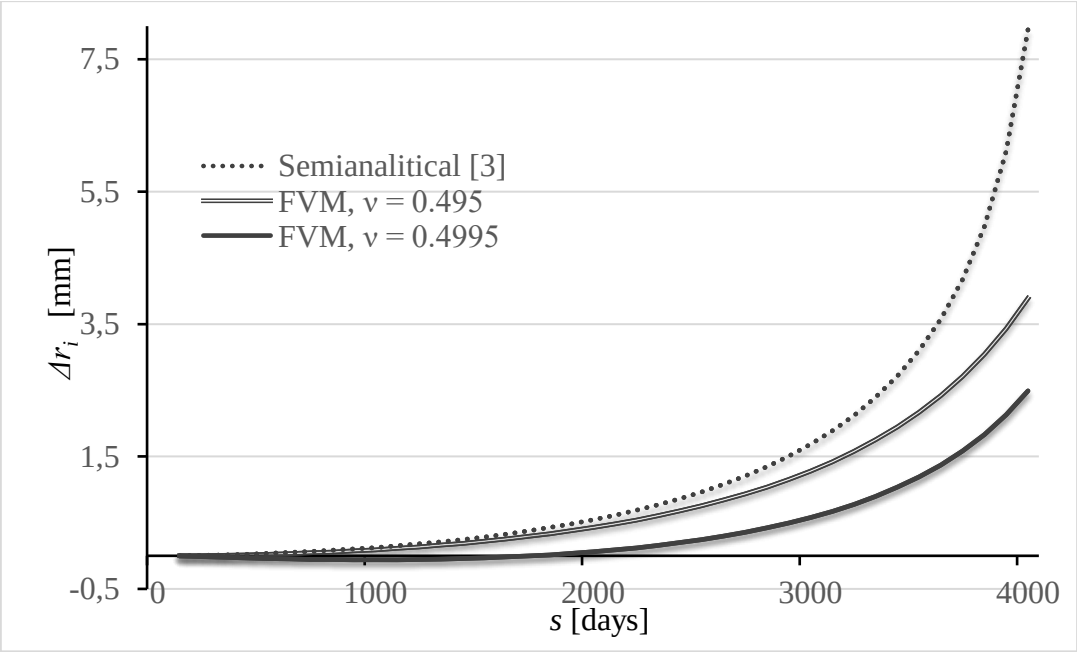

Figure 2.12 Inner radius dilatation, for pre-stretch 40%

In the second step, the influence of elastin pre-stretch on the simulation results was investigated. An elastin pre-stretch with the value of 40% was used. Figure 2.12 shows a comparison with the semi analytical solution, taken from [70]. From the results in Figure 2.12, the deviation of results increases with the rise of Poisson's factor. This discrepancy is associated with the absence of a model in OpenFOAM that can describe incompressible flow. The error in the OpenFOAM package becomes more pronounced at later time steps.

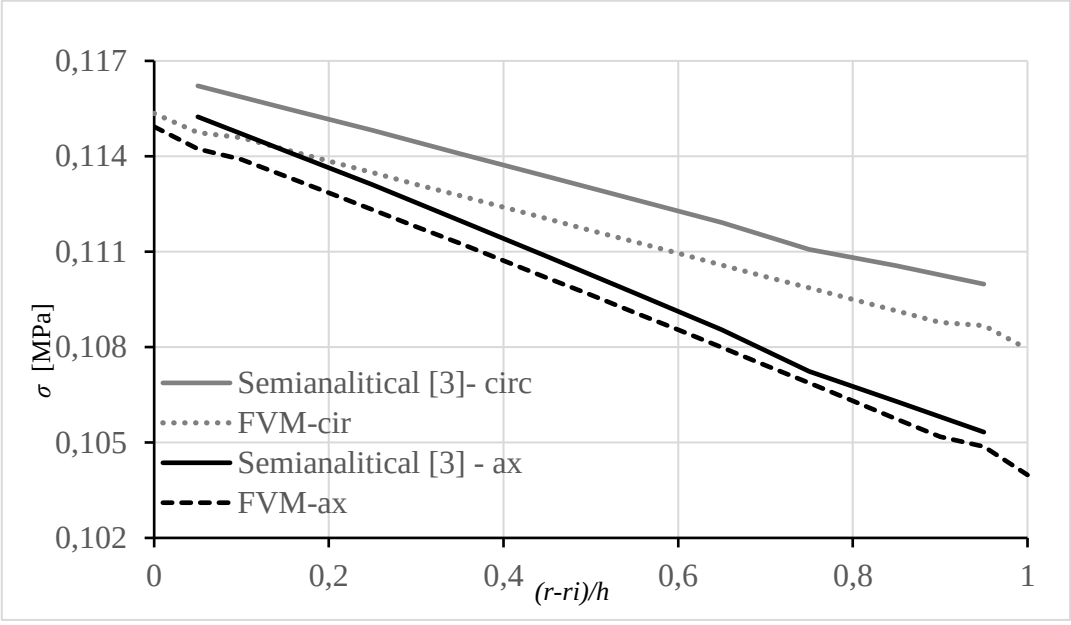

Figure 2.13 Circular and axial stress distributed across the vessel thickness

Additionally, the stress distribution through the blood vessel wall was investigated, as shown in Figure 2.13. When comparing the circular and axial stress across the thickness of the blood vessel wall, the stress values partially differ over the entire area, and there are additional peaks in the stress value in the outer part of the wall. It is important to note that the solution was approached using the *Updated Lagrangian* [71] formulation due to smaller stress oscillations.

2.5.5. Summary on incompressibility

In this chapter it was presented the finite volume method for large deformations, common in the field of biomechanics. The library *elasticSolidFoam* from OpenFOAM was used as a solver, lacking a defined model for describing the incompressible behavior of the material. The results demonstrated that the current method introduces deviations, particularly in stress values, stemming from a notable numerical error. It is crucial to adapt and implement the incompressibility formulation in the solver to achieve valid results. This method has been successfully implemented for small deformations, addressing issues like "locking" and stress oscillations inherent in standard incompressible models.

2.6. FSG model

2.6.1. Overview

This chapter will introduce the primary objective of the thesis, outlining the *Fluid-solid-growth* framework and its application to the evolution of thrombus-laden aneurysms. The FSG model comprehensively captures alterations in the aortic wall due to disease, the blood flow pattern within the vessel lumen, and ILT formation based on blood flow parameters. The interdependence of all three components within the FSG model creates a mathematically and numerically intricate framework. This model dynamically captures the growth and remodeling responses of the aortic wall to the irreversible loss of elastin while incorporating thrombus finite elements at specific times and locations identified through CFD analysis. Hemodynamics is undoubtedly an important factor in progression of many cardiovascular diseases. For instance, it is theorized that atherosclerosis develops at sites with complex flow fields due to low WSS and WSS gradient. Both low and high WSS are associated with the growth of intracranial aneurysms, as well as the formation of intraluminal thrombus in aneurysms and dissections.

Consequently, there is a demand for a framework capable of elucidating the evolving geometry, spatio-temporal alterations in wall properties, and hemodynamics that govern cell mechanobiology, leading to imbalanced matrix turnover or thrombus deposition. Figure 2.14 schematically shows the three main parts of the FSG model ant their interaction.

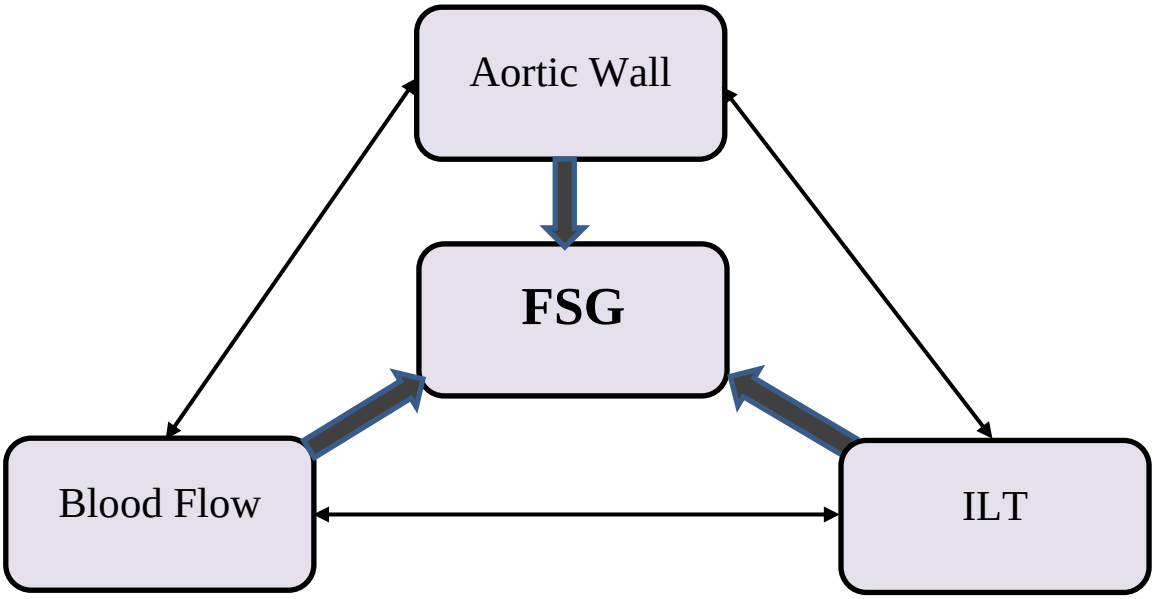

Figure 2.14 Schematic representation of the FSG model

The main goal of this work is to present the general FSG model, which will be applied to thrombus-laden AAA growth based on the CFD blood flow analysis. The study investigates the impact of different model definitions on the results and explores thrombus deposition in relation to parameters such as TAWSS, OSI, and ECAP. It's worth noting that the computation of PLAP requires a dynamically load-balanced particle tracking code, and thus, PLAP and related TFP are not considered in this study. Additionally, the investigation explores how changes in flow fields influence the shape of AAA, subsequently affecting thrombus deposition patterns, shapes, and volumes.

2.6.2. FSG Methodology

The FSG model involves a long-term G&R model of the evolving wall (time scale in days) with a loose coupling of CFD analysis spanning several cardiac cycles (time scale in seconds). Unlike CFD analysis, fluid-structure interaction (FSI) accounts for the compliancy of the arterial wall, resulting in more accurate wall shear stresses. However, for patient-specific cases, the arterial material parameters can be highly heterogeneous and unknown. In this work, considering that threshold values for thrombus deposition were estimated using CFD analyses, the wall was assumed to be rigid during hemodynamic analyses.

The initial, healthy aortic blood vessel is represented by an axisymmetric, 2-degree geometry with an initial radius is r = 10 mm and height h=250 mm. The finite element mesh for the G&R simulation consists of 726 elements, with 121 in the axial and 6 in the radial direction, excluding any ILT elements. The mesh exhibits finer resolution in the central area where the aneurysm will develop and coarser resolution at the ends. Notably, the number of aortic wall elements remains constant regardless of the shape and AAA size during its growth. Conversely, ILT elements are added based on ILT deposition and growth criteria.

The starting point of the FSG simulation involves configuring the model parameters for both the G&R and the CFD models, as well as ILT deposition criterion. To conduct the CFD analysis, the luminal surface is exported as an STL geometry, and a new mesh is generated from the STL file. It is important to note that this chapter specifically lists only those variables that were subject to variation in the current study. In the initial phase of the simulation, the process begins by repeatedly running the G&R simulation alone, in order to save computational time. This continues until significant radial dilatation occurs, triggering the ILT deposition because of elastin degradation. Flow chart diagram of the implemented FSG algorithm is shown in Figure 2.15.

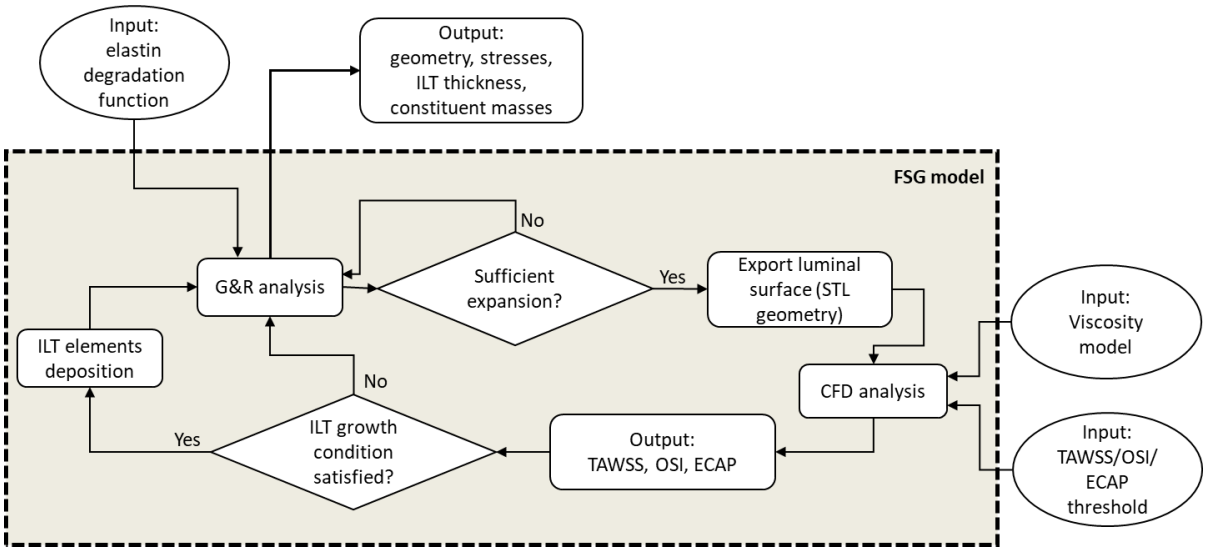

Figure 2.15 *Fluid-solid-growth* model flow chart

Starting with an ideal cylindrical geometry and a normal vessel size, the initially small inner radius of the AAA results in high WSS. High WSS makes it impossible to meet the criteria for ILT deposition, regardless of the criteria used. In this example, TAWSS was used, which is also implemented across all other ILT deposition criterion by definition. TAWSS and inner contour radius for initial phase of simulation can be seen in the Figure 2.16 *a*). TAWSS is lower in the aneurysm sac compared to the healthy part of the aorta, and it has not yet reached the threshold value. If the criterion is not met in a CFD simulation, the G&R algorithm refrains from adding any ILT elements. G&R analysis is ongoing and proceeds in conjunction with CFD analyses to identify the initial stage at which ILT will be deposited.

CFD analysis is conducted to verify one of a ILT deposition criteria. As the AAA radius increases, WSS and TAWSS values decrease until reaching a critical point when they are equal to or lower than the threshold. Figure *b*) shows inner wall radius and TAWSS distribution at the moment when condition for thrombus deposition is finally reached. (e.g., 17 % radial dilatation of the wall for usual TAWSS threshold value 0.4 Pa). In regions where deposition criterion values fall below the specified threshold, new ILT elements are generated in FEAP and added to mesh. If thrombus is already formed, hemodynamics is checked in every third timestep, i.e., every 30 days. Results were very similar when CFD was run every second or every third timestep, but the disparity was more pronounced when CFD run every fourth timestep. Thus, as the optimum between time-conserving and result accuracy, CFD analyses

are executed every three timesteps. The CFD mesh is obtained from G&R geometry node coordinates, transformed into axisymmetric geometry, and used to create a finite volume mesh with 30 wedge elements in the radial direction, irrespective of wall expansion. Smaller elements near the wall ensure more precise results in proximity to the wall, crucial for accurate TAWSS determination from wall shear stress results. The axial coordinates of the finite volume mesh are identical to FEAP nodes and are set automatically. In the next G&R simulation step, ILT elements are added to the area locations where TAWSS was lower than the threshold value, as shown in the Figure *c*). This process repeats in the iterative loop, allowing the inner wall radius to grow, accompanied by the ILT deposition. Figure 2.16 c). shows inner radius contour with first layer of thrombus finite elements and corresponding TAWSS distribution. The G&R analysis of the thrombus-laden aneurysm persistently runs, repeating through a predetermined number of timesteps. This iterative process results in substantial deposition of thrombus volume, as depicted in Figure 2.16 *d*) for advanced AAA stage.

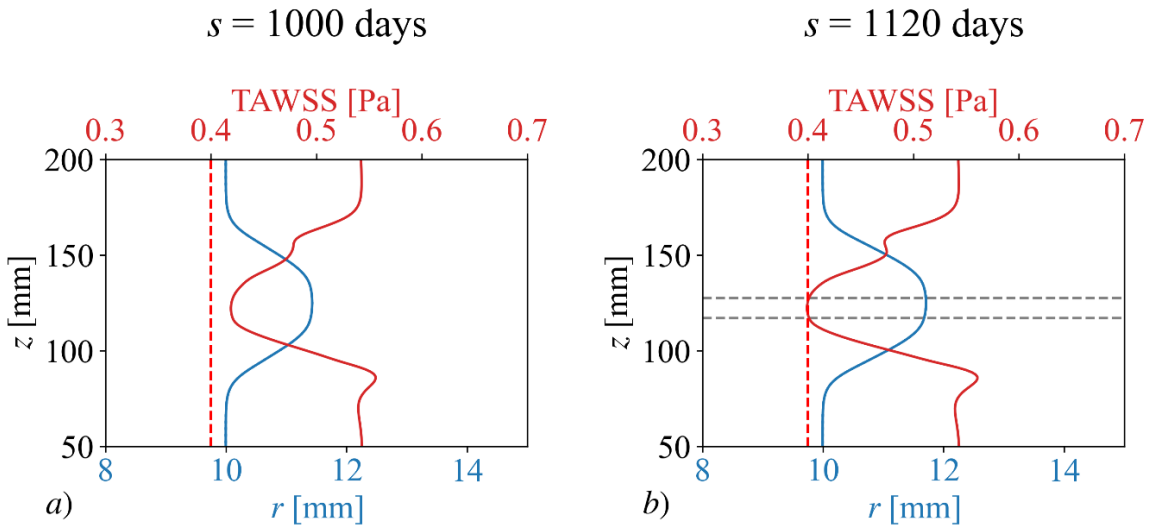

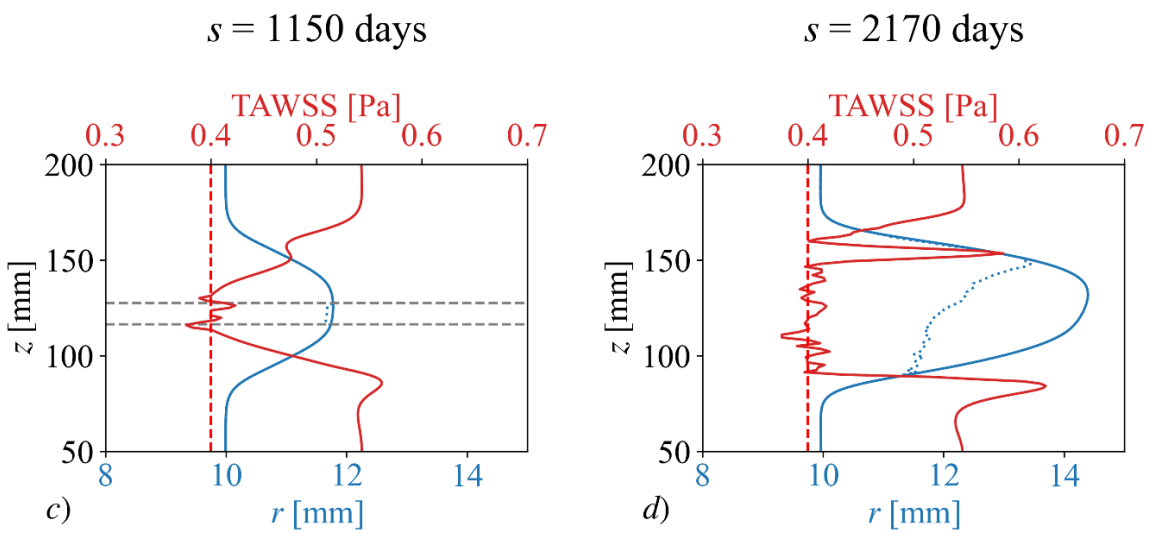

Figure 2.16 Inner wall radius contours (solid blue lines), inner ILT contours (dotted blue lines), axial distribution of TAWSS s(solid red lines), TAWSS threshold value (dashed red lines) for different timesteps: *a*) at time $s = 1100$ days before ILT is formed and TAWSS does not reach threshold value at any location (a), *b*) at time $s = 1120$ days threshold value is first reached; *c*) $s = 1150$ days with first ILT layer deposited; *d*) at time $s = 2170$ days with significant volume of ILT

2.6.3. Model demonstration

To provide a comprehensive understanding, a detailed presentation of one complete FSG simulation example will be showcased, emphasizing differences, advantages, and potential drawbacks in comparison to the traditional G&R model that excludes CFD analysis. Notably, the incorporation of CFD analysis, rather than relying solely on wall dilatation for ILT deposition, is anticipated to introduce variations in ILT shape and size, potentially influencing the disease trajectory.

In this representative example model, blood viscosity was modelled using the Casson viscosity model with laminar characteristics, as detailed in Chapter 4. Standard G&R parameters, including those for elastin degradation, geometry, and collagen mechanics, as outlined in Chapter 3 and presented in Table 2, were utilized. The ILT deposition criteria in this model relied on the TAWSS parameter with an adopted threshold value of TAWSS < 0.4 Pa. While

OSI and ECAP parameters do not actively contribute to this scenario, they will be monitored to provide insights into their behaviour and values.

Table 1 Parameters values for representative FSG model

Variable	**Analyzed values**
ELASTIN DEGRADATION	
a, [-]	300
b, [-]	2
c, [-]	1
d, [-]	2
e, [-]	3.157
$z_{up} - z_{down}$, [mm]	20
COLLAGEN MECHANICS	
G^k, [-]	1.06
σ_h^c, [kPa]	100
K_σ^c	**2**
HEALTHY AORTIC RADIUS	
r_in, [mm]	10

The initial, healthy aortic blood vessel is represented by an axisymmetric, 2-degree geometry with an initial radius is r = 10 mm and height h=250 mm. The finite element mesh for the G&R simulation consists of 726 elements, with 121 in the axial and 6 in the radial direction, excluding any ILT elements. The mesh exhibits finer resolution in the central area where the aneurysm will develop and coarser resolution at the ends. Notably, the number of aortic wall elements remains constant regardless of the shape and AAA size during its growth. Conversely, ILT elements are added based on ILT deposition and growth criteria. The FEAP and OpenFOAM meshes after the first timestep at the beginning of the FSG simulation are illustrated in the Figure 2.17.

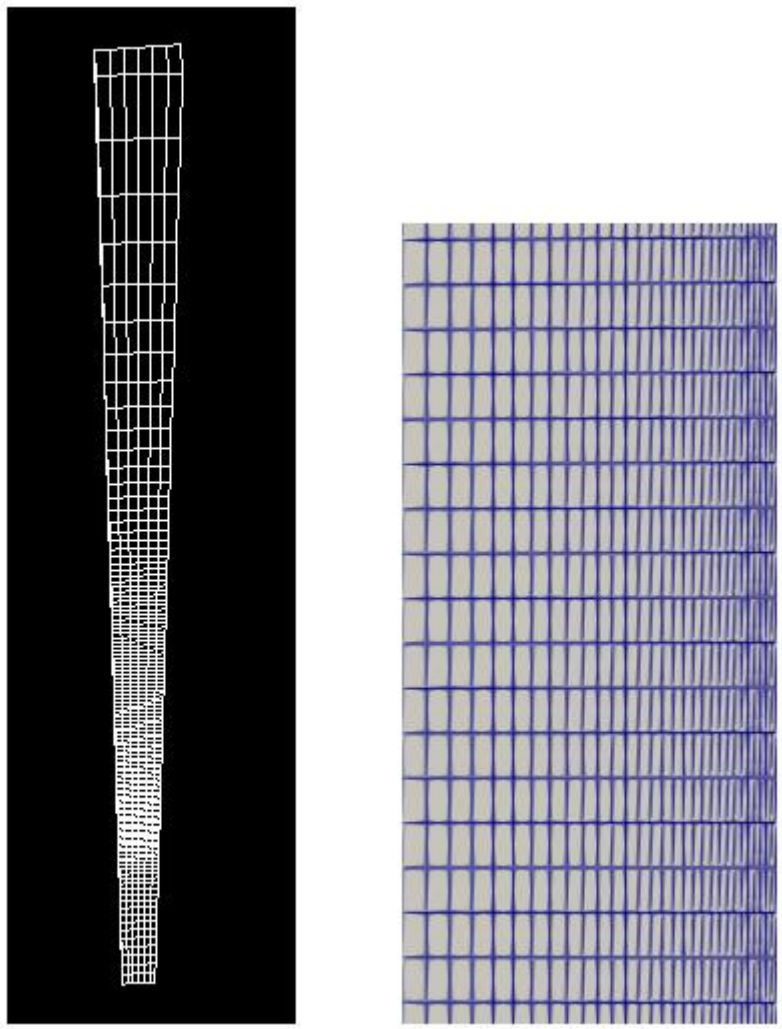

Figure 2.17 *a*) FEAP and *b*) OpenFOAM mesh detail after first analysis for blood vessel with no radial dilatation

At the beginning of the FSG simulation, elastin degradation is on the verge of starting, and the radius begins to expand. The aortic wall has not yet expanded, and the geometry can be considered tubular. TAWSS values are not low enough to meet the ILT deposition criteria because of high wall shear stress values. TAWSS, OSI and ECAP values in this initial step are shown in Figure 2.18.

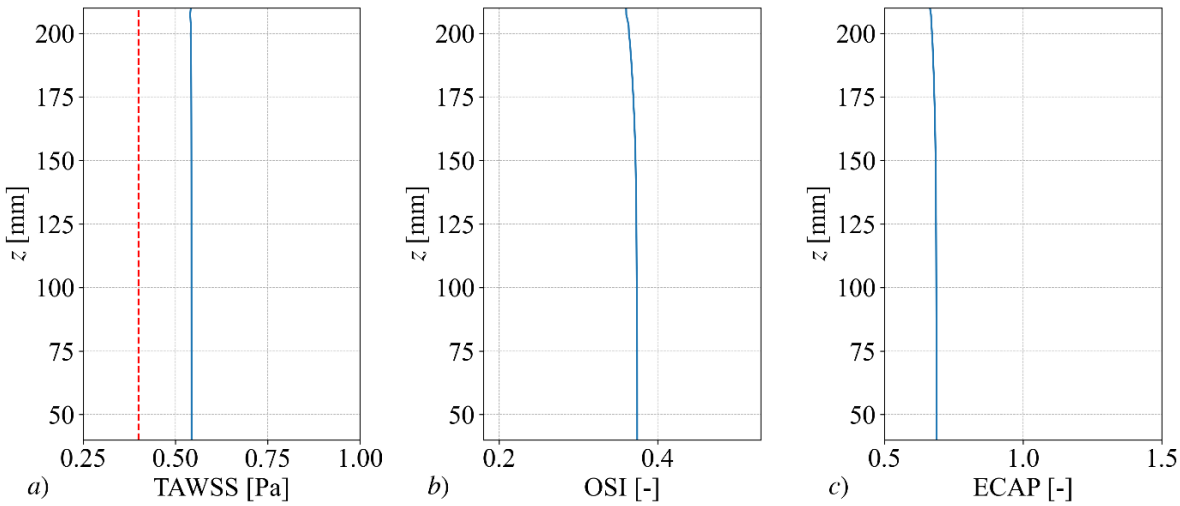

Figure 2.18 *a*) TAWSS, *b*) OSI, *c*) ECAP distribution for the first time step with healthy aortic wall

The TAWSS value of 0.55 Pa across the entire region represents the characteristic value for a healthy blood vessel. Minor irregularities observed in the OSI distribution can be attributed to boundary conditions; however, these irregularities are negligible, particularly given their occurrence at the outset of the blood vessel and far from the aneurysmal area.

The time required for TAWSS values to meet the ILT deposition criteria is contingent upon the G&R geometry parameters and CFD viscosity settings. Under typical values, such as those used in this simulation, ILT deposition typically initiates shortly after 1000 days from the onset of the disease. In this specific simulation, the initial deposition of ILT occurs around 1120th day after the disease's commencement. The maximum inner radius just before the first ILT deposition is approximately 11.7 mm, as depicted in the Figure 2.19.

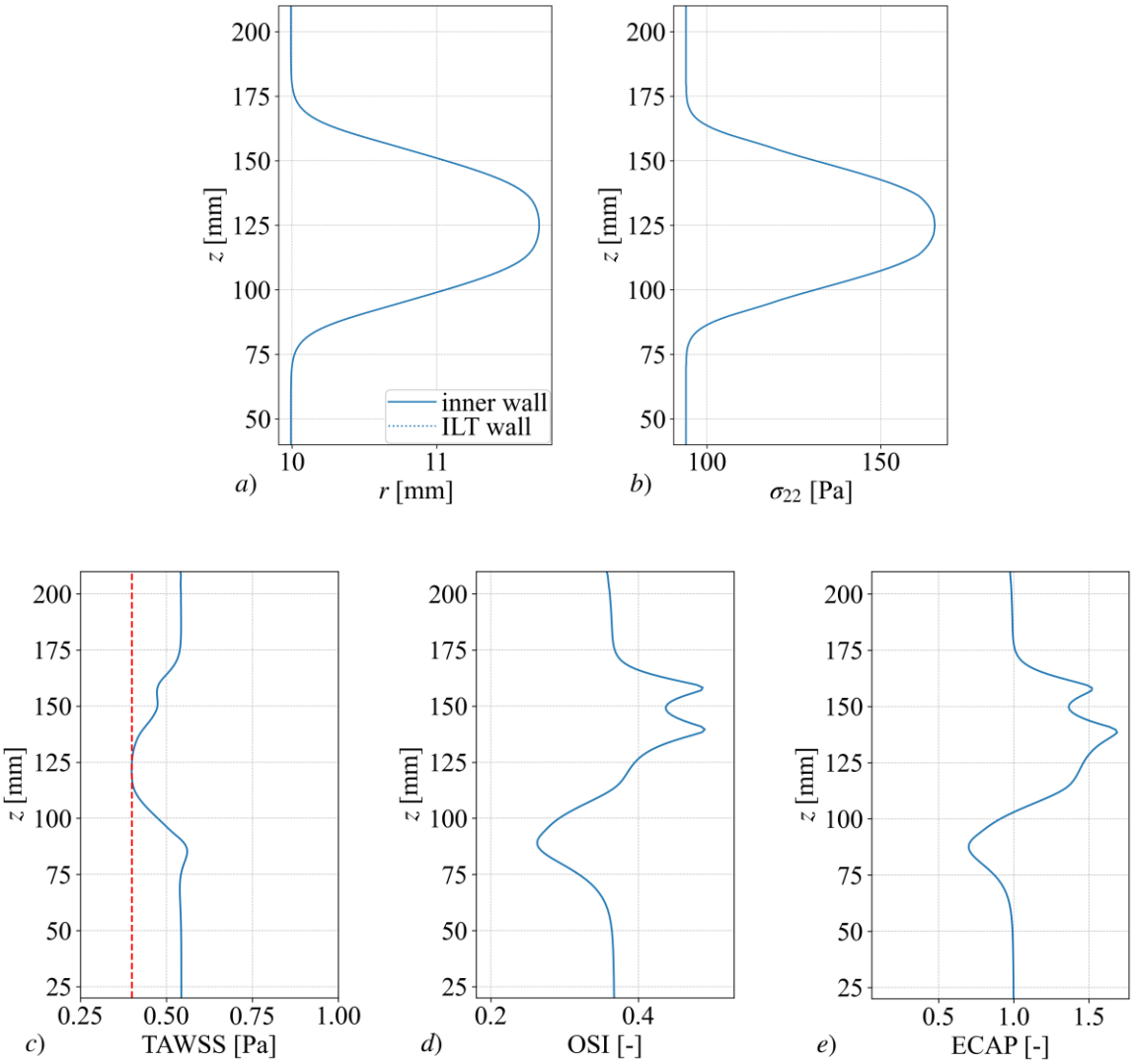

Figure 2.19 *a*) Inner wall radius and inner ILT contours, *b*) stress contour, *c*) Time averaged wall shear stress, *d*) Oscillatory shear index, *e*) Endothelium cell activation potential, plotted over axial AAA length *z* for the inner radius when TAWSS exceeds threshold of 0.4 Pa

As expected, it is clearly visible that the geometry is still vertically symmetrical and maximal radius is in the middle of AAA height. Maximal inner wall radius r_{max} = 11.7 mm and contour is vertically symmetrical because AAA grows freely and there is no ILT that will pull the wall vertically. That coincides with [13]. The same phenomenon applies for stress distribution; it is fully vertically symmetric. TAWSS has the lowest value, a bit below threshold, 0.4 Pa in the central aneurysmal area and that is the place where the ILT formation will start due to critical TAWSS condition. It can be observed that TAWSS diagram is not symmetrical and has greater values in the upper neck region. That could have an impact later on ILT deposition direction.

This suggests an asymmetrical deposition of ILT, with a greater concentration in the lower area. As expected, there is a slight increase in TAWSS values in the healthy part of the vessel near the end of the AAA, just after the aneurysmal area, due to flow separation. The OSI distribution shows high asymmetry, with maximum values of 0.5, indicating fully oscillatory behavior. The upper neck region exhibits values near the maximum, while the lower AAA region shows significantly lower values. Critical areas based on OSI and ECAP parameters are closer to the bottom, with OSI criticality at the end of the aneurysmal area and slightly beyond ECAP. Despite differences in scale, the shapes of the ECAP and OSI diagrams are similar.

In the next stage there will be observed two moments in the growth process. First is when the maximal inner radius is r_{max} = 14mm and second is r_{max} = 16mm. After 2020 days, when the maximal inner radius exceeds 14 mm, clear asymmetry in ILT and AAA shape is visible, also as tendency for aneurysm to harbor the ILT in the lower region, shown in Figure 2.20.

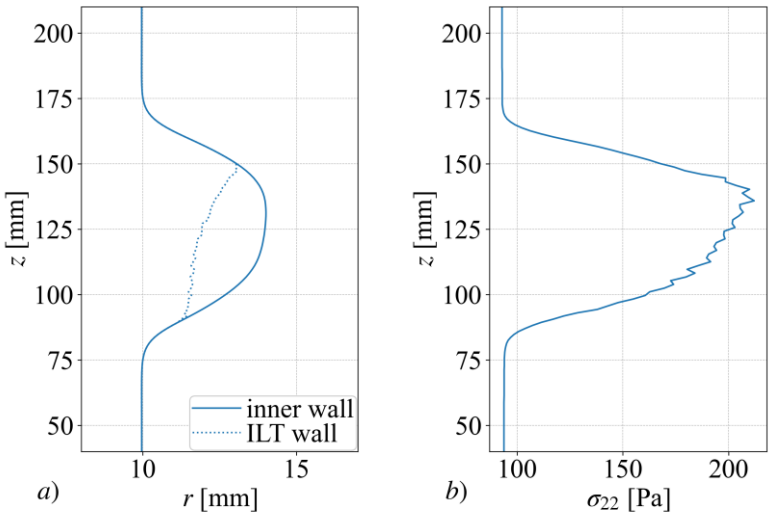

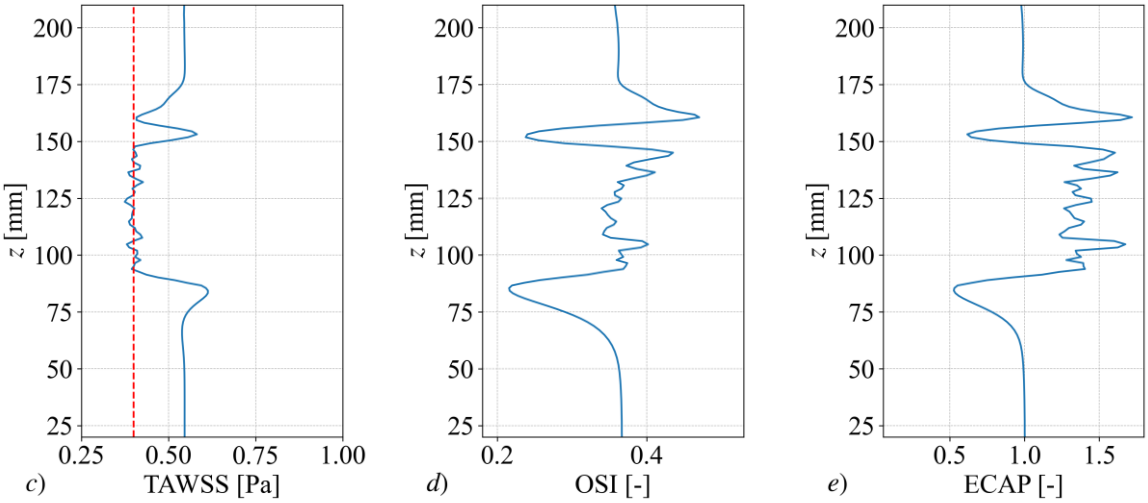

Figure 2.20 *a*) Inner wall radius and inner ILT contours, *b*) stress contour, *c*) Time averaged wall shear stress, *d*) Oscillatory shear index, *e*) Endothelium cell activation potential, plotted over axial AAA length *z* for r_{max}=14mm.

Figure 2.20 clearly illustrates the deposition of ILT on the lower neck side of the aneurysm, with the center of the ILT mass approximately 10 to 15 mm lower than the original center. The deposited ILT causes the stress contour to be vertically asymmetric, with lower values in regions that have thicker ILT. Both ECAP and OSI distributions exhibit similar shapes with more oscillations and irregular patterns compared to those without deposited ILT in the aneurysm. Same quantities are shown in Figure 2.21 for the moment when r_{max} = 16mm.

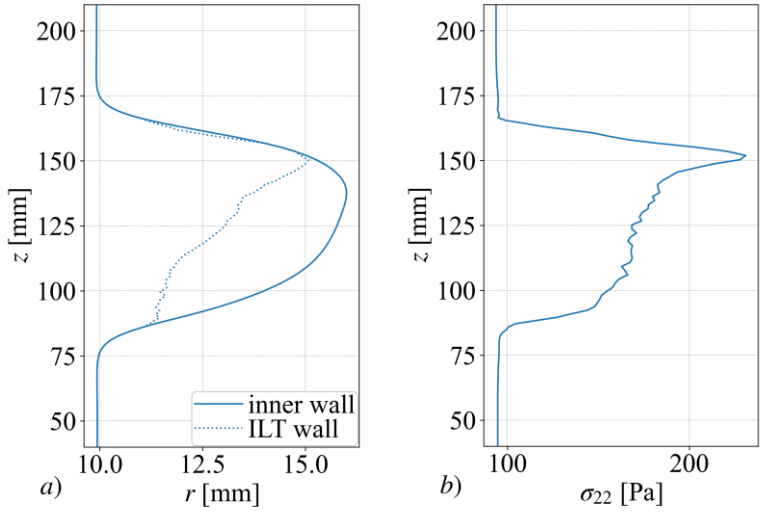

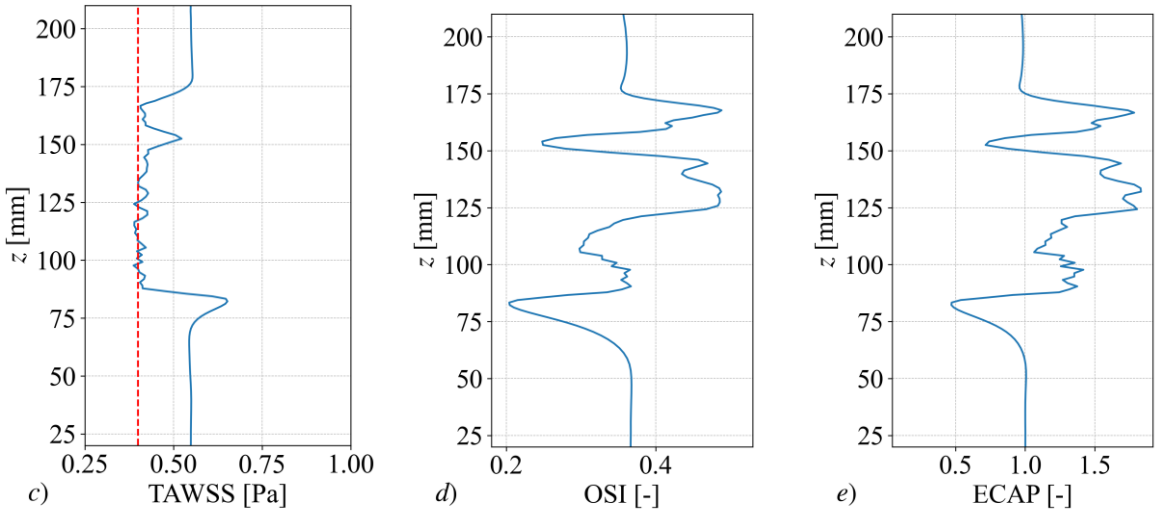

Figure 2.21 *a*) Inner wall radius and inner ILT contours, *b*) stress contour, *c*) Time averaged wall shear stress, *d*) Oscillatory shear index, *e*) Endothelium cell activation potential, plotted over axial AAA length *z* for r_{max}=14mm.

Figure 2.21 shows the inner radius contour exhibits further vertical asymmetry, with the majority of the ILT mass deposited in the lower region. There is a visible thin layer of ILT formed in the upper part of the AAA, disconnected from the original mass. TAWSS distribution is similar, with a less pronounced local maximum in the upper neck part of the AAA. This suggests that the ILT would eventually cover the entire AAA wall and continue to form a single mass. The more pronounced asymmetrical deposition of ILT is reflected in the stress distribution, which is higher in the upper region where ILT is not deposited yet but has almost the same values in the region where ILT has grown thicker. In other words, due to elastin degradation, stress should grow, but it is not increasing at the expected rate because of the thicker ILT, which partially absorbs the stress. OSI and ECAP distributions still look relatively similar to each other and to the previous comparison, but with more changes in value. The lower-middle part has lower values, which was not the case for AAA when r_{max} = 14mm. This phenomenon suggests that the disease progression direction may be different if OSI or ECAP had been used as ILT deposition criteria.

For both time steps when r_{max} =14 and r_{max} =16mm, the ILT surface along its entire height has TAWSS values around the threshold area. This indicates that ILT grows consistently

throughout the analysis time. It can be concluded that the development of ILT will be consistent throughout the entire height.

To get a more detailed impression of the growth process of AAA, several quantities will be displayed on the diagrams as they change over time, such as maximal diameter $D_{\max}$ and inner radius $r_{\max}$, aneurysmal height H, maximal stress $\sigma_{22,\max}$ and ILT volume V_{ILT}. $r_{\max}$ is the maximal diameter of the inner wall at certain time. It is important to notice that location of $r_{\max}$ is changing through the whole growth process because it is closely connected to ILT position, in the opposite relation. As the ILT grows in certain areas, diameter will be smaller because ILT takes over one part of the stress and therefore radial dilatation will be smaller. More about maximal radius height, $H_{D_{\max}}$ location will be explained a bit later in this chapter. Height H and its measurement procedure is described in the Chapter 3. The maximal stress is crucial as it impacts the stability of the AAA, and in instances of overload, it may lead to AAA rupture. In order to monitor the $\sigma_{22,\max}$, whole aneurysmal wall is observed, and the biggest value is taken as a quantity. Therefore, just like the $H_{D_{\max}}$, maximal circumferential stress height $H_{\sigma_{22,\max}}$, depends on the geometry and ILT shape. V_{ILT} is important quantity because according to Shum [5], it is one of the most used parameters for predicting AAA rupture, along within other parameter combinations. Also, ILT shape influences the $H_{D_{\max}}$, and $H_{\sigma_{22,\max}}$. This quantities over time are shown in Figure 2.22.

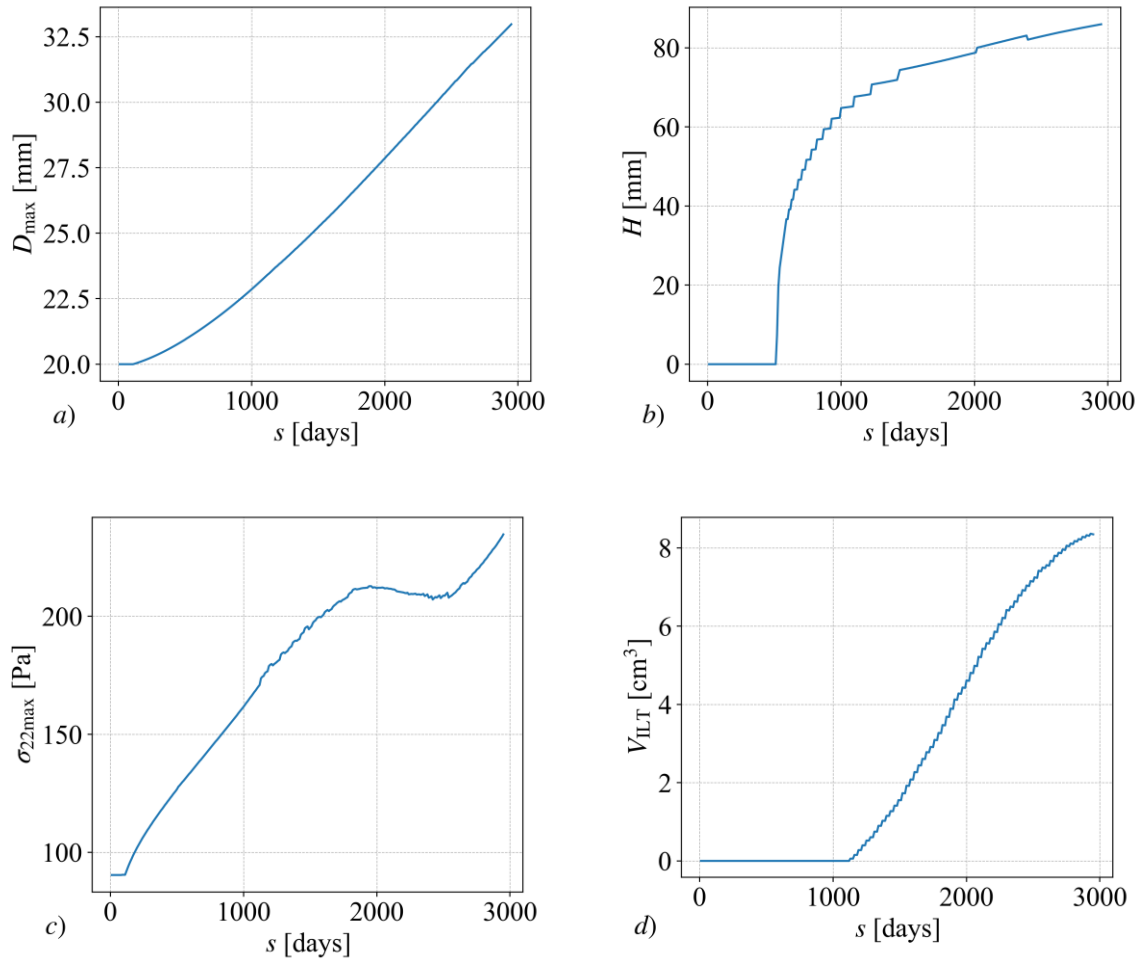

Figure 2.22 *a*) Inner diameter, *b*) AAA height, *c*) maximal circumferential stress and *d*) ILT volume over time

In the Figure 2.22 *a*), it is visible that $r_{max,}$ grows continuously and with a slightly higher rate in the later stage, no matter of ILT deposition. Height *H,* as shown in figure *b*), has a strictly non-linear growth rate and grows with a much higher rate in the first stage. However, it is expected due to the geometry and radial expansion of the aneurysm. Maximal stress $\sigma_{22,max}$, is shown in figure *c*). After first 1015 days, when ILT starts to deposit, growth rate is a bit unstable and has slightly oscillatory characteristics. An interesting appearance happened between 1800-2500 days, when its growth stopped, maximal stress remains constant and even slightly decreases. That phenomenon, known in literature, happens because of geometric features and ILT and AAA shape. This can be attributed to the phenomenon that the point of maximum stress changes and moves along the height. In the figure *d*), V_{ILT} is growing completely linear up to the last 400 days when the growth rate slightly drops. V_{ILT} is directly connected to TAWSS values, and its growth process should follow radial expansion rate which influences TAWSS values in the

first place. Additionally, it can be observed that V_{ILT} growth did not disrupt the smooth expansion of the diameter.

Because of obvious vertical asymmetry, there is additional quantity that would be also good to analyze, and that is the height of the maximal diameter, $H_{D_{\max}}$. If AAA was vertically symmetric all the time, $H_{D_{\max}}$ would be unchanged throughout the entire FSG simulation. In Figure 2.23 $H_{D_{\max}}$ is shown.

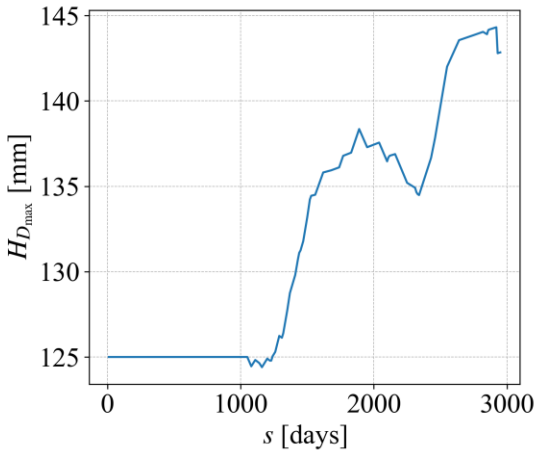

Figure 2.23 Maximal diameter height over time

If compared to the G&R model, which does not have implemented CFD analysis and ILT deposition based on some criteria obtained from OpenFOAM, maximal radius height $H_{D_{\max}}$ would always be in the middle of aneurysmal height through all growth process. Due to the relatively coarse mesh and large finite elements, visible oscillations appear on the diagram. However, in practice, a smooth curved line should be expected. Additionally, there is an area where $H_{D_{\max}}$ drops in duration of 300 days, 2000 days after disease beginning. That phenomenon is attributed to irregular ILT deposition process and growth. $H_{D_{\max}}$ located in the same area where the maximal stress is; therefore, it can be considered a critical point for AAA rupture. Because of ILT deposition in the lower area, critical point moves up towards upper neck region.

Finally, in Figure 2.24 it is shown the stress distribution through the 6 radial layers in the aortic wall.

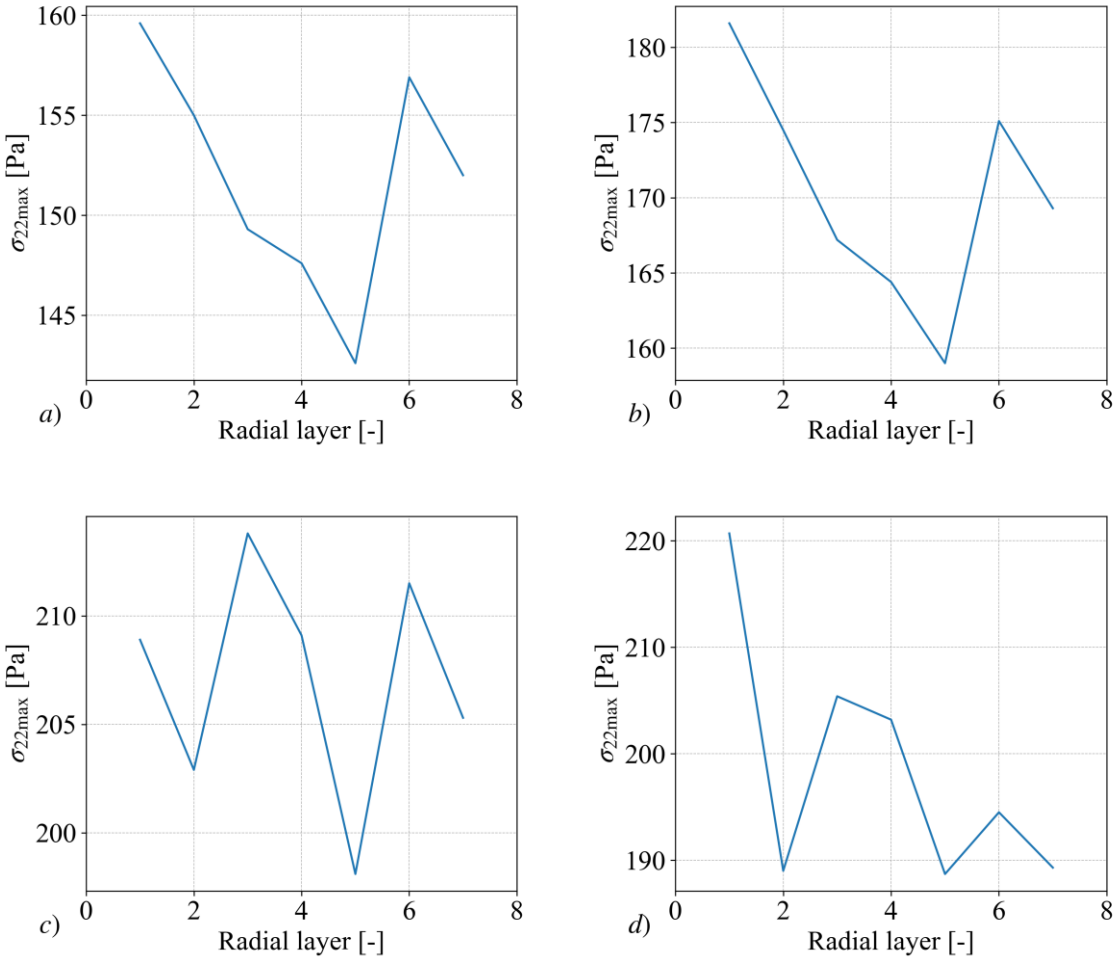

Figure 2.24 Maximal circumferential stress through seven layers, in *a*) 1000th, *b*) 1030th, *c*) 2200th and *d*) 2500th day from the disease start

Due to the evolving material composition over time, the stress distribution is expected to change and increase progressively. It is evident that the maximal stress in the outer layer will experience a significant decrease compared to the inner layer, consistent with the findings reported in the literature. Nevertheless, exact distribution observation should be approached with caution due to potential numerical stability considerations.

In conclusion, the FSG model offers additional insights compared to the G&R model without CFD analysis. The most significant difference lies in the location area of ILT deposition. As a result of distinct wall shear stress distribution in the upper and lower neck regions, TAWSS tends to be lower in the bottom neck area, initiating ILT deposition based on the adopted criterion. With the expansion of the AAA, ILT deposition becomes increasingly asymmetric

until it eventually starts depositing in the upper neck region, influenced by the distorted geometry and blood flow patterns.

Unlike standard G&R models that introduce ILT based on the location of maximal radius dilatation, typically in the central region, the FSG model, supported by the findings of Shum et al. [72], demonstrates that ILT formation initiates in the bottom neck region and gradually expands towards the upper part of the AAA. This underscores the validity and significance of the FSG model in the analysis of AAA.

Given the complexity of the model, a thorough examination of several parameters and settings is necessary to identify the most optimal options. In chapter 4.3, where CFD settings will be explored, it was observed that certain model configurations, through the accumulation of errors, could lead to significant variations and alterations in the progression of the disease. To understand how differences in model definitions affect thrombus deposition and, consequently, the evolution of the disease, we explore various blood viscosity models proposed in the literature, turbulence characteristics, ILT deposition criteria with corresponding threshold values, and initial AAA shape. This investigation aims to demonstrate how seemingly minor differences in individual timestep results can have a substantial impact on the overall shape and presentation of the FSG model. Parameters such as TAWSS threshold value, turbulence, viscosity model, AAA sac shape, and OSI and ECAP as ILT deposition parameters will be examined for their potential impact on the model.

3. INFLUENCE OF GEOMETRY ON AAA RUPTURE

This chapter delves into the analysis of geometric features of AAA and their implications on aneurysmal rupture. Given the relatively unexplored nature of this topic, there is an opportunity to make a scientific contribution by employing applied G&R theory and scrutinizing its data.

Prediction of rupture and optimal timing for AAA surgical intervention remain wanting even after decades of clinical, histological, and numerical research. Although studies estimating rupture from AAA geometrical features from CT imaging showed some promising results, they are still not being used in practice. Patient-specific numerical stress analysis introduced too many assumptions about wall structure for the related rupture potential index (RPI) to be considered reliable. G&R numerical models eliminate some of these assumptions and thus might have the most potential to calculate mural stresses and RPI and increase our understanding of rupture.

To recognize numerical models as trustworthy, it is necessary to validate the computed results with results derived from imaging. Elastin degradation function is one of the main factors that determine idealized aneurysm sac shape. Using a hundred different combinations of variables defining AAA morphology (elastin degradation function parameters, collagen pre-stretch, and initial healthy aortic diameters), we investigated the relationship between AAA morphology, RPI and compared numerical results with clinical findings. Good agreement of numerical results with clinical expectations from the literature gives us confidence in the validity of a numerical model. We show that aneurysm morphology significantly influences the stability of aneurysms.

Additionally, we propose new parameters, geometrical rupture potential index (GRPI) and normalized aneurysm length (NAL), that might predict rupture of aneurysms without thrombus better than currently used criteria (i.e., maximum diameter and growth rate). These parameters can be computed quickly, without the tedious processing of CT images.

3.1. Introduction

AAAs often remain asymptomatic until rupture, an event with a high mortality rate. Rupture prediction and medical interventions continue to be based primarily on the maximum diameter and clinicians' experience, despite various histological, experimental, and computational efforts to find more reliable rupture criteria. For example, from a histological point of view, inflammation and associated extracellular matrix degradation were believed to play a crucial role in AAA progression [73], yet the influence of inflammation on AAA rupture is unexpectedly controversial [74], [75]. The potential to predict rupture of various inflammation biomarkers has been investigated – circulating levels of markers of extracellular matrix degeneration, levels of macrophage migratory inhibition factor, and osteopontin have been reported as potential biomarkers, [76]. Yet, Tavares et al. [74] suggested that inflammation is not a marker for rupture but instead for remodeling. Similarly, Niestrawska et al. [75] noted that collagen deposition only occurs in conjunction with infiltration of inflammatory cells. They theorized that inflammation in the wall is necessary for synthetization of fiber. That would explain why anti-inflammatory drugs were reported to be surprisingly counterproductive – a rapid AAA development and rupture in a patient on immunosuppressive drugs was reported in [77]. Note that these histological studies are essential for understanding biochemical processes occurring during AAA progression; however, unfortunately, in order to measure the levels of proposed biomarkers, it is necessary to harvest aneurysmal tissue. Thus, even if they were confirmed as markers for rupture, they could not be used to determine the need for surgical intervention.

Further, more applicable attempts to predict rupture have been made by analysis of CT scans. Again, controversies arose with conflicting results: several studies found that AAA rupture is associated with larger intraluminal thrombus (ILT) volumes [78], [79]; however, another study found no difference in ILT volumes in ruptured and intact AAA [80]. Similarly, some studies claim that thicker thrombi lead to localized hypoxia, and consequentially, increased neovascularization and inflammation, as well as regional wall weakening [81], but others found that thicker thrombus slowed down the AAA growth and vice versa, the smaller relative size of ILT was linked to higher growth rate [82]. It has also been hypothesized that aneurysm morphology is more predictive of rupture risk. Shum et al. [5] defined twenty-five size and shape indices in total and estimated their importance for aneurysm rupture. The same group concluded that AAA volume and surface area were significantly different in ruptured and

unruptured aneurysms [83], yet Kitagawa et al. [84] stated that the diameter measurement of an aneurysm is superior to volume measurement for prognosis and operative planning. In addition, Shum [72] concluded that maximum aneurysm diameter and sac volume, along with other meaningful geometrical parameters, are in direct and close relationship with peak wall stress.

From the mechanical point of view, rupture occurs simply when wall stresses exceed wall strength. This simple criterion led to early "snapshot" patient-specific finite-element stress analyses. Despite introducing many assumptions (e.g., homogeneous structure, no pre-stretches, oftentimes spatially uniform wall thickness), one such study, [85], showed that AAA geometry, rather than size and loading, plays a crucial role in rupture. They showed that stresses could be higher in smaller normotensive AAA compared to large hypertensive ones. However, it is essential to keep in mind that both stress and strength distributions are extremely heterogeneous and depend on various factors [86]–[89].

The computational method that shows the most promise for computing wall stresses and rupture potential index more precisely and increasing our understanding of AAA progression and rupture is the general framework for growth and remodeling (G&R) of soft biological tissues. G&R models eliminate most assumptions used in "snapshot" analyses, at the cost of true, patient-specific AAA geometry.

Vascular adaptations, diseases, and interventions have been studied using constrained mixture G&R model for the last twenty years [90]. Several studies helped to understand the role of the different model parameters, e.g. [91]. Using the G&R model implemented in membrane finite element, the importance of initial structure and aortic properties on the growth of idealized fusiform AAA has been studied [92]. Additionally, postulating that functional elastin and smooth muscle are mostly lost in aneurysms, collagen remains the principal remaining load-bearing constituent of the aneurysmal wall.

In order to simulate realistic aneurysm geometries, we have implemented the G&R model of the wall in 3D finite elements using the finite element analysis program *FEAP* [93]. The implementation was verified on an adaptation of a non-cylindrical artery to increase in blood pressure and blood flow, [11]. The implementation showed promising potential for computing realistic evolution of geometry, stress, and thickness during the growth of fusiform and non-

symmetric fusiform aneurysms. We also presented slight buckling of the non-symmetric fusiform aneurysm due to non-axisymmetric elastin degradation, characteristic for true abdominal aortic aneurysms [11].

In this contribution, we apply the existing model to computationally study the correlation of aneurysm morphology on rupture potential index (RPI) and compare our results with results derived from CT imaging from [5]. We also propose new, easily computed parameters that will predict the likelihood of AAA rupture without thrombus better than the currently used maximum diameter.

3.2. Methods

Although the G&R theory was explained in Chapter 2.6 here will be mentioned only the important things needed for understanding the matter. Briefly, G&R models are founded on the idea that soft tissues are subject to a continuous constituent mass turnover, with collagen and smooth muscle being degraded and new tissue being continuously deposited. Mathematically, current mass is calculated as

$$M^k(s) = M^k(0)\,Q^k(s) + \int_0^s \dot{m}^k(\tau)\,q^k(s-\tau)\,\mathrm{d}\tau \tag{32}$$

where $M^k(s)$ and $M^k(0)$ are total (integration point-wise) masses of constituent k at the current time s and initial time 0, respectively. Mass production rate is denoted by $\dot{m}^k(\tau)$ and $q^k(s-\tau)$ is the survival function defining the percentage of constituent mass produced in a time τ that survived till the current G&R time *s*. Survival function for mass existing in the initial G&R time ($\tau = 0$), $q^k(s-0)$, is labeled as $Q^k(s)$.

Unlike collagen and smooth muscle, elastin is produced only in prenatal age, meaning production rate $\dot{m}^{\mathrm{e}}(\tau) = 0$. That simplifies eq. (32) to

$$M^{\mathrm{e}}(s) = M^{\mathrm{e}}(0)Q^{\mathrm{e}}(s) \tag{33}$$

Elastin degradation function Q^e in healthy arteries slowly and mainly homogeneously decreases with time with a long half-life $\tau_{1/2}^e$ of approximately 40 years, [94]. Aneurysms are characterized by a local loss of elastin and thus Q^e changes also with spatial coordinates. The elastin degradation function used here is adapted from [56], similar to other studies that focused on aneurysm growth [55], [95], [96]. For non-symmetric fusiform aneurysm, elastin degradation function can be defined as

$$Q^{\mathrm{e}}(s,z,\vartheta)=\phi_{\mathrm{rem}}^{\mathrm{e}}+\left(1-\phi_{\mathrm{rem}}^{\mathrm{e}}\right)f_1(s)\,f_2(z)\,f_3(\vartheta) \tag{34}$$

In this equation $\phi_{\mathrm{rem}}^{\mathrm{e}}=0.2$ is the fraction of elastin not being degraded, as it was shown in [97] that even in large aneurysms, some functional elastin remained. Functions $f_1(s)$, $f_2(z)$ and $f_3(\vartheta)$ define degradation over time, axial and circumferential direction, respectively. First-order temporal decay of elastin is assumed, such that

$$f_1(s)=\left(1-\left(1-\exp\left(-s/\tau_{1/2}^{\mathrm{e}}\right)\right)\right). \tag{35}$$

Because aneurysm growth is computationally initiated by loss of elastin, the half-life of elastin in the aneurysmal sac was reduced to the value $\tau_{1/2}^e=2$ years. Similar to previous studies [55], [56], [95], [96], degradation in the axial direction *Z* was chosen to be:

$$f_2(z)=\begin{cases}\exp\left[-\dfrac{-0.7}{\min(300,a)}\left(z-z_{\mathrm{down}}\right)^b\right] & z<z_{\mathrm{down}},\\ \exp\left[-\dfrac{0.7}{\min(300,a)}\left(z-z_{\mathrm{up}}\right)^b\right] & z>z_{\mathrm{up}},\\ 1 & z_{\mathrm{down}}\le z\le z_{\mathrm{up}}.\end{cases} \tag{36}$$

Variables *a* and *b* define width and steepness of elastin degradation in the axial direction. That can be seen in Figure 3.1 *c*), showing that for the constant value of the parameter b, an increase in parameter *a* prolongs the range where elastin is degraded; and *e*), demonstrating the influence of parameter b for constant *a*. In between coordinates z_{down} and z_{up} from the equation (**36**),

elastin degradation is maximal and constant in the axial direction, while when z approaches 0 or L, $f_2(z)$ gradually goes to zero, leaving elastin intact in the healthy part.

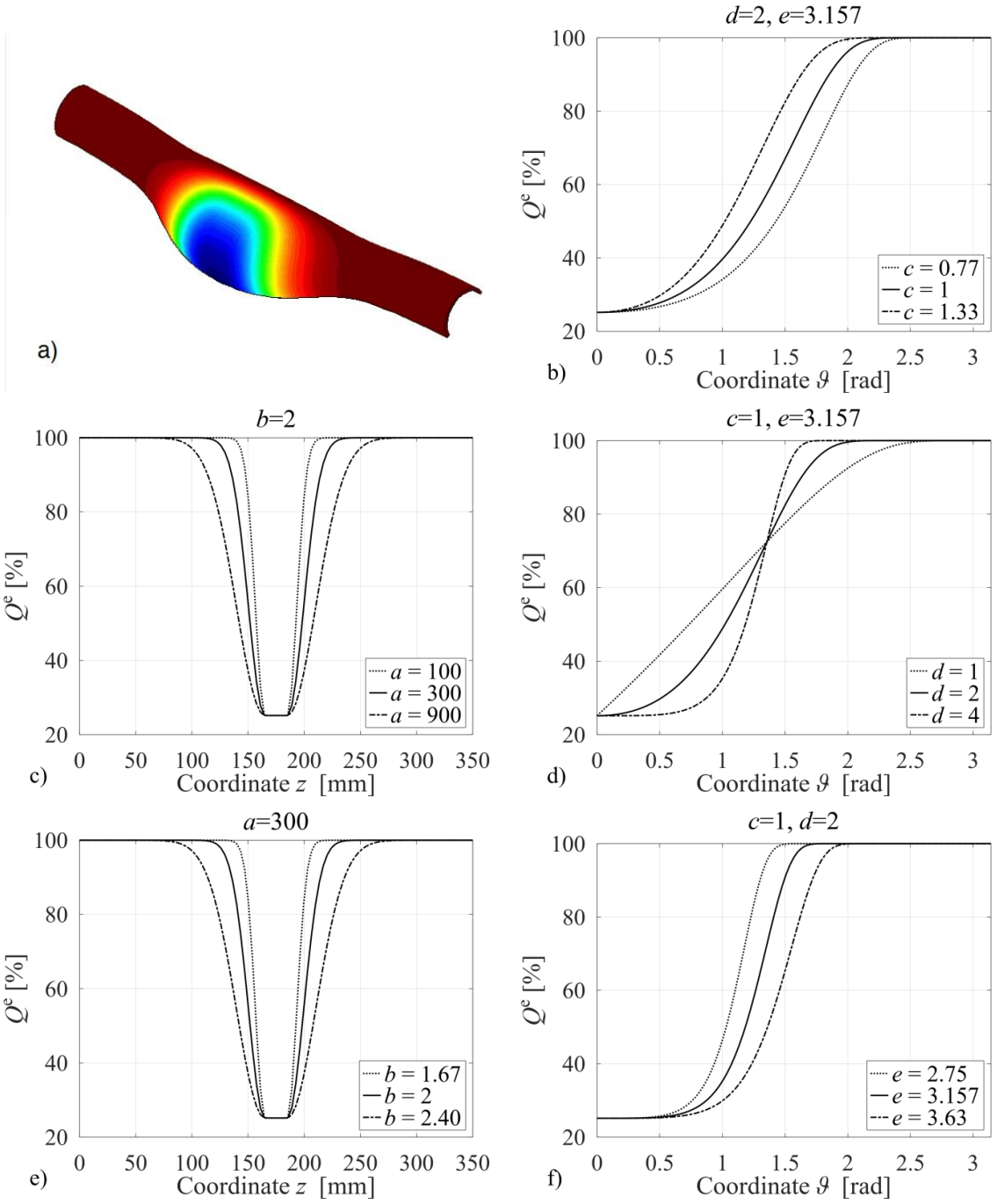

Figure 3.1 Spatial distribution of remaining elastin fraction *a*). Influence of different parameters a, b, c, d, e combinations from equations (5) and (6) at instant s=2000 days: axial distribution of remaining elastin at $\vartheta = 0°$ depending on parameters a *c*), and b *e*); circumferential elastin distribution at the aneurysm apex ($z = 175$ mm) depending on values of parameters c (b), d (d), and e while the other two are kept constant *f*).

Additionally, to model non-symmetric fusiform aneurysm, degradation of elastin in the circumferential direction ϑ is needed, and chosen to be:

$$f_3(\vartheta) = \exp\left[-\left(\frac{c\vartheta}{e-\vartheta}\right)^d\right] \tag{37}$$

where *c, d* and *e,* are function parameters determining width and steepness of elastin degradation in the circumferential direction. As can be seen from Figure 3.1 *b*) and (f), with lower values of *c* and higher values of e the area is widening. Note that for a special case $c = 0$ aneurysm becomes axially symmetric. On the other hand, parameter *d* changes the steepness of the elastin degradation function, Figure 3.1 *e*).

Figure 3.1 *a*) shows the spatial distribution of the remaining mass of elastin Q^e at instant $s = 2000$ days for chosen parameters *a, b, c, d,* and *e*. The dark red color in the Figure 3.1 *a*) denotes intact elastin. In response to a local irreversible loss of elastin, a local dilatation forms, and the shape of the AAA sac is strongly influenced by elastin degradation function.

The aneurysm growth is modeled starting from an initially healthy aorta. That enables us to solve the inverse problem, satisfy equilibrium in homeostasis, and avoid making assumptions about the initial mass fractions, orientations, and mechanical properties of a diseased aorta. The healthy aorta is represented by a 180° cylindrical segment comprising 50 non-uniform elements in the axial direction, 16 in the circumferential direction, and 3 in the radial direction. Hexahedral 8-node elements were used with three degrees of freedom at each node. In order to minimize the influence of boundary conditions, i.e., proximal-distal symmetry, the length of the segment was set to 350 mm. Enlargement of aneurysms is initiated by the irreversible loss of elastin, simplified to a spatiotemporal function.

Intending to find a more reliable geometry-based rupture predictor than the currently used maximum diameter, we investigated parameters that influence the AAA sac morphology the most. Despite many parametric studies that tried depicting importance (e.g. [56], [92]) and possible range (e.g. [98]) of each model parameter, or significance of the growth description ([55]), none of the previous studies investigated the influence of elastin degradation function parameters on the AAA progression and rupture. Because the parameters significantly influence

aneurysm sac geometry, we changed parameters in the elastin degradation function (equations (5) and (6)). The elastin degradation likely depends on increased inflammation and elevated oxidative stress due to smoking [99], [100], Marfan syndrome, and other patient anamnesis data. The analyzed variables and the corresponding tested values are shown in Table 2. Parameter values for elastin degradation function were chosen based on Figure 3.1, in such a way that they generate sufficient change to AAA morphology.

Additionally, as discussed above, collagen fiber deposition pre-stretch defines stiffness of collagen and thus, indirectly also deformation of AAA. Because stiffness of collagen is calculated to satisfy equilibrium, we varied two main collagen-related parameters – prestretch and homeostatic stress in collagen fibers. Reference for values of collagen pre-stretches was taken from the literature, e.g. [56] used a similar range. On the other hand, homeostatic collagen stress should not be lower than homeostatic stress in an artery (defined as 100 kPa) but values much higher than 200 kPa would lead to unphysical negative stiffness of elastin. Additionally, noting that healthy aortic diameter varies among patients in the range 14-24mm (e.g., see Fig. 1 and Table 1 in [101] or Table 2 in [102]), we analyzed the influence of healthy aortic diameter as well. Thus, analyzed values of healthy diameter were chosen from the range reported in the literature.

The stress-mediated gain parameter $K\_\sigma\text{^}c$ defines collagen production and does not affect AAA morphology much. However, it was determined to be by far the most influential parameter in the variability of model output [103], as it changes AAA growth rate, and consequently stresses and RPI. This means that for the same geometry (i.e., geometrical indices), RPI will vary significantly. Changes in this parameter must, therefore, be included in this study. Parameter range was chosen based on parameter sensitivity studies ([56], [103]). Note that all three models are slightly different, but the values can be roughly calculated to correspond to each other.

All other model parameters were the same as listed in Table 2. A total of 114 different parameter combinations were simulated.

Table 2 G&R parameters used for simulations

Variable	**Analyzed values**

ELASTIN DEGRADATION	
a, [-]	100, 300, 900
b, [-]	1.67, 2, 2,40
c, [-]	0.77, 1, 1.3
d, [-]	1, 2, 4
e, [-]	2.75, 3.157, 3.63
$z_{up} - z_{down}$, [mm]	10, 20, 30, 40
COLLAGEN MECHANICS	
G^k, [-]	1.048, 1.06, 1.08
σ_h^c, [kPa]	100, 200
K_σ^c	1, 2, 3
HEALTHY AORTIC DIAMETER	
d_in, [mm]	16, 20, 24

Note that all these changes could represent real differences in patients: e.g., stiffer collagen might correspond to male sex [104], healthy aortic diameter changes with age [101], height/body mass index. Obviously, the model contains many more input parameters that could have been chosen to investigate**.** Yet, we focused on parameters that have the most influence on AAA geometry and one that was shown in multiple previous studies to have the highest influence on AAA outcome. Furthermore, production rate parameters were numerically investigated quite thoroughly, unlike initial aortic diameter or elastin degradation function parameters that were always kept constant.

3.3. Morphological analysis

Martufi et al. [105] defined twenty-five size and shape indices, out of which nine were 1D size indices, six 2D shape indices derived from the 1D size measurements, four 3D size indices, two 3D shape indices, and four second-order curvature-based indices. Shum et al. [5] calculated these indices on 76 human AAAs applying semi-automatic vessel wall detection and quantification from computed tomography images [106] and automatic generation of surface topologies for AAA models [83]. The study population contained ten ruptured and 66 randomly selected unruptured aneurysms. Among these 25 indices, AAA length (*L*), height (*H*),

maximum diameter (*D*), tortuosity (*T*) surface area (*S*), and volume (*V*), the ratio of ILT to AAA volume, and asymmetry factor were deemed the most important.

Note that some of the geometrical features from [105] are related to the thrombus and neglected in this study. The definition of 1D indices on computational AAA can be seen in Figure 3.2. Maximal diameter is measured at the aneurysm apex. Aneurysm height is calculated as the shortest distance between the centers of starting and ending diameter. Starting and ending diameters are defined as 5% diameter dilatation. Aneurysm length follows the centerline, starting and ending from the same diameters, as shown in Figure 3.2.

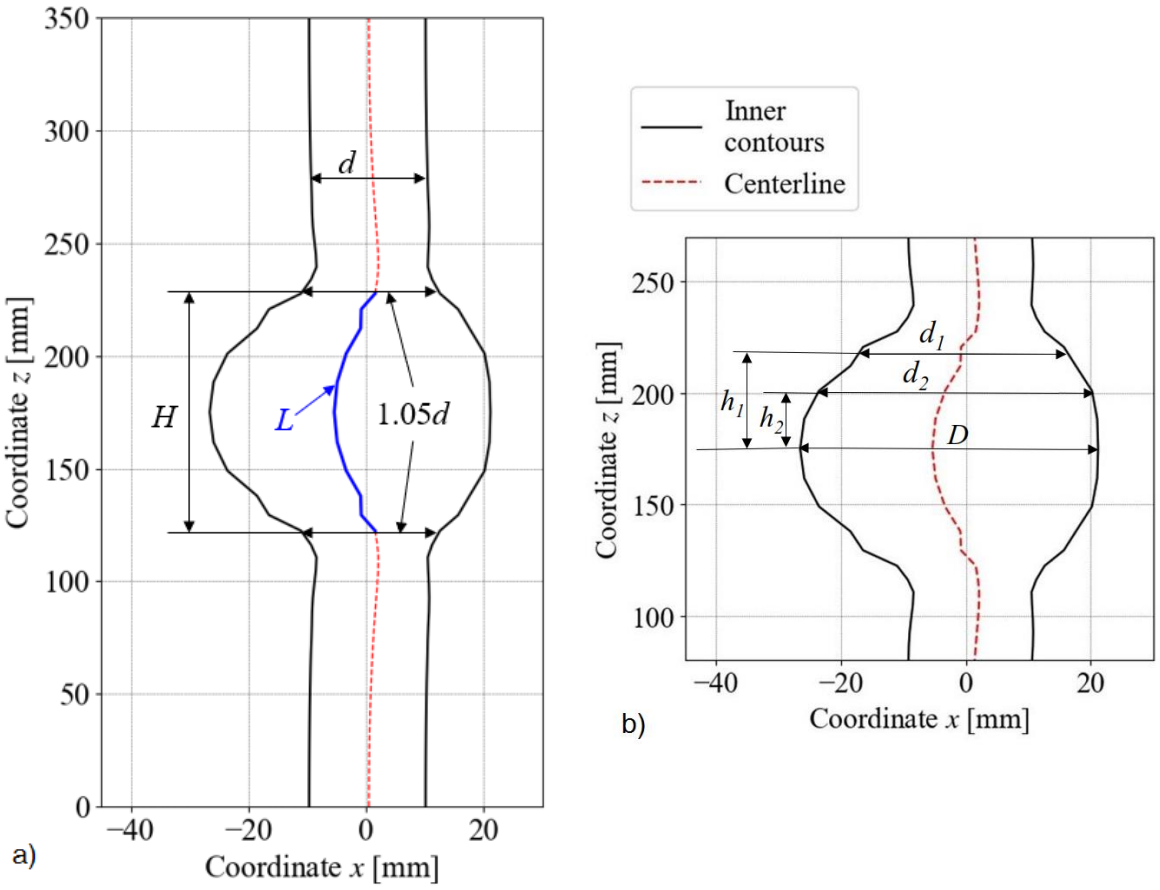

Figure 3.2 Inner contours (full black line) and centerline (dashed red line) of a nonsymmetric fusiform aneurysm and definition of 1D geometrical features: healthy inner diameter *d*, the height of aneurysm sac *H* (defined from locations where diameters are 5% wider compared to a healthy one), length of aneurysmal sac *L* (blue line following the centerline between the same boundaries as H) (a); maximal diameter *D*, the definition of proximal neck diameters d_1 and d_2 at different heights h_1 and h_2 measured from the aneurysm apex at $z = 175$ mm.

Proximal neck diameter is measured from CT images as aortic diameter just below renal arteries. On computationally obtained aneurysm, it is unknown where the renal arteries and the neck are. Thus, we used two different definitions of the neck diameter: the first definition is taken from [105], where both proximal and distal neck diameters of idealized fusiform aneurysm were delineated as healthy diameter. Noting that the aneurysm height of idealized aneurysm is greater compared to the height of both aneurysm sac [105] and abdominal aortic segment [102] measured from CT imaging, we defined neck diameter at a distance h from the apex . Neck diameters d at three different heights were investigated (h_1=62mm, h_2=55mm, and h_3=48mm).

2D size indices are calculated using 1D indices: tortuosity T is the ratio of the length and height of aneurysmal sac, while diameter-diameter ratio Ddr is calculated as maximal to neck ratio, as in [5]. Three-dimensional size indices of interest are the surface and volume of the aneurysm sac. They are determined using coordinates of finite element nodes.

3.4. Numerical follow-up procedure

In order to find the most reliable predictor of rupture based on AAA morphology, we have run 114 G&R analyses with different combinations of input parameters defined in Table 2.As shown in the flow chart in Figure 3.3, for each analysis, the instance when dilatation of the aorta exceeded 50% of the healthy diameter represents the starting time step in observation. At that time, 1D size indices are measured, and 2D and 3D are calculated. Additionally, rupture potential index (RPI), a ratio of wall stress and strength is calculated. Wall strength S has been shown to be heterogeneous and dynamic. It is typically calculated (in MPa) as

$$S = 0.719 - 0.379 \cdot (ILT^{1/2} - 0.81) - \\ - 0.156 \cdot (NORD - 2.46) - 0.213 \cdot HIST + 0.193 \cdot SEX, \tag{38}$$

where ILT is thickness of thrombus is cm, $NORD$ is normalized local diameter, $HIST$ is the family history (½ with history, -½ without history) and SEX is patient's gender (½ male, - ½ female), [89]. Because we focused on AAA without thrombus, for all aneurysms we take ILT = 0. Additionally, as idealized AAAs have no history or sex, we took the most conservative

case – female sex (*SEX* = - ½) and family history (*HIST* = ½). Note that the strength is still spatio-temporal function because of changes in diameter.

G&R time of aneurysm formation is defined as s_f, and the analysis continuous. Geometrical features and RPI are examined every 6 months (i.e., every 18 timesteps of ten days), and the instance of the latest follow-up s_f is updated each time.

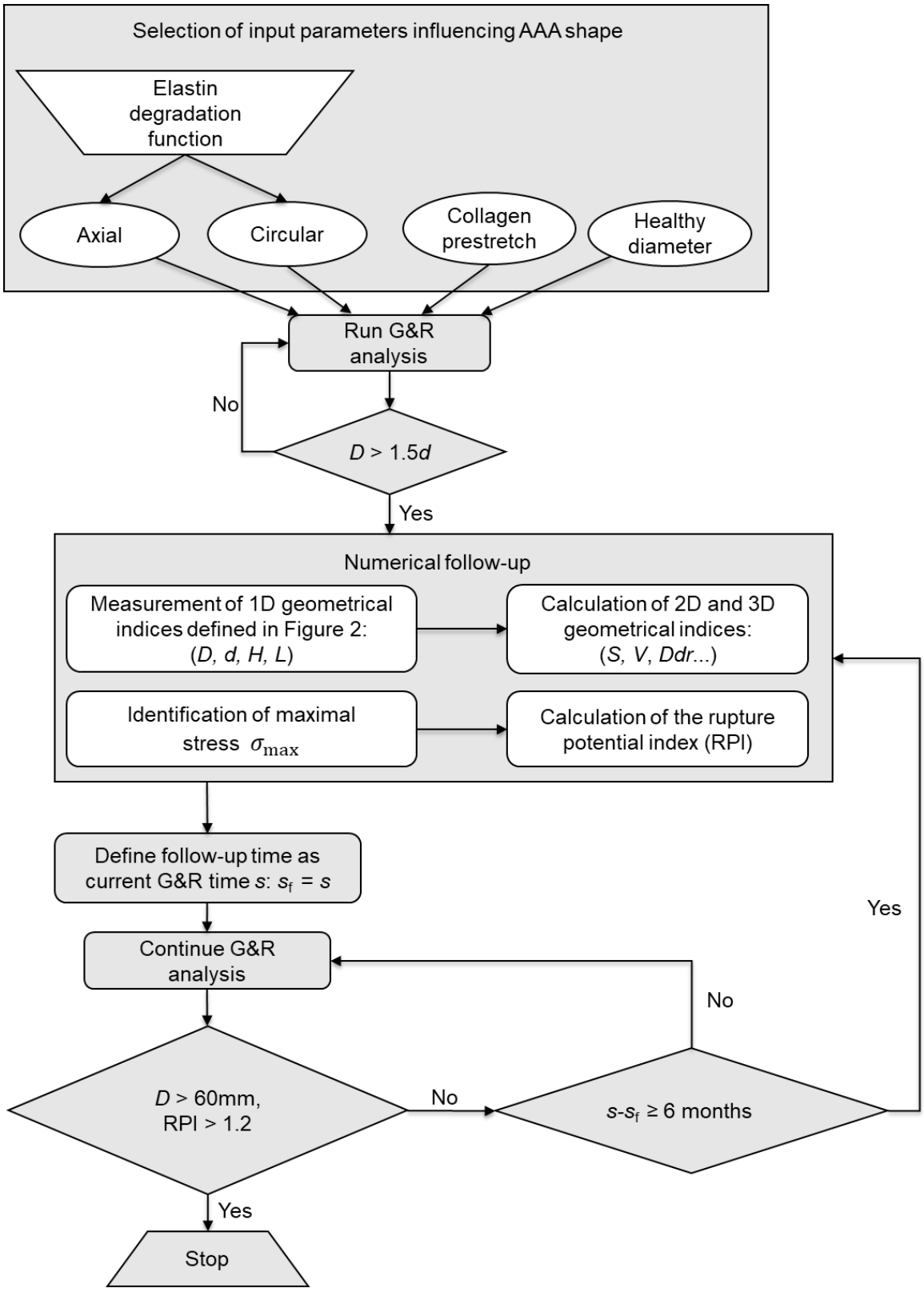

Figure 3.3 Flow chart of the procedure for a numerical follow-up. Notation: s_f denotes G&R time of the latest numerical follow-up, s is current G&R time, D denotes maximum diameter, GR is a growth rate

If the maximal diameter during a follow-up exceeds 60 mm we assume thrombus would be deposited [20] or the RPI exceeds 1.2, we consider the aneurysm ruptured and terminate the simulation. The value of 1.2 was chosen because the chosen conservative HIST and SEX values might slightly overestimate RPI. We have run a statistical analysis with a cut-off at RPI = 1, and statistics changed minimally.

3.5. Statistical analysis

The correlation of each geometrical index with the RPI was studied statistically using a linear regression model to calculate Pearson's correlation coefficient *r*. Pearson's correlation coefficient is a measure of strength and direction of linear statistical correlation of two variables. For *r*-value close to ±1, there is a strong linear correlation between the RPI and a certain parameter. Wald test with t-distribution of data was performed to examine the significance of a linear correlation between the RPI and each index.

Statistical analysis was run for previously defined 1D, 2D, and 3D indices, but was also used to define a new, potentially more reliable parameter. The definition of the new composite morphological parameter CMP was based solely on 1D indices easily estimated from imaging scans (i.e., maximum diameter *D*, healthy/proximal neck diameter *d*, and centerline length *L*)

as $\mathrm{CPM} = L^i D^j d^k \left(N D^m - d^m \right)^n$. The advantage of 1D features compared to volume or surface is a simple measurement without tedious CT image processing. CMP was designed both using clinical observations and the initial trial and error method. We allowed $i, j, k, m, n = -3, -2..3$

and $N = 1, 2, 4$. Statistical values were computed for each combination of *i*, *j*, *k*, *N*, *m*, and *n* for all four definitions of diameter *d*. The form of CMP that predicts rupture the best was chosen as a combination that resulted in the highest absolute *r*-value averaged over all definitions of proximal neck diameter.

3.6. Results

A total of 114 analyses and 876 numerical follow-ups were conducted. For each follow-up, the relationship between the estimated RPI and size index can be shown as in Figures 4-7. Additionally, we calculated the correlation factor *r* for all parameters to determine which parameter predicts the RPI the best, as shown in Table 3. The mean value of each parameter with its corresponding standard deviation is added to the table and compared to results from CT imaging. Note that data from [5] includes 46 out of 76 randomly chosen aneurysms larger than 55mm. Such large aneurysms are not even considered numerically. Because of that, indices such as maximum diameter, surface area, and volume that depend on the choice of observed aneurysm are much larger in the literature. Nevertheless, data in the literature for those indices also vary greatly, as can be seen for surface area and AAA volume reported by the same group in [5] and [83] in Table 3.

Noting that the RPI of some observed geometrical indices is clearly grouped depending on the healthy diameter, every point is colored based on the initial diameter. These indices are not good predictors of rupture themselves, yet their potential to predict rupture increases significantly when normalized by healthy diameter.

As can be expected, one of the geometrical indices grouped by initial diameter is the maximum diameter shown in Figure 3.4 *a*). If only the healthy diameter of 20 mm were considered (black dots), as is usually the case in computational parametric studies, the maximum diameter would have an *r*-value very close to 1. However, with the change of initial healthy aortic diameter in a physically reasonable range, the *r*-value decreased to 0.665 (see Table 2). Unlike the maximum diameter, the aneurysm length does not seem to depend on the initial diameter, Figure 3.4 *b*). Although almost exponential relation can be seen, the dissipation of data is too high for aneurysmal length alone to be considered a reliable predictor of rupture. However, noting other parameters either have linear or very weak connection to rupture, it is not surprising that the length of the AAA sac was determined as the feature with most information gain by machine learning performed in [5]. Note from Table 2 that numerically obtained and measured AAA lengths are similar with the mean values of 113 vs. 106 mm.

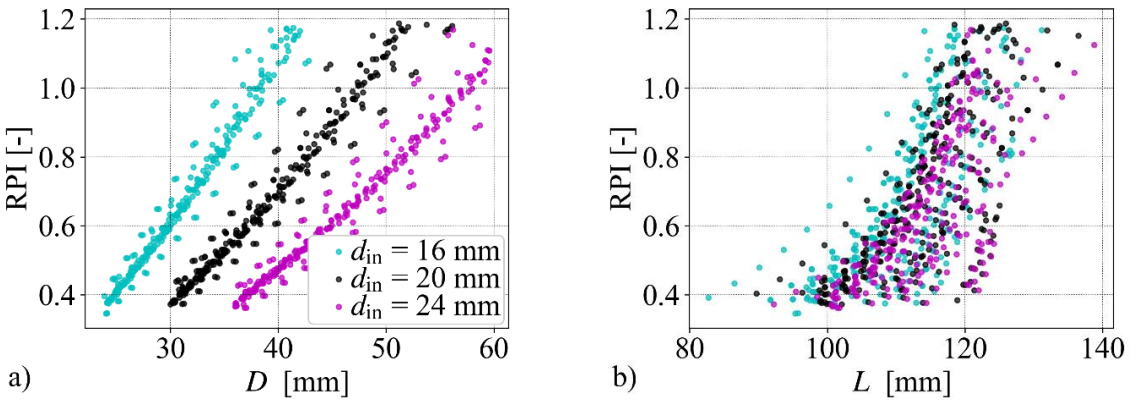

Figure 3.4 The predicted RPI depending on 1D geometrical indices: maximal aneurysmal diameter *D a*), aneurysmal sac length *L b*)

Unsurprisingly, when maximum diameter from Figure 3.4 *a*) is normalized by neck diameter defined as the diameter of the healthy aorta, a very strong correlation can be found, as shown for *Ddr* in Figure 3.5 *a*), with the calculated *r*-value 0.9803.

Table 3 Statistical values (Pearson's correlation coefficient r, mean, standard deviation std.) for different geometrical indices obtained numerically and from the literature. Indices colored in green have relatively high r-value (r > 0.9)

Parameter	***r*-value**		**Mean ± std.**	**Literature** [5]
1D GEOMETRICAL INDICES				
D, [mm]	0.665		38.837 ± 8.444	54.92 ± 11.08
H, [mm]	0.67		111.758 ± 7.73	86.49 ± 22.78
L, [mm]	0.7		112.756 ± 8.089	106.84 ± 29.15
d_1, [mm]	0.0523		23.733 ± 4.081	28.97 ± 4.99
d_2, [mm]	0.324		28.289 ± 5.236	
d_3, [mm]	0.5247		32.266 ± 6.42	
2D GEOMETRICAL INDICES				
T, [-]	0.885		1.009 ± 0.004	1.23 ± 0.11
Ddr, [-]	0.9803		1.964 ± 0.319	1.93 ± 0.43

Ddr at h_1, [-]	0.926		1.64 ± 0.241	
Ddr at h_2, [-]	0.7385		1.373 ± 0.159	
Ddr. at h_3, [-]	0.527		1.203 ± 0.09	
3D GEOMETRICAL INDICES				
S, [cm^2]	0.864		47.4 ± 21.67	80.32 ± 26.14 64.33±28.25 from [83]
V, [cm^3]	0.777		64.816 ± 38.322	154.87 ± 80.16 100.32±52.81 from [83]
NEWLY PROPOSED INDICES				
GRPI, [mm]	0.9585		63.9 ± 12.5	
GRPI at h_1, [mm]	0.9707		54.8 ± 9.2	
GRPI at h_2, [mm]	0.926		47.4 ± 6.1	
GRPI at h_3, [mm]	0.919		42.8 ± 3.7	
NAL, [mm]	0.9643		223 ± 48.716	
NAL at h_1, [mm]	0.9722		185.85 ± 35.961	
NAL at h_2, [mm]	0.9143		155.149 ± 23.338	
NAL at h_3, [mm]	0.904		135.553 ± 13.601	

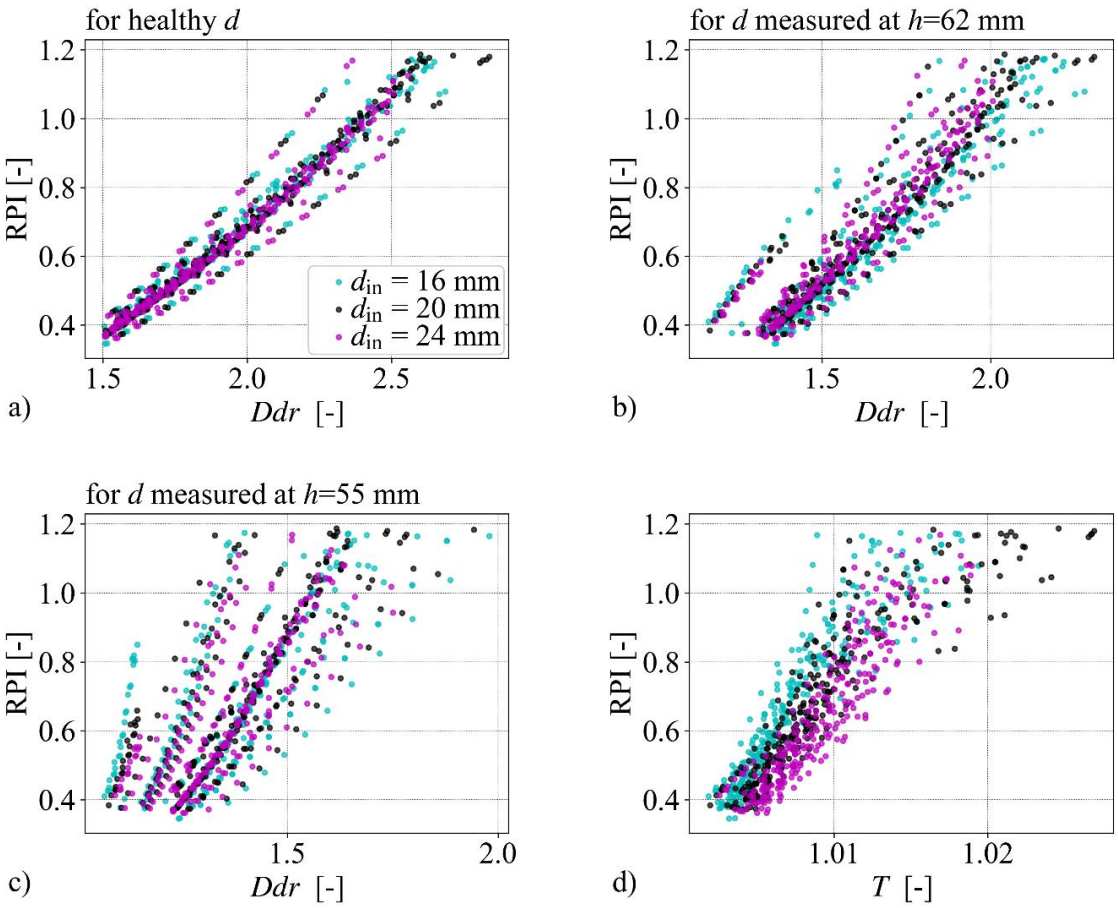

Figure 3.5 The predicted RPI depending on 2D geometrical indices: ratio of the maximum and healthy diameter *Ddr a*); Ddr at height h_1=62 mm *b*); *Ddr* at height h_2=55 mm *c*); and tortuosity *T d*)

Regrettably, it seems that the proximal neck diameter measured from CT scans, at least on large aneurysms, does not seem to relate to a healthy aorta and is dilated (mean values 20 vs. 28.97 mm). For other numerical definitions of proximal neck diameter *d* as diameter at a certain height from the apex, the potential of *Ddr* to predict rupture, shown Figure 3.5 *b*) and *c*), and the correlation factor drop extensively to 0.926, 0.738 and even 0.527 with decreasing height, as shown in Table 3. It can also be seen from the table that with an increase in height and decrease in correlation function, the value of *d* approaches value measured from CT scans.

Tortuosity of the aneurysm, together with length, was one of the four most important geometrical features predicting rupture, as determined by machine learning, [5]. Note that the other two are related to an intraluminal thrombus. Numerically, it surprisingly groups by initial diameter, Figure 3.5 *d*). Although a clear linear correlation can be seen, it is not as strong as for

Ddr. The numerical value of tortuosity is much smaller than the clinically obtained one, possibly because of the prescribed boundary conditions and partially because a healthy artery was modeled as a straight cylinder. In contrast, even a healthy artery is slightly tortuous [102].

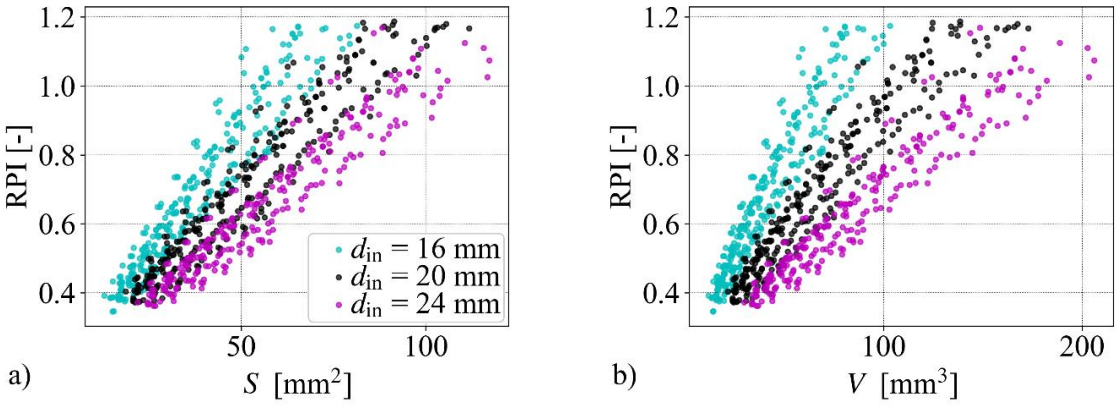

Figure 3.6 The predicted RPI depending on 3D geometrical indices: surface *S a*), aneurysm sac volume *V b*)

Despite AAA volume being considered by many the best alternative for maximal diameter as a criterion for surgical intervention, both AAA volume and aneurysm surface area show clear grouping by initial diameter, Figure 3.6, as could have been expected. Obviously, it is easy to conclude that the normalization of surface and volume might result in a strong correlation of new parameters and RPI. However, unlike the maximum diameter or height, AAA surface and volume cannot be easily computed. Thus, we investigated composite morphological parameters based on 1D indices that could possibly correlate better with RPI. Table 4 summarizes ten parameters with the highest average *r*-value. The geometrical rupture potential index (GRPI) with the highest correlation to RPI is $\mathrm{GRPI} = \dfrac{(LD)^2}{d(4D-d)}$ Note that the average *r*-values are very similar for all composite parameters presented in the table, and small changes in data can easily rearrange the importance of each CMP. It is, thus, difficult to claim which one is the most accurate in predicting AAA rupture, yet we propose all of them are worthy of clinical verification.

The simplest parameter out of top ten, that might be worth considering is $\mathrm{NAL} = \dfrac{LD}{d}$, which could be deemed to be normalized aneurysm length. Despite its average correlation coefficient

being slightly lower compared to GRPI, it is very simple and there are no exponents in its definition, which minimizes the influence of measurement errors.

Table 4 Pearson's correlation coefficients for the ten best composite morphological parameters

Composite parameter	*r*-value (for d_in)	*r*-value at h_1,	*r*-value at h_2	*r*-value at h_3	average *r*-value
$\frac{LD^2}{d(4D-d)}$	0.958598	0.970754	0.925933	0.919237	0.943631
$\frac{(L^2D)^3}{d^2(2D-d)}$	0.95761	0.97065	0.920346	0.921262	0.942467
$\frac{L^2D^3}{d^2}\frac{1}{4D-d}$	0.959145	0.970353	0.925694	0.910063	0.941314
$\frac{L^2}{Dd}(4D-d)^2$	0.947743	0.968989	0.925923	0.921976	0.941158
$\frac{L^2}{d\left(\frac{4}{D}-\frac{1}{d}\right)}$	0.953541	0.96876	0.916443	0.922738	0.940371
$\frac{L^2D^3}{d^2(4D-d)}$	0.96097	0.971706	0.911032	0.915804	0.939878
$\frac{L^2}{Dd(4D^2-d^2)}$	0.940694	0.965403	0.929528	0.923632	0.939814
$\frac{L^2}{d}(2D-d)$	0.949643	0.970174	0.922944	0.916448	0.939802
$\frac{L^2}{d}(4D-d)$	0.941159	0.964661	0.929377	0.92279	0.939497
$L\frac{D}{d}$	0.964299	0.972272	0.914362	0.904772	0.938926

For the first definition of proximal neck diameter, i.e., when it was equal to the healthy diameter, both GRPI and NAL resulted in a very strong correlation to rupture, Figure 3.7 The predicted RPI depending on GRPI *a*) and NAL *b*) for proximal neck diameter defined as a healthy diameter: GRPI *c*) and NAL *d*) for proximal neck diameter defined at height h1=62

mm; and GRPI *e*) and NAL *f*) for proximal neck diameter defined at height h2=55 mm, Figure 3.7 *a*) and *b*). Interestingly, for a healthy radius, NAL has a slightly better correlation. For all other definitions of proximal neck diameter, GRPI remained a relatively stable predictor of rupture. Although there is a slight decline in statistical correlation factor *r*, the reduction is mild compared to *Ddr*. Note, however, that if healthy diameter can be measured or estimated, *Ddr* still has absolutely the best correlation coefficient and definitions of GRPI, and NAL would be unnecessary.

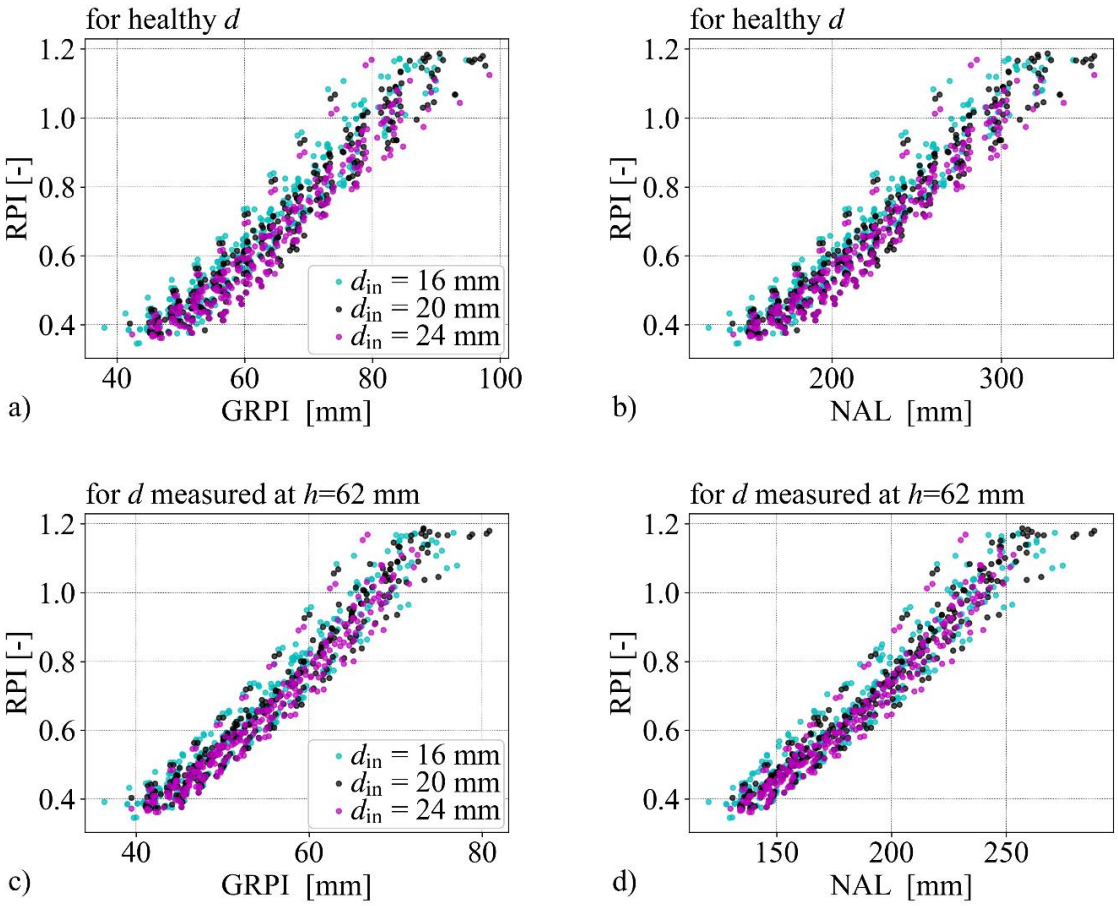

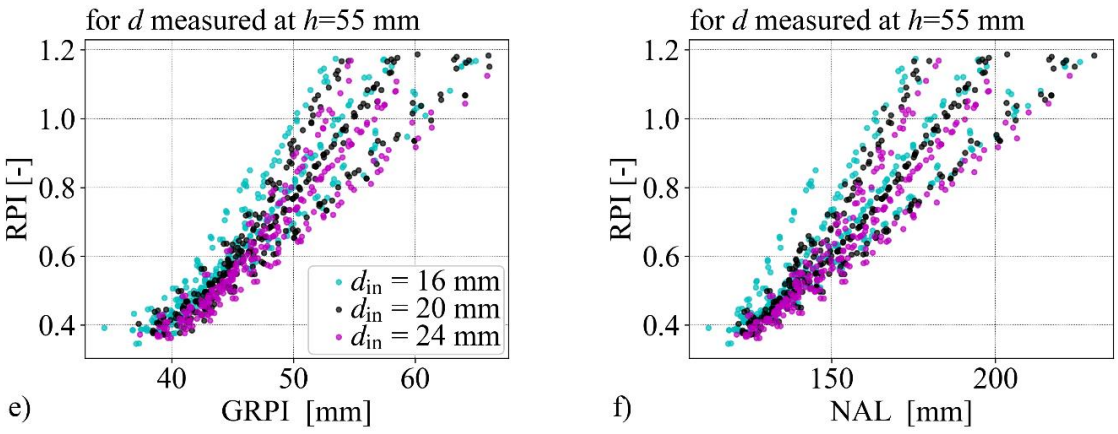

Figure 3.7 The predicted RPI depending on GRPI *a*) and NAL *b*) for proximal neck diameter defined as a healthy diameter: GRPI *c*) and NAL *d*) for proximal neck diameter defined at height h_1=62 mm; and GRPI *e*) and NAL *f*) for proximal neck diameter defined at height h_2=55 mm

3.7. Summary Geometric Factors Affecting AAA Rupture

The prediction of abdominal aortic aneurysm rupture and definition of optimal timing for surgical intervention remain wanting even after decades of histological, clinical, and numerical research. While inflammation biomarkers might have the potential to predict rupture [73], [76], they require harvesting tissue and are thus impractical. Despite numerous attempts to find a geometrical feature more predictive of rupture, such as AAA volume or intraluminal thrombus thickness, clinical decisions remain based on maximal diameter.

Computational biomechanics, especially growth and remodeling (G&R) models, has the potential to increase our understanding of disease progression and rupture. We have previously implemented a numerical G&R model of the aortic wall into finite element code, enabling us to compute aneurysmal behavior and geometry realistically. In order to further validate the model and possibly determine a geometrical index that predicts rupture more reliably, we have run simulations with 114 combinations of input parameters that influence the morphology of the aneurysmal sac. We focused on elastin degradation function and initially healthy diameter, neither of which have been numerically studied, collagen prestretch (and, indirectly, stiffness).

Numerical follow-up has been conducted every six months from the instance of aneurysm formation. During each follow up 1D indices were measured, 2D and 3D size indices were computed, and rupture potential was estimated. Using all acquired data, we show that the correlation between maximal diameter and the RPI is relatively low. Some of the geometrical indices, maximal diameter *D* included, show prominent grouping by initial healthy diameter. The same is valid for surface area *S*, volume *V* and tortuosity *T*. These parameters are obviously inadequate to predict rupture, yet their potential increases significantly when normalized. For example, when the maximal diameter is normalized by a healthy one (*Ddr*) correlation with rupture is very good. Regrettably, healthy diameter is usually unknown, and proximal neck diameter, measured just below renal arteries, is dilated: measured proximal neck diameter is on average 40% larger compared to the numerical one. With the change of numerical definition of the neck, from healthy diameter to a diameter at a certain height from the apex, values of proximal diameter and *Ddr* approach measured values; however, *Ddr* loses potential to predict rupture. Thus, we propose new parameters to predict rupture: geometrical rupture potential index (GRPI) and normalized aneurysmal length (NAL). Both are easily computed from 1D indices without the tiresome processing of CT images. If healthy diameter can be measured (e.g., at the thoracic aorta just above the renal arteries), *Ddr* might be the best feature to predict the rupture. Otherwise, GRPI or NAL seem to be the most reliable parameter for rupture prediction, as statistical correlation factor *r* did not radically decrease when the definition of neck diameter was altered.

It is necessary to keep the model limitations in mind. Because the AAA geometry is idealized (despite being non-symmetric), it is impossible to determine some of the 1D indices defined in [105], such as distal and proximal diameter or height of the neck. This further means some of the 2D parameters could not have been computed numerically (e.g., the ratio of neck AAA height). Moreover, the difference between aneurysmal length and height is not adequately presented, and tortuosity is low. Furthermore, similar to other G&R models, the influence of surrounding tissue or the spine was neglected, and laminar flow was assumed. It is important to emphasize that the presented numerical results were calculated without intraluminal thrombus. Yet, this by no means diminishes the importance of here presented work, as biochemical processes in AAAs with and without thrombus are quite different, and there is no valid rationale for the same geometrical index to be used in both cases. If these parameters can indeed predict rupture of small AAAs that would not be treated under current guidelines, the mortality rate would still be decreased.

Nonetheless, it might be beneficial to verify the proposed parameters using a thrombus-laden model. Towards this end, we have recently presented a finite element model of thrombus-laden AAA [14], although biochemical processes were therein neglected. Based on the literature data and numerical studies that include ILT, we believe that for thrombus-laden aneurysms, a predictor of rupture would be related to surface covered by thin thrombus, as it is likely perilous. A thin thrombus slightly shields the wall mechanically, but it also lowers the production of wall constituents. Biochemically, it is proteolytically very active [42], leading to further degradation of the wall. A thick thrombus prevents the diffusion of proteolytically active molecules from the blood to the wall. Clinically, [5] also concluded that a smaller ILT to aneurysm sac volume ratio leads to rupture, [82] claimed that thicker thrombus slowed down the AAA growth and vice versa, the smaller relative size of ILT was linked to the higher growth rate. Thus, we firmly believe that a biomarker for rupture of thrombus-laden aneurysms must be based on a surface covered by a thin thrombus. Noting that this is very difficult to obtain from clinical imaging, GRPI might remain the most reliable easily calculated parameter predicting rupture.

In conclusion, a good agreement of numerical results and clinical observations gives us confidence in the validity of the developed computational model of aneurysm growth. We believe this shows the potential computational biomechanics can have in expanding the comprehension of the disease itself. Furthermore, it can be helpful with finding the more reliable combination of factors that lead to aneurysm rupture.

4. CFD SIMULATIONS OF AORTIC BLOOD FLOW

The initial step in configuring the model parameters involves selecting the appropriate viscosity model. It is crucial to assess the variations between Newtonian and various non-Newtonian models. Considering the dynamic changes in the AAA geometry, the blood flow regime, and the variations in WSS and blood velocity over time, it is clear that analyzing a single geometry at only one stage of AAA disease is insufficient. Therefore, to obtain a comprehensive understanding, evaluations will be conducted at both the initial and advanced stages of AAA development. The geometry is obtained after each FEAP analysis time as an STL file and is subsequently meshed using *blockMesh*.

4.1. Boundary conditions

Boundary conditions are adopted from Zambrano [107] and [24]. A pulsatile flow is prescribed at the blood vessel entrance, depicted in in Figure 4.1 *a*), with one cardiac cycle lasting exactly one second, corresponding to a 60 BPM pulse rate during a state of rest. The parabolic profile is set on the surface area of the circular cross-section at the blood vessel entrance. At the blood vessel exit, pressure is applied as a pulsating function, illustrated in Figure 4.1 *b*). No-slip boundary condition is set on the AAA and blood vessel walls. Three cardiac cycles are simulated to ensure that results are stabilized over time. Hemodynamical indices are computed from the last cycle so initial conditions would not disturb the calculations.

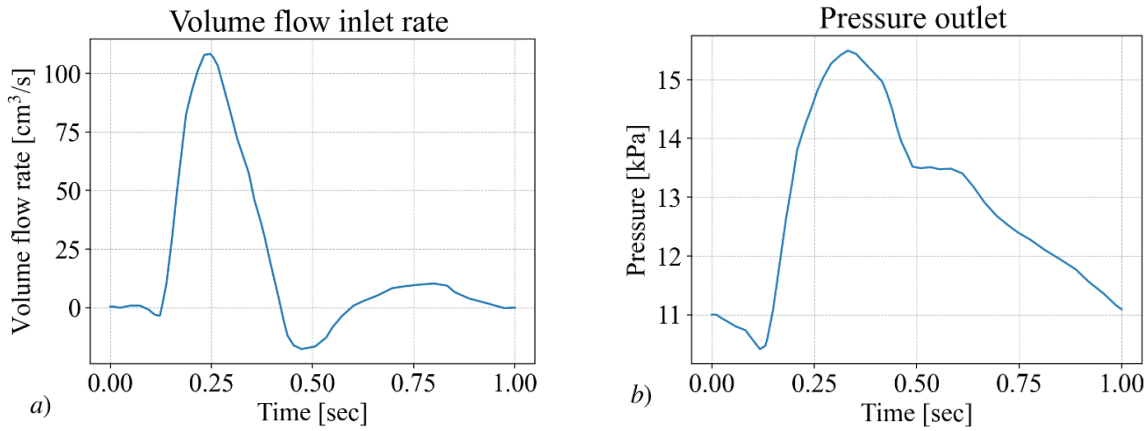

Figure 4.1 Volume flow rate at the inlet *a*), pressure rate at the outlet *b*), both measured over a single cardiac cycle with a duration of one second, repeated periodically

For both examinations, turbulence and viscosity model, similar boundary conditions have been used. Newtonian viscosity model is chosen to compare turbulence properties. Kinematic blood viscosity is selected based on shear-rate analyses and is $\nu = 5 \cdot 10^{-6}\ \mathrm{m^2/s}$ while the density is $\rho = 1060\ \mathrm{kg/m^3}$. For other viscosity models, settings are described in its chapters.

4.2. Geometry

As outlined by Yamamoto [36], the choice of the blood viscosity model should be based on shear rate values. Additionally, the utilization of the Newtonian viscosity model requires the prior determination of shear rate to select the appropriate constant viscosity coefficient, which is contingent on shear rate. The significant drawback of the Newtonian viscosity model lies in the challenge of determining the correct viscosity coefficient. Shear rate undergoes changes with the geometry and during pulsatile flow. To assess which model is more appropriate, shear rate calculations were conducted on two distinct AAA geometries, corresponding to the initial and advanced stages of aorta dilatation. The initial, healthy blood vessel geometry features an inner radius of 10 mm, while AAA geometry with internal radius of 12 mm and 15 mm were chosen to represent initial and advanced AAA sizes. These geometries reflect the disease's progression at 1210th and 2560th days, as depicted in Figure 4.2, which illustrates the contours for the two geometric analyses.

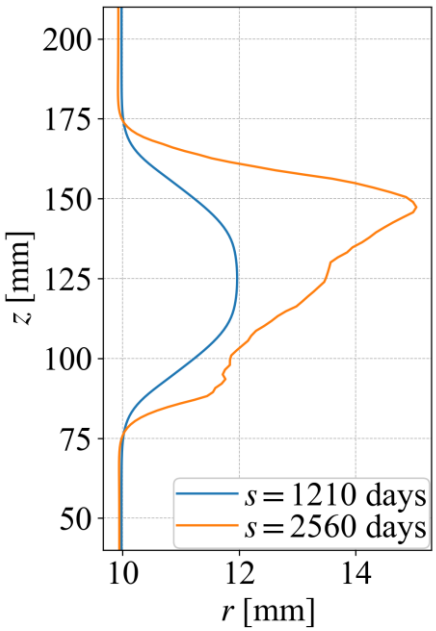

Figure 4.2 Inner radius contour geometries used for shear rate analysis, 1210th and 2560th days after disease start.

4.3. Influence of model characteristics

During the initial phase of setting CFD and FSG model parameters, critical decisions regarding assumptions are essential. These include assessing whether the blood flow in an AAA tends towards a laminar or turbulent regime, selecting the most appropriate viscosity model, and choosing the parameters for the FSG model. The interconnected nature of these decisions poses a significant challenge, as each assumption impacts the others, underscoring the complexity inherent in the modeling process. This interdependence requires careful consideration and coordination, highlighting the intricate balance needed to accurately simulate the physical phenomena involved.

4.3.1. Turbulence model

In the initial example, an analysis of flow characteristics will be conducted, with a specific focus on comparing laminar and turbulent flow. Emphasis will be placed on evaluating the distribution of ILT criteria predictors, given their pivotal role in subsequent analyses and the FSG model. Turbulence was considered homogeneous with an intensity of 1.5%. This value characterizes the turbulence as medium-turbulence case which was chosen because at the beginning stages of FSG simulation the AAA geometry is smaller, and turbulence effects are less likely to appear. The geometry selected for the simulation has a maximal inner radius of 15mm, in order to emphasize the turbulence effects.

With the AAA growth, some turbulence effects may appear, so this is the most suitable solution for both cases. For the first comparison, velocity profiles will be compared for several moments. Due to flow separation, profiles could be different for laminar and turbulent flow. Blood flows for several moments are shown in Figure 4.3.

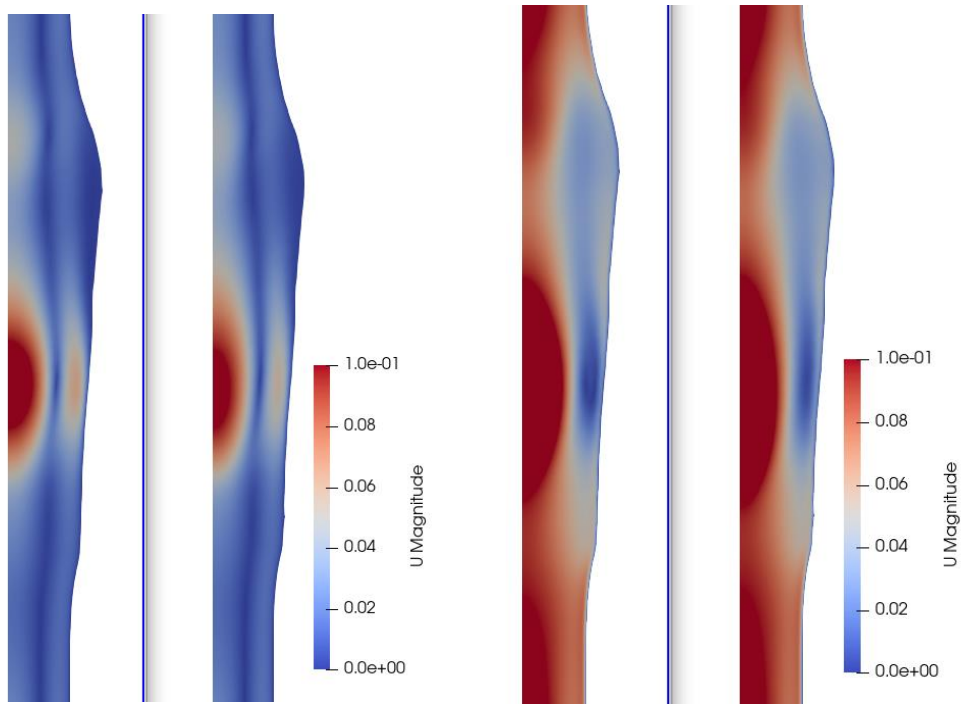

a) *b)*

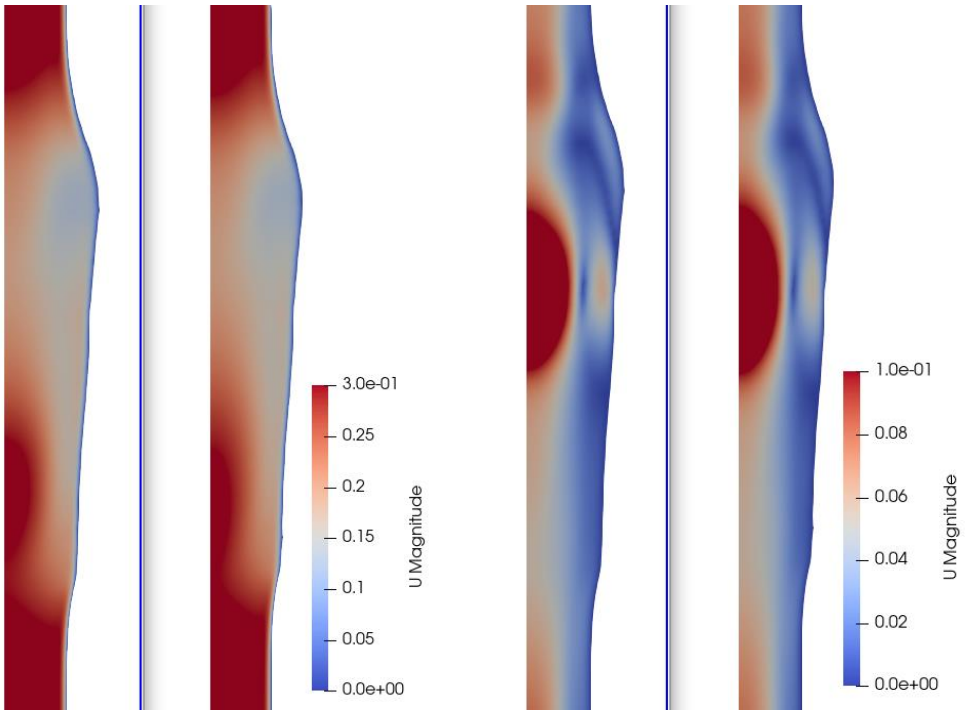

c) *d)*

Figure 4.3 Velocity distribution comparison for turbulent and laminar flow regime in *a)* 0.10s, *b)* 0.15s, *c)* 0.20s, *d)* 0.80s of cardiac cycle. The laminar flow is on the left (*a*) and c)) and turbulent on the right (*b*) and *d*)).

As shown in Figure 4.3 , the velocity profiles exhibit only slight differences between turbulent and laminar flows. The main distinction is observed in the central region of the blood vessel, where turbulent flow shows a broader velocity range, covering more of the AAA height. Key parameters from the CFD analysis include TAWSS, along with OSI and ECAP. TAWSS serves as the primary predictor for the ILT deposition criterion, but this won't be the focus of this chapter. It is worth mentioning that the ILT growth criterion for OSI and ECAP is not yet established. Initially, the TAWSS, OSI, and ECAP distributions will be compared for laminar and turbulent flows on the same geometry.

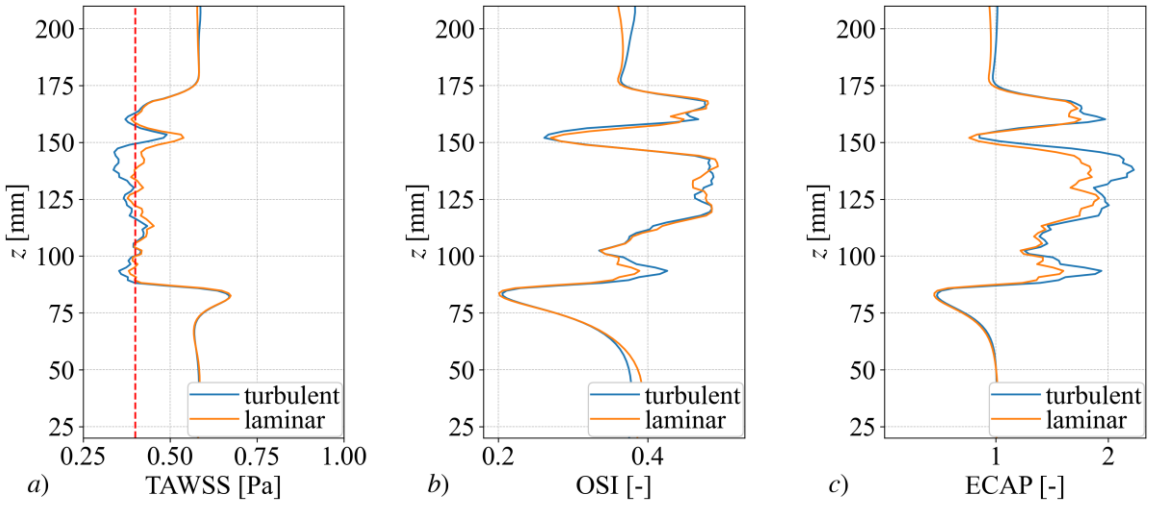

Figure 4.4 TAWSS, OSI and ECAP distribution for the laminar and turbulent flow for Newtonian fluid.

In Figure 4.4 *a*), it is evident that turbulent and laminar flows exhibit a similar pattern in TAWSS distribution, with a more significant difference observed in the upper neck part of the AAA. Turbulent flow values in this region fall below the 0.4 Pa threshold, while laminar flow values surpass it. Although this difference may not appear substantial at first glance, its cumulative impact over numerous cardiac cycles could lead to a markedly different outcome, especially considering its proximity to the threshold value. Consequently, it becomes imperative to conduct a thorough examination of both turbulent and laminar flow regimes in the FSG model. This detailed analysis is essential to accurately capture the complex fluid dynamics and their impact on the structural integrity of the geometry being simulated. The OSI distribution, shown in Figure *b*), for turbulent and laminar flow regimes is more analogous than TAWSS, suggesting that the difference in oscillation (OSI) between turbulent and laminar flows is less pronounced than the TAWSS difference. Considering TAWSS and OSI, it can be

inferred that the difference in ECAP, shown in Figure *c*) distribution should lie between TAWSS and OSI, as it is influenced by both parameters. As observed in the TAWSS distribution, the most substantial difference occurs in the upper neck region.

Both laminar and turbulent model have similar tendencies, although turbulent flow has lower TAWSS values in upper neck region, which means greater tendencies for ILT accumulation. Therefore, higher growth of ILT can be expected if turbulent regime was used. That observation also applies to ECAP distribution and if ECAP was used as ILT deposition criteria. However, due to the possible completely different course of ILT deposition, conclusion cannot be simply made, and further analyses have to be performed. What can be concluded with certainty is that turbulent and laminar regime show sufficiently different outputs which may lead to different disease outcomes.

4.3.2. Viscosity model

Another crucial examination involves assessing the impact of viscosity models, particularly on ILT deposition criteria. The primary criterion for determining which viscosity model to use is based on the shear rate.

Observing the larger AAA with a 15 mm radius reveals an irregular geometry, a characteristic attributed to ILT deposition, although the ILT is not under consideration at this point. To better comprehend the variations in shear rate induced by pulsatile flow and fluctuating blood velocity, three distinct moments have been selected, each representing the maximum, intermediate, and minimum flow during one cardiac cycle. These moments are identified on the volume flow diagram in Figure 4.5, denoted as points A (maximal flow, t=0.25s), B (0.05 seconds after the maximum flow rate, t=0.30s), and C (minimal flow, t=0.5s). The irregularities in the larger AAA geometry, likely associated with ILT, emphasize the dynamic changes in shear rate throughout the pulsatile flow cycle.

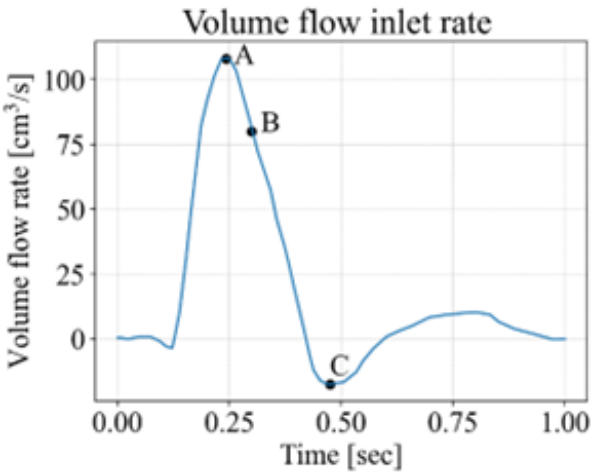

Figure 4.5 Volume flow rate for one cardiac cycle with marked maximal flow rate, *t*=0.25s (A), flow rate 0.05 sec after maximal flow rate (B), *t*=0.3s, and minimal flow rate (C), *t*=0.5s

In Figure 4.5, volume flow rate is shown in three different moments cardiac cycle: for *t*=0.25s, *t*=0.3s and *t*=0.5s. Vertical black lines depict boundaries for optimal blood viscosity model according to Yamamoto [36] : Casson model (C) should be used for shear rates lower than 140 s^{-1}, transient flow model (T) describes blood the best for shear rate between 140 and 160 s^{-1}, while for higher shear rates blood behaves like a Newtonian (N) fluid Figure 4.6 shows, current, non-averaged shear rate values for geometry at two moments in G&R time fluctuate from as low as 10 s^{-1} to as high as 600 s^{-1}, covering all three regions and proposed models. This means that different models should be used in different times at different locations, which is clearly not easy to predict or model.

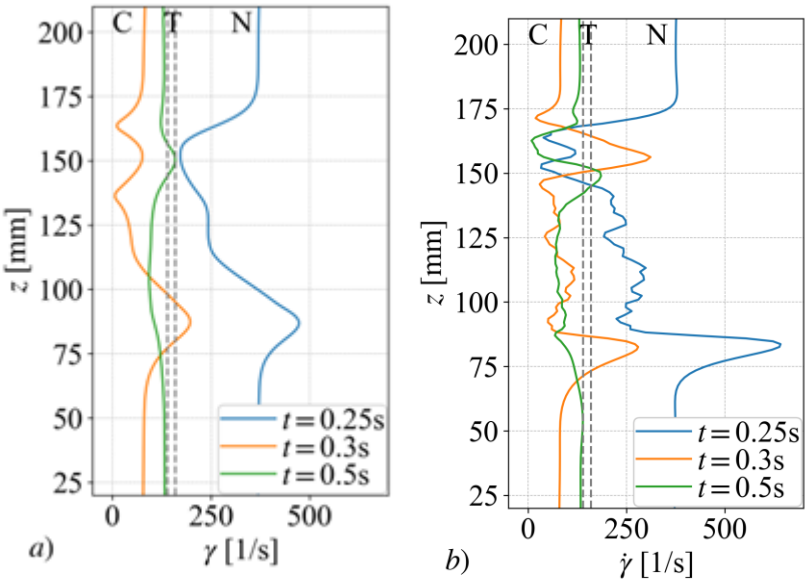

Figure 4.6 Shear rate distribution fin three different moments, for *t*=0.25s, *t*=0.3s and *t*=0.5s, shown in Figure 4.5 analyzed on two different geometries, *a*) 1210 and *b*) 2560 days after disease start

Shear rate varies much from moment to moment because of pulsatile flow. Maximal shear rate occurs when the flow rate is maximal. For the first geometry shear rate is 470 s^{-1} at its maximum and belongs to the Newtonian regime through its all length. Note that, although at the moment of maximum blood flow during the cardiac cycle (blue line in Figure 4.6, shear rate is very high, but already 0.05 seconds later shear rate falls significantly and is in all three regimes, and mostly in Casson region. The difference between shear rate values for earlier and advanced geometry is not expectedly pronounced. However, shear rate distribution for advanced disease geometry is closer to each other in different moments and have more pronounced oscillations. Thus, it can be concluded that model selection is more susceptible to error for later time. Shear rate distributions in all three moments have the same tendency but with a bit more deviations and irregularities. For example, shear rate for maximal flow moment moves partly to the Casson range, but also exceeds more to Newtonian range later. Given that the development of the disease spans several years, it is beneficial to examine how stress behaves over a larger time scale. This approach allows for a more comprehensive understanding of the long-term effects and progression of stress-related changes within the affected structures. For that purpose, time averaging of the shear rate will be done and results will be compared to the results in three moments, t=0.25s, *t*=0.3s and *t*=0.5s,

One cardiac cycle time averaged shear rate (TASR) distribution, for initial and advanced disease geometry is shown in Figure 4.7.

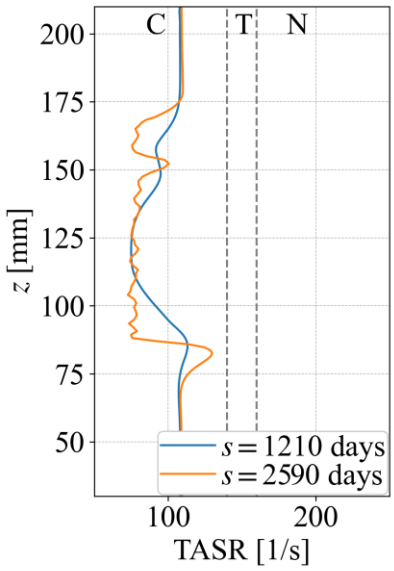

Figure 4.7 Time-averaged shear rate during AAA evolution: at G&R times *s*=1210 days and *s*=2560 days

As can be seen in Figure 4.7, range of time averaged shear rate for both geometries vary between 50 s^{-1} and 140 s^{-1}, which corresponds to Casson viscosity. Case performed on geometry in the later stage of the disease shows much more fluctuations and oscillations which can be attributed to more irregular flow due to irregular geometry. Also, because of the large G&R elements it is not possible to get fine CFD mesh, but that will be explained in the last chapter. Mean shear rates value for the smaller radius geometry is approximately 92 s^{-1} and for the later disease stage geometry is 86 s^{-1}. Depending on the sex and methods used for measuring, kinematic viscosity should be chosen around $\nu = 5 \cdot 10^{-6}\,\mathrm{m^2/s}$ for Newtonian viscosity model, according to Yamamoto. However, with great certainty, shear rate values do not exceed Casson range. Additionally, it is important to note that when shear rate is not time averaged, range of shear rate significantly varies locally and depending on the observed moment of the cardiac cycle. Casson viscosity model can be safely used as the all-time-averaged values are in range, but due to pulsatile flow Newtonian model should be examined also.

4.4. Summary on CFD settings

In this chapter, various analyses were conducted to determine the optimal settings for CFD simulation, with a focus on the viscosity model and turbulence regime selection. According to Yamamoto [36], the choice of the viscosity model should be based on shear rate values.

However, selecting the turbulence regime is more complex, as the changing geometry and blood velocity make it challenging to definitively choose between viscosity and turbulence. Shear rate analysis was conducted on two distinct geometries to compare and better understand the effects of structural variations on fluid dynamics. The first geometry exhibited a 20% increase in radius, totaling 12 mm. It evolved from an idealized tube geometry to a more complex shape at 1210^{th} day of disease development. The second geometry had a maximal radius of 15 mm, growing over 2560 days of disease development. For both geometries, the average shear rate distribution was similar. However, the exact shear rate varied from moment to moment due to pulsatile flow. The maximal shear rate occurred when the flow rate was at its peak, placing the entire shear rate distribution in the Newtonian viscosity regime during that moment. However, shortly after, 0.05 seconds, the shear rate dropped significantly, mostly falling within the Casson regime, as well as in almost all other moments. A similar situation is observed for both the initial and advanced geometries. Considering all the factors mentioned, the Casson model should be chosen, primarily based on the shear rate analysis.

After comparing different viscosity models, some differences are observed too. The viscosity coefficient is directly correlated with the TAWSS value for the Newtonian viscosity model. Therefore, it is crucial to determine the viscosity coefficient correctly. However, due to changes and irregularities in geometry and the pulsatile nature of flow, determining it precisely is challenging. It can be done as an average value, but this may not cater to different geometry shapes and velocities. Moreover, after shear rate analysis, it would be better to choose the Casson model as it automatically considers changes in shear rate. The mitigating circumstance is that the Casson viscosity model provides very similar results compared to Newtonian if the viscosity coefficient is well defined.

The difference in turbulent and laminar regimes was not pronounced when considering blood velocity and ILT deposition criteria (TAWSS, OSI, and ECAP). The most significant difference was observed in TAWSS distribution in the upper neck region where flow separations occur. OSI distribution was similar across the entire area. Since it is challenging to precisely determine turbulence characteristics, and most current works consider flow as laminar, it will be considered as such. Additionally, turbulent flow incurs higher computational costs, which could further slowdown an already very complex model. As mentioned, although the differences in turbulence character or viscosity models may not seem significant, there is a question of whether errors will accumulate in the FSG model due to many iterative fluid-solid analyses.

This becomes crucial because of the ILT deposition criterion and the delicate decision of whether ILT will be created or not.

5. FSG MODEL AND SETTINGS

This final chapter demonstrates the impact of various model settings, particularly blood viscosity models, on the shape of the ILT location. Furthermore, a CFD analysis investigation was conducted into the influence of different deposition criteria from the literature, such as time-averaged wall shear stress, oscillatory shear index, and endothelial cell activation potential, on the locations and morphology of thrombus. The study also delved into the effects of different threshold values for TAWSS parameter. Lastly, the chapter demonstrates how minor changes in the morphology of the aneurysm sac can impact hemodynamics and, consequently, thrombus deposition.

5.1. Influence of blood viscosity model

Hemodynamic and ILT deposition parameters, such as TAWSS or OSI are highly influenced by the viscosity of the fluid. While blood is generally acknowledged as a non-Newtonian fluid, its viscosity is intricate, making it challenging to characterize with a single viscosity model. As a result, various models, including Bird-Carreau, Carreau-Yasuda, and Casson models, have been proposed to model blood viscosity. Additionally, in certain flow regimes and shear rates, blood behaviour may approximate that of a Newtonian fluid [36]. Therefore, our investigation explored thrombus deposition using two non-Newtonian blood models: Casson and Bird-Carreau (with parameter values obtained from OpenFOAM literature) and three kinematic viscosity values falling within the physiological range for blood.

ILT size and shape are used as the primary criteria for evaluating viscosity models. The analysis was evaluated using TAWSS as the criterion because it is the only parameter with a stated threshold value in the literature (0.4 Pa), as proposed in [24]. All cases are displayed at the specific moment when the outer radius reached 16 mm, in order to highlight the greatest differences between models, as this point in time shows the most significant changes. Figure 5.1 *a*) shows the inner wall and inner ILT contours at moments when the maximum diameter is consistent.

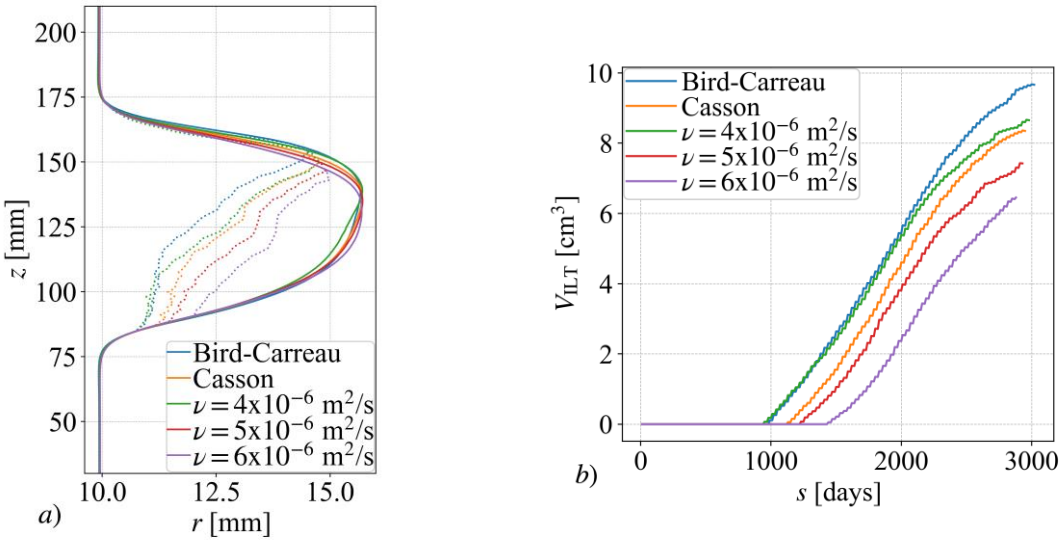

Figure 5.1 Inner and ILT contours at the same maximum AAA radius of 15.3 mm *a*), growth of ILT volume *b*) for different threshold viscosity models

It is evident that higher viscosity values lead to increased wall shear stress. Consequently, a significantly larger dilation of the AAA sac is required to reach the threshold value when the viscosity is higher. For instance, in Figure 5.1 *a*), comparing the green, red, and purple lines representing Newtonian flows with different viscosities shows that the ILT is thinner at higher blood viscosity values. Additionally, the non-Newtonian Bird-Carreau model results in the thickest thrombus, whereas the Casson model yields a thrombus of median thickness.

The impact of defined blood viscosity on the delay in ILT formation is clearly illustrated in Figure 5.1 *b*), which depicts the increase in ILT volume over time. Interestingly, after the initial thrombus formation, the growth rate of thrombus volume appears to be independent of viscosity, as all curves in Figure 5.1 *b*), exhibit almost identical steepness.

5.2. Influence of TAWSS threshold value

One of the most proposed criteria for thrombus deposition is time averaged wall shear stress. Most studies stated that low WSS values corresponds to ILT accumulation, yet most of them do not define the exact value of TAWSS that predicts thrombus deposition. The exception was Zambrano [24], who suggested threshold value for TAWSS, below which the accumulation of ILT begins, has a value of 0.4 Pa. It's crucial to note that this value is derived from CFD analysis

using the Carreau–Yasuda model. However, this threshold value may be subject to variation when employing FSI analysis, a different viscosity model, or even different initial conditions for flow and pressure. Recognizing this variability, our investigation focused on understanding how changes in the TAWSS threshold value can impact the deposition times, shapes, and growth patterns of intraluminal thrombus. Setting the TAWSS condition too low may result in no ILT deposition, while setting it too high may lead to an unrealistic occlusion of the lumen by ILT. The size and position of the ILT wall are closely tied to the critical TAWSS value, influencing whether ILT fills the lumen up to the healthy wall boundary while maintaining the same volume as the healthy vessel or if the lumen continues to grow with the ILT boundary moving toward the abluminal direction.

The objective is to illustrate the variations in ILT growth and deposition patterns for each case. Inner diameter growth and ILT volume expansion are depicted in Figure 5.2. A discernible trend emerges, showcasing an increase in ILT thickness with a higher TAWSS threshold. However, the shape of the ILT wall differs across cases. For instance, in the case with a marginal threshold of TAWSS=0.45 Pa, the neck regions are more pronounced, and the middle part moves upward and away from the axis. Similar trends and shapes are observed in other cases. As anticipated, cases with lower critical values tend to exhibit less ILT on the wall. Notably, all cases exhibit pronounced asymmetry, with ILT being predominantly deposited in the lower neck region.

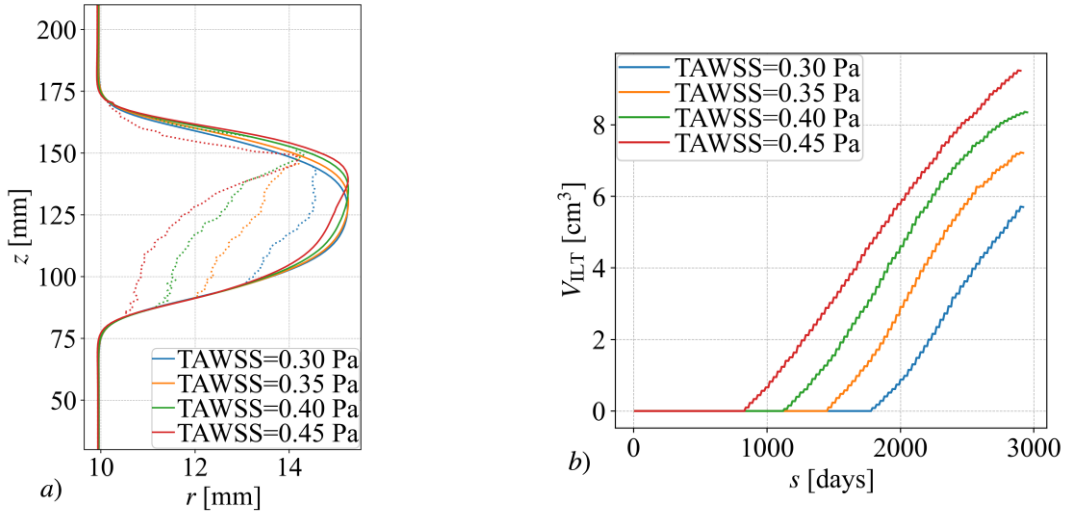

Figure 5.2 Inner wall and ILT contours at the same maximum AAA radius of 16 mm *a*), ILT volume over time *b*), for different threshold TAWSS values

Furthermore, Figure 5.2 *a*) show that AAA shape does not remain vertically symmetrical, due to asymmetrical ILT deposition. For TAWSS as a deposition criterion, ILT tends to first accumulate more towards distal region, close to the iliac bifurcation. This is to some extent analogue to what happens in reality: according to Figure 2b in [24] showing the ILT thickness distributions of 14 patients at their last scans, it is easy to notice that thrombus accumulates more on the distal part of the AAA sac compared to proximal side, especially for patients P-5 and P-8. Furthermore, based on figure 3 in [24], the authors concluded that for all patients ILT formed at the region of maximum diameter and over time spread to the surrounding areas while simultaneously increasing ILT thickness on areas previously covered by ILT. This is fully matching the computationally obtained results, as first thrombus layer forms at location of maximum radius, see Figure 2.16 *c*), and further amasses around this location.

Yet, it can be noted interesting differences in ILT growth pattern based on threshold value of TAWSS. Figure 5.3 shows that for high TAWSS threshold of 0.5 Pa (green lines), close to a TAWSS value at the healthy descending aorta, AAA is practically fully thrombosed and ILT is almost symmetrical. Note that, when only mechanical influence of ILT is taken into account, fully thrombosed aneurysms are much more stable compared to the partially thrombosed ones, [14], and it did not grow to the maximal AAA radius of 15 mm (thus, there is no green line shown in Figure 5.3 *c*).

When TAWSS threshold is set to value lower than 0.45 Pa, thrombus grows from the apex in the beginning, shown as orange line in Figure 5.3 *a*), but at certain geometry a thin thrombus deposits on the proximal side, Figure 5.3 *b*). Over time, larger distal and thin proximal thrombus connect into a unified thrombus mass, shown in Figure 5.3 *c*). However, the crater in the ILT shape does not fill at any point. Lowering the threshold values results in the delayed formation of a thin thrombus on the proximal side; this is only visible in Figure 5.3 *c*) for a threshold of 0.4 Pa.

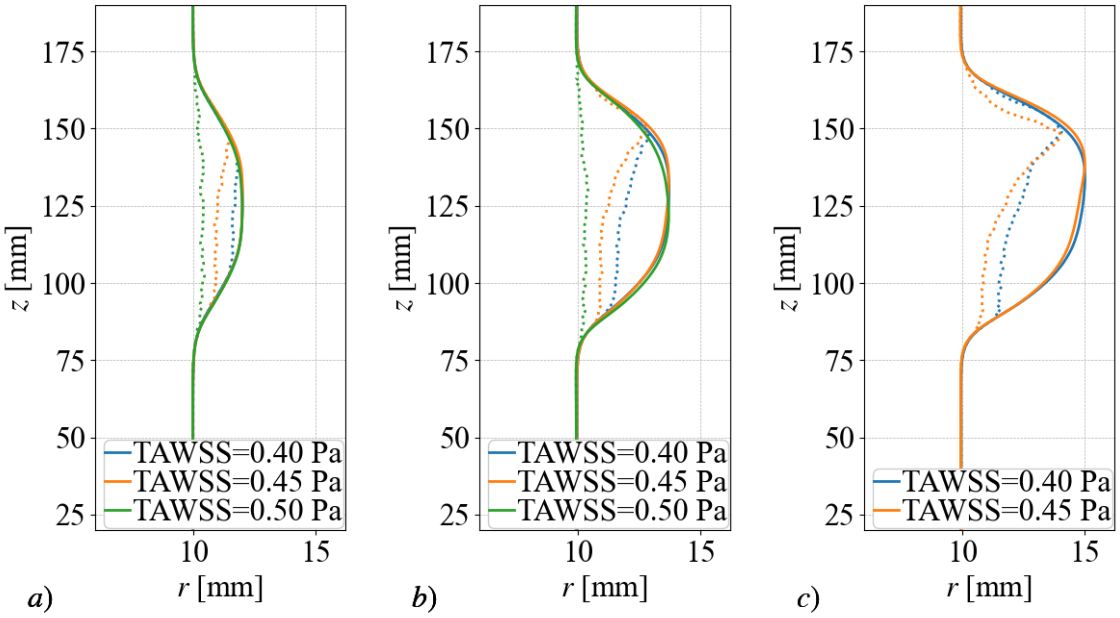

Figure 5.3: Thrombus contours for different TAWSS threshold values at maximum AAA radius of 12 mm (a), 13.7 mm (b), and 15 mm (c)

It is clearly seen that the lower the TAWSS threshold was set, the greater is ILT volume. That coincides with the claim that ILT volume growth rate will also be bigger for lower threshold. But here is also important to notice that the time of ILT deposition is not the same and varies depending on the threshold. As expected, ILT volume growth has the similar rate for all cases, as in *c*). Herein, the only difference is the timing of when the ILT begins to deposit. That impact the current geometry shape but seems to have no major difference. Additionally, lumen is kept stable by continuously depositing ILT elements. Circumferential stress growth over time is also different for each case, shown in figure *d)*. Stress was monitored at the initial node of the inner radius, a critical point for rupture in every AAA, over the entire contour length. Therefore, the node exhibiting the maximum stress over the whole AAA was identified at each timestep. The curves in the diagram suggest that thicker ILT contributes to reducing peak wall-shear stress in the advanced stage of AAA when the ILT is more substantial. This aligns with the observation that ILT redirects blood pressure from the radial direction. A noteworthy difference is observed: stresses in AAA cases with a higher TAWSS threshold value tend to stabilize, while those with a lower value continue to grow continuously. In the case with a TAWSS threshold value of 0.45 Pa, a gap in the middle of the ILT is apparent, attributed to the imperfection of the Casson viscosity model and the relatively coarse mesh. Conversely, the case with a threshold value of 0.4 Pa appears satisfactory and will be utilized in the subsequent example.

5.3. Influence of turbulence

For the comparison between the turbulent and laminar models, the Newtonian viscosity model was utilized featuring a viscosity coefficient of $\nu = 5 \cdot 10^{-6}\ \mathrm{m^2/s}$. Turbulent and laminar models will be compared to get better impression in possible ILT formation differences, as the different turbulent regime may affect the flow image which affects the wall shear stress. As shown in chapter 2.3, the differences observed for one time step were not substantial, both in terms of TAWSS and velocity distribution. However, given the cumulative error characteristic during FSG model iterations, it is imperative to reevaluate. As mentioned earlier, turbulence was assumed to be homogeneous with an intensity of 1.5%, placing it within the medium-turbulence range. All other settings are the same as described in chapter 2.3.

Figure 5.1 *a*) shows the inner wall and inner ILT contours for the moments when radius r_{max}=13mm. This case was chosen because the AAA is relatively small, yet the differences are still visible. Note that ILT deposition starts when r_{max} = ~ 11.7 mm. Additionally, stress contours will be shown for the same moment to see how ILT helps to reduce the peak stress.

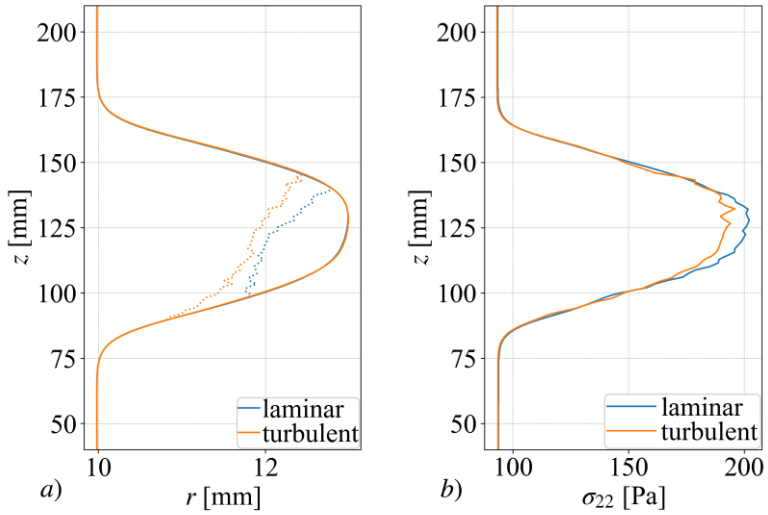

Figure 5.4 *a*) Inner wall radius and inner ILT contours, *b*) stress distribution when r_{max} = 13mm for laminar and turbulent Newtonian viscosity model.

From Figure 5.4, it is evident that the inner walls for both cases are the same, but there is a significant difference in ILT size. Turbulent flow tends to harbor a much larger ILT, and it also initiates slightly earlier, as shown in Figure 5.6. Both ILTs originate from the same location, at the bottom central side of the aneurysm, and then spread upwards. This observation also highlights how ILT contributes to reducing circumferential stress in the region where ILT is thicker. With the same inner radius, the difference in stress is solely attributable to ILT deposition as it takes over a portion of the stress tension.

Figure 5.5 shows inner wall and ILT contours for the radii r_{max} = 14 mm and r_{max} =16 mm. In Figure 5.5 *b*) it can be noticed that ILT size and shape for r_{max} = 16 mm especially, is even more different for turbulent model than compared when r_{max} = 13mm.

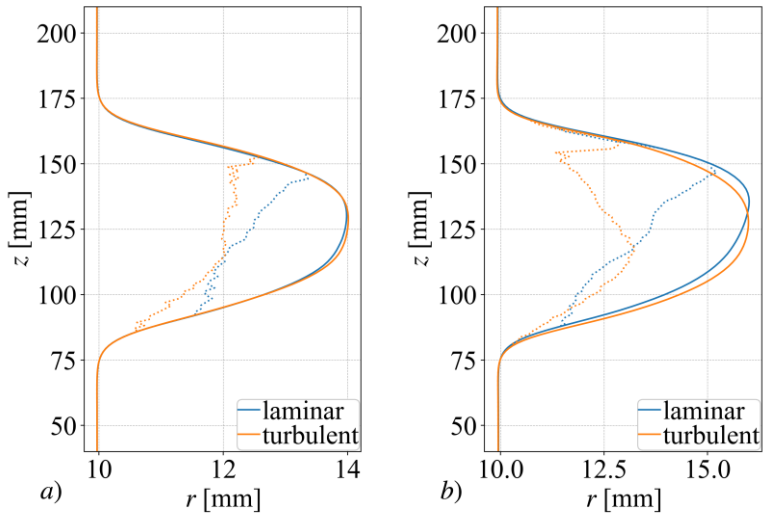

Figure 5.5 Inner and ILT contours when a) r_{max} = 14mm, and b) r_{max} =16mm for laminar and turbulent Newtonian viscosity model.

Figure 5.5 shows a substantial difference in ILT deposition between the laminar and turbulent models, with the turbulent flow regime exhibiting a tendency to accumulate more ILT. Similar to all other model cases, ILT is asymmetrical and mainly situated in the lower part of the aneurysm for r_{max} = 14mm. However, in contrast to all other cases and times, as observed in Figure 5.5 *b*), the turbulent regime positions the ILT much more toward the upper neck region. Due to the size and shape of ILT, different tendencies can be expected for several quantities in later stages due to the asymmetry and relocation of ILT towards the upper part of the aneurysm.

Figure 5.6 shows the growth of all important quantities over time for both laminar and turbulent flow.

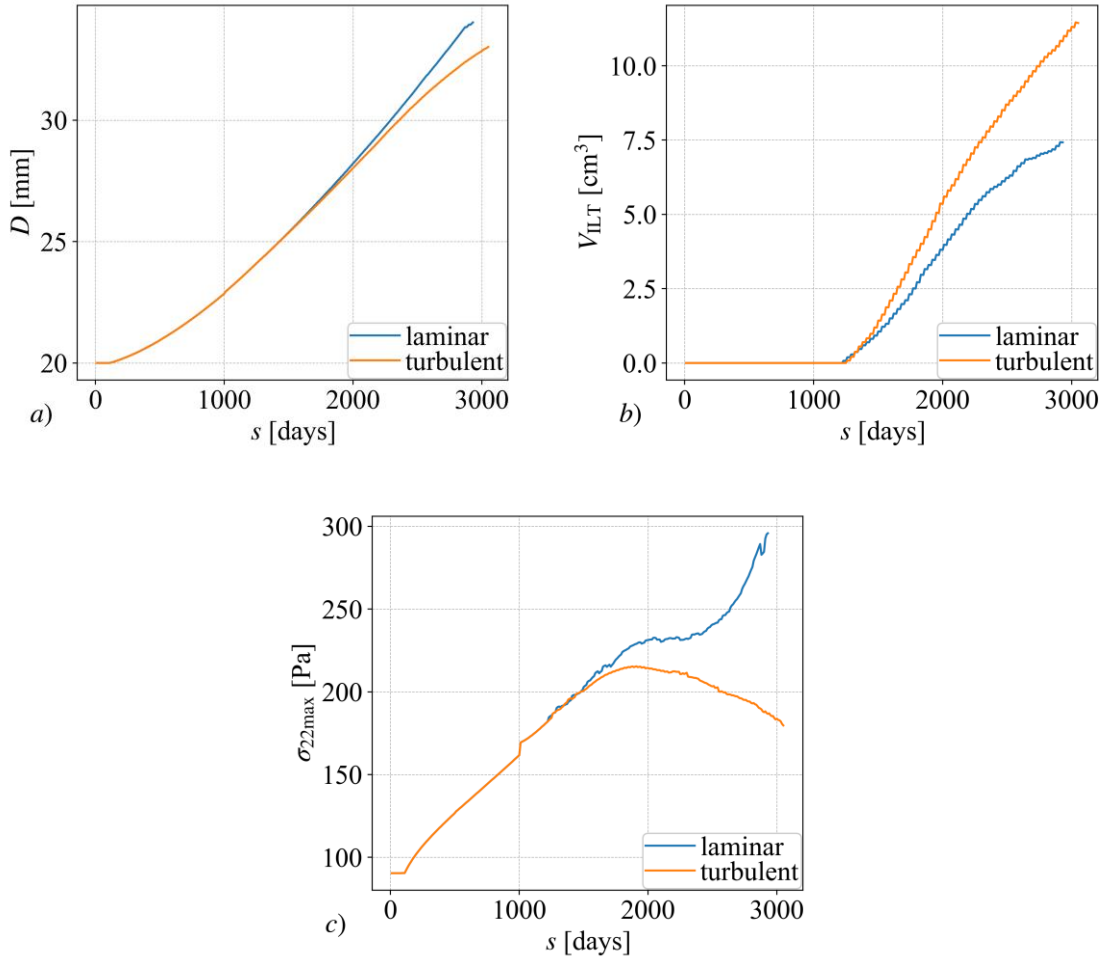

Figure 5.6 Inner diameter *a*), ILT volume *b*), maximal circumferential stress *c*), over time for laminar and turbulent flow

It can be observed that the laminar and turbulent cases exhibit significant differences in all the listed quantities. The most noticeable distinction is in the size and deposition rate of ILT, as shown in Figure 5.6 *b*). The deposition initiates at the same time for both models and grows at its own continuous rate. The deposition rate slows down for the laminar case in the later stage, after 2400 days from the disease start, while it continues almost linearly for the turbulent case. However, the deposition rate is approximately 50% faster for turbulent flow. The size of ILT influences both stress and the maximal value. In Figure 5.6 *a*), the difference in diameter size becomes noticeable only after 2000 days, and the gap widens with time.

However, there is not much difference in maximal radius growth until r_{max} = 15mm, or 2300th day from AAA start, as it can be seen in V_{ILT}. The laminar case has a bigger wall dilatation because of less ILT deposited, resulting in less stress transferring. At the very end of the growth process, r_{max} is roughly 10% larger for laminar case.

On the other hand, there is a huge difference in stress distribution. In Figure 5.6 *c*), it can be noticed that stress is increasing throughout the whole time for the laminar case, but at a variable rate. In the initial 1800 days, the maximal stress is quite similar for both cases. However, in the last 500 days, stress rapidly escalated in the laminar case after a period of stagnation lasting 300 days. During the final 500 days, the maximal stress decreases for the turbulent case, suggesting, in theory, a reduced risk of AAA rupture, which is directly connected to ILT thickness. Nevertheless, before drawing such a conclusion, additional parameters must undergo examination.

Due to very different ILT growth process and marked irregularities in results, $H_{D_{max}}$ and $H_{\sigma_{22,max}}$ will be presented to give more insights what is happening. $H_{D_{max}}$ and $H_{\sigma_{22,max}}$ are shown in Figure 5.7.

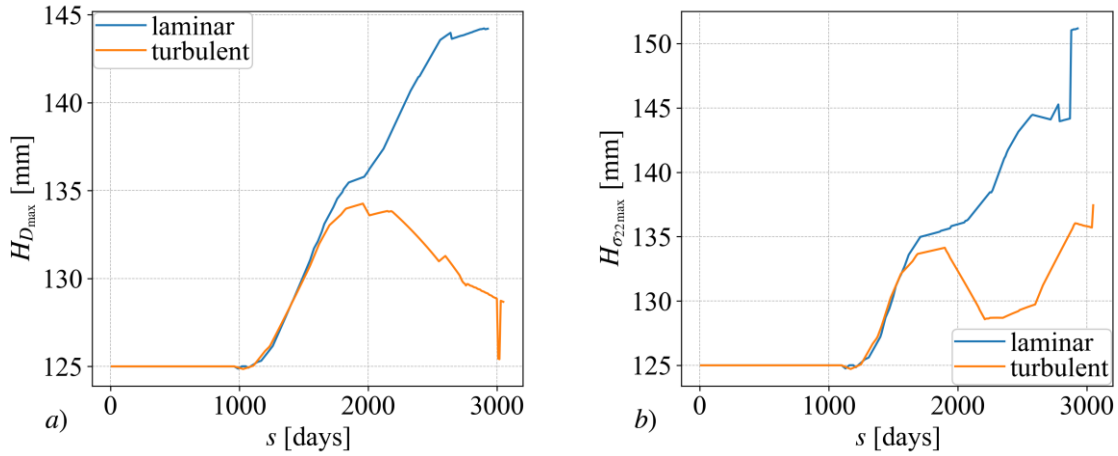

Figure 5.7 Maximal diameter height *a*), maximal circumferential stress *b*), over time for laminar and turbulent flow

As explained previously, $H_{D_{\max}}$ is closely connected to ILT shape and location. As seen in the Figure 5.7 *a*), for the initial 1500 days both cases have the same $H_{D_{\max}}$, despite different ILT size. That implies that the ILT is situated at the same vertical position on the aneurysmal wall. Figure 5.7 *b*) confirms that assumption because $H_{\sigma_{22,\max}}$ is also the same for the first stage of ILT growth. In the mature stage of AAA growth, after 2000 days from the disease start, $H_{D_{\max}}$ is totally different for laminar and turbulent cases. ILT location for laminar case continues to descend towards AAA bottom neck region and therefore $H_{D_{\max}}$ continues to increase. By the end of simulation, $H_{D_{\max}}$ increased for almost 20 mm. Given that the aneurysmal height is slightly over 85 mm, this difference is quite substantial. However, because of different ILT deposition processes, $H_{D_{\max}}$ for turbulent case returns towards initial location, in the middle of aneurysm, at height of 125mm. That tendency is pronounced as the $H_{D_{\max}}$ decreases continuously till the simulation end. $H_{\sigma_{22,\max}}$ diagram looks very similar to $H_{D_{\max}}$ diagram for the laminar case, in contrast to turbulent, which shows increase in $H_{D_{\max}}$ and $H_{\sigma_{22,\max}}$ in the last 500 days, due to a change in the ILT center of mass.

In a single geometry CFD simulation case, turbulent and laminar models did not exhibit significant differences in TAWSS values. The results appeared very similar, both in distribution and values. However, when analyzed within the FSG model, notable differences emerged. The laminar model tended to accumulate ILT in the lower region consistently throughout the simulation. On the other hand, the turbulent model, in the early stages, deposited ILT in the same location but shifted its deposition direction toward the upper part of the aneurysm after 1700th day. Additionally, the ILT size in the turbulent model was 50% larger, influencing and modifying the critical location for potential rupture. That is clearly seen in the $H_{\sigma_{22,\max}}$ diagram in the Figure 5.7 *a*). When compared to the literature, Zambrano [24] showed that ILT starts to deposit at the lower part of aneurysm and then spreads towards upper part, and that statement is closer to the results obtained from the turbulent model.

5.4. Influence of aneurysm sac shape

The chosen geometrical parameter Δz_{MED}, was modified to evaluate its influence on the AAA configuration during the FSG analysis. Considering the AAA's length, ILT could accumulate in different areas, including the neck region or more centrally. Based on prior observations, some variations in the shape of the AAA were expected. The subsequent figures, similar to those in earlier comparisons, are plotted in Figure 5.8.

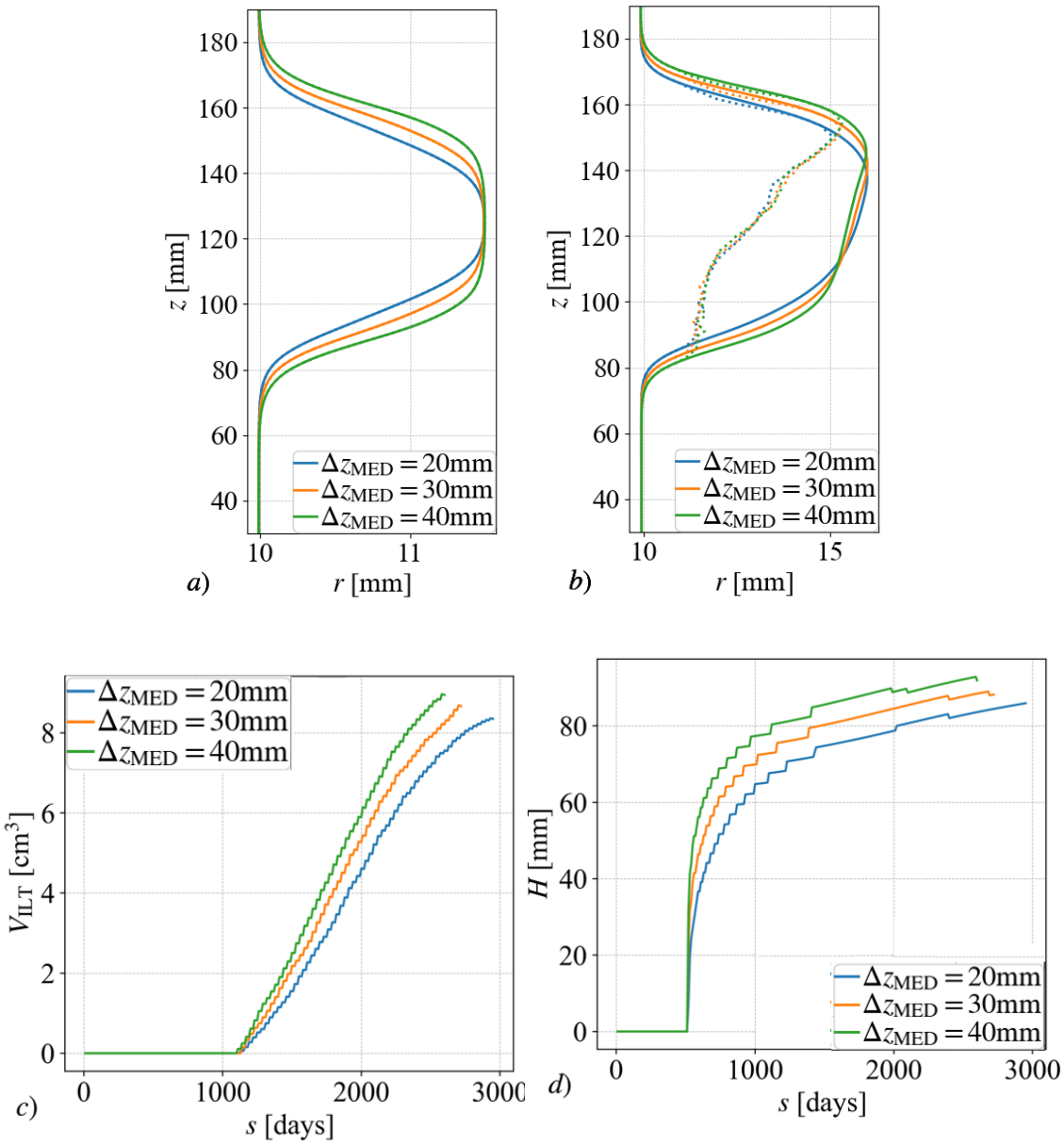

Figure 5.8 Diagrams for different Δz_{MED} geometrical parameter: Inner contours when r_{max} =12 mm *a*), Inner and ILT contours when r_{max} =16 mm *b*), ILT volume over time *c*), and AAA height over time *d*)

Figure 5.8 *a*) and *b*) shows inner wall radius and inner ILT contours for different geometrical parameter Δz_{MED}. Significantly, in figure *a*), the alterations in the AAA's shape and its inner contour are pronounced. When examining different values, the length of the AAA is markedly extended in the 40 mm and 30 mm configurations when contrasted with the 20 mm setup. Despite these variations, the ILT contour remains broadly uniform. As depicted in Figure 5.9 *c*), the rates of diameter growth are virtually identical. However, despite these comparable patterns in AAA shapes, the ILT volumes illustrated in Figure 5.9 *c*) exhibit notable disparities in their numerical figures. This discrepancy indicates that while the general geometric features of the aneurysm may bear resemblance, the precise distribution and buildup of the intraluminal thrombus within the sac are dictated by elements other than just the geometric parameters.

In the Figure 5.9 *d*), it can be seen significant difference in maximal circumferential stress. As observed earlier, instances with a thicker ILT tend to exhibit a lower value of circumferential stress. This correlation highlights the potential influence of ILT thickness on stress distribution within the aneurysm sac. Model case with Δz_{MED} = 40 mm exhibits the least increase in circumferential stress over time when compared for the same duration. An interesting observation is noted in the stress diagram. Unlike other comparisons, stress stabilizes for a certain period but then resumes growth for all cases. This indicates that the stabilizing effect is not solely connected to this parameter. Considering the final stress and ILT volume growth, it can be concluded that these AAA cases will not stabilize.

5.5. OSI and ECAP as ILT deposition criteria

Oscillatory shear index (OSI) and endothelial cell activation potential (ECAP) are other parameters used for modeling ILT deposition. To our knowledge by far, there are not specified threshold values for OSI and ECAP in the literature to be used as ILT deposition criteria. Therefore, the goal of this chapter is to find the most suitable values and compare it to TAWSS criteria. According to Bhagavan et al. [26], high OSI values regions promotes ILT formation and it can be compared to low TAWSS regions. Bhagavan stated that OSI was high within the lesion (OSI=0.33 on average) where otherwise TAWSS has low values and vice versa, OSI had lower values in the healthy aorta segment (OSI=0.27 on average). However, Bhagavan et al. used idealized geometry of the real, geometrically complex, patient-specific representation of aneurysm. In addition, due to irregular geometry, this model is not geometrically like ours and

cannot be directly compared. Their maximal diameter was ~45mm which is significantly larger than ours, as ILT usually harbors earlier due to TAWSS criteria. Because of all things listed, OSI values cannot be used as fixed threshold values and need to be adjusted. However, high OSI promotes ILT deposition and that is the guideline that will be used. Everything also applies to ECAP parameter. As ECAP is calculated as OSI divided by TAWSS, high ECAP promotes ILT deposition also.

The initial challenge is determining an effective method to compare the similarities between cases involving TAWSS, OSI and ECAP. The chosen approach involves comparing the growth of maximal diameter and ILT volume over time. This comparison is crucial, particularly after the turbulent and laminar cases are examined, as the growth rate significantly influences the final appearance of the AAA and ILT. It is important to note that the shape of the ILT may not necessarily mimic the original model, providing motivation for further research. Throughout this analysis, the Casson viscosity model and laminar characteristics were used for blood flow modeling, along with standard G&R parameters detailed in the Chapter. 2.3.

Throughout this analysis, many various threshold values were tested to identify the optimal outcomes. To streamline the presentation and focus on the most promising results, only the best options will be showcased. For the OSI, the chosen threshold value is OSI=0.4575, and for ECAP, the selected threshold value is ECAP=1.54. Diagrams of the D_{max} and V_{ILT} are shown in Figure 5.9.

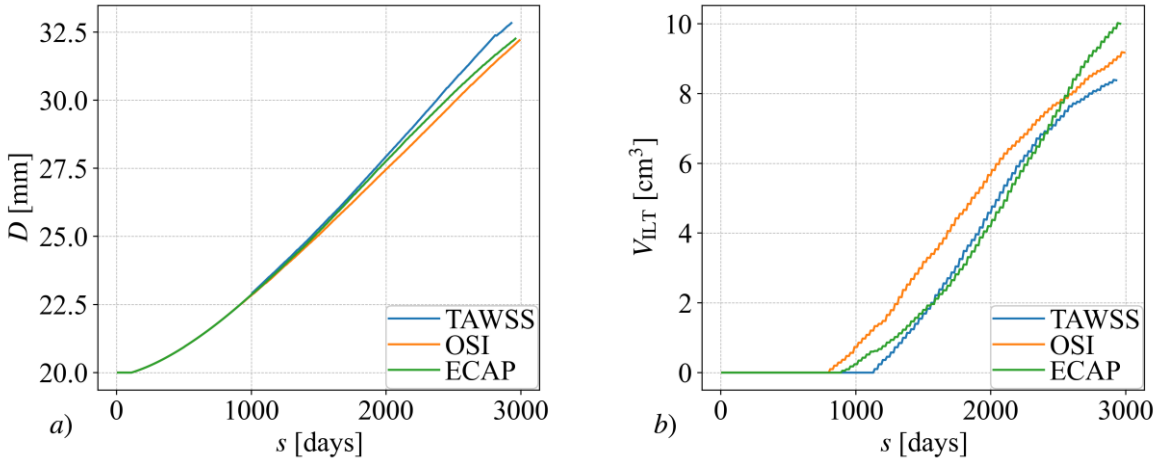

Figure 5.9 Inner maximal diameter *a*), and ILT volume *b*) over time for cases that use TAWSS, OSI and ECAP parameters as ILT predictor.

In Figure 5.9 *a*), there can be noticed a minimal variation in D_{max} between different ILT deposition criteria models. Both the final diameter size and growth rate exhibit similarities. In Figure 5.9 *b*), the TAWSS and ECAP models demonstrate close resemblance throughout the entire duration, except for the last 500 days. During this period, ECAP continues to grow consistently, while TAWSS experiences a decline. Additionally, ECAP initiates ILT deposition slightly earlier, but after 200 days from the start of ILT deposition, both sizes and growth rates align. In comparison to TAWSS, OSI shows more distinctions. ILT deposition begins 300 days earlier than TAWSS, maintaining a consistent growth rate and resulting in a consistently larger ILT. The difference is approximately 2 cm^3, implying that TAWSS would need 300 days to reach the OSI volume. However, when considering contours for the same inner diameter in Figure 5.10, this difference may not be problematic. Inner and ILT contours will be illustrated when the maximal radius is r_{max}=13mm, r_{max}=14mm, r_{max}=16mm.

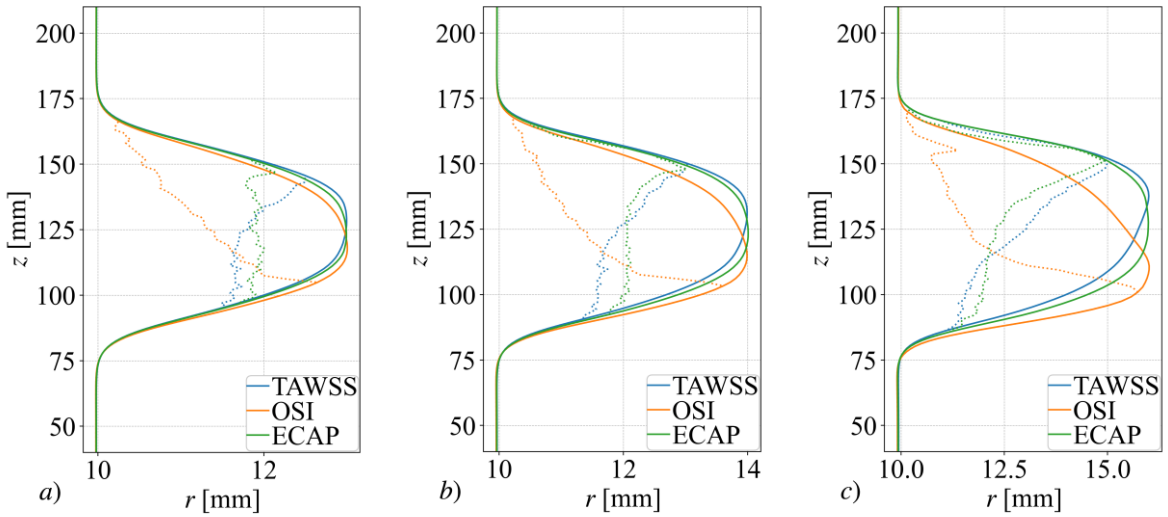

Figure 5.10 Inner and ILT contours for TAWSS, OSI and ECAP ILT deposition criteria when maximal inner diameter is *a*) r_{max}=13mm, *b*) r_{max}=15mm, *c*) r_{max}=16mm

Since the first inner radius r_{max} =13mm, a substantial difference in ILT deposition is evident between models. OSI tends to harbor ILT in the upper neck region, in contrast to TAWSS, which deposits ILT in the lower and central region. Additionally, due to the ILT location, there is a disparity in the inner wall contour. The OSI contour is slightly shifted downward because ILT impedes the expansion of the upper part of the wall. ECAP, being a combination of these two parameters, exhibits a location for ILT in between OSI and TAWSS. In Figure 5.10 *b*) and *c*), these observations persist but are more pronounced. In the moment when r_{max} =14 mm, ILT

becomes larger with no noticeable differences. However, the ILT shape for ECAP and TAWSS cases appears more similar than in Figure 5.10 *a*).

In Figure 5.10 *c*), when r_{max}=16mm, the difference between the models is the most prominent; the inner wall for OSI is noticeably shifted down due to ILT deposited in the upper neck region. Although TAWSS and ECAP ILT look similar, the inner wall is not the same. While ECAP is vertically centered, TAWSS is shifted upwards.

For these diameters, in the Figure 5.10 will be shown stress contours for all three models.

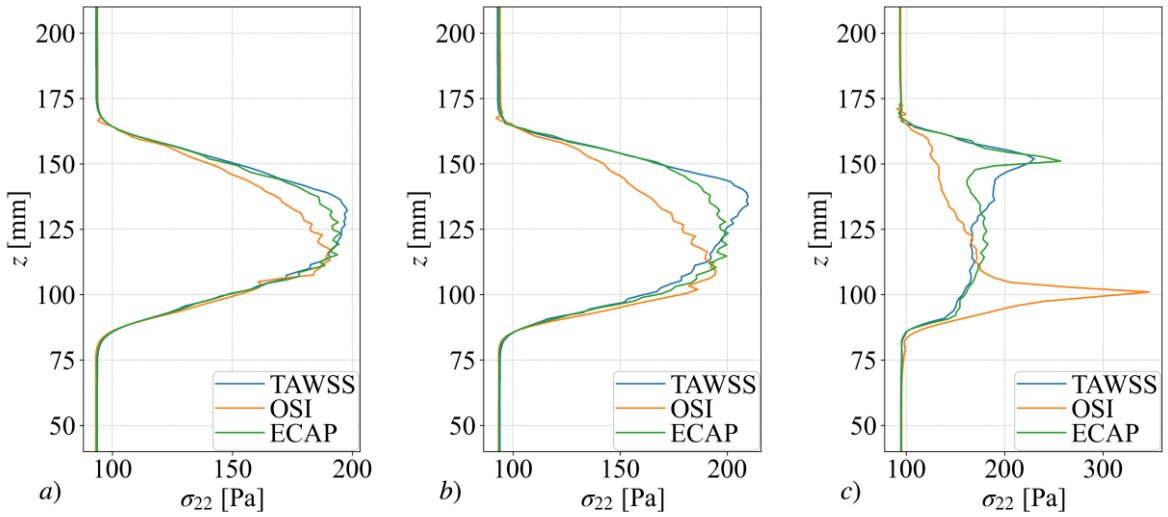

Figure 5.11 Stress contours for TAWSS, OSI and ECAP ILT deposition criteria when inner diameter is *a*) r_{max} =13mm, *b*) r_{max} =15mm, *c*) r_{max} =16mm

Deposited ILT reduces the stress value as it takes over part of the load from the wall. This phenomenon becomes more pronounced with time. In Figure 5.10 *a*), the difference is not as noticeable, while in Figure 5.10 *b*), the impact of ILT position is clearly seen. TAWSS and OSI have opposite stress distribution and maximal values. The TAWSS model has ILT deposited in the lower region, resulting in its maximal stress in the upper part of the aneurysm, and vice versa for the OSI model. Figure 5.10 *c*), shows an extreme case where the OSI model has maximal stress by far in the place where ILT is not deposited. This lower part can be

considered a critical point for the OSI case. In contrast, the critical point for TAWSS and ECAP cases is near the top of the neck region, at almost the same height of H=160mm.

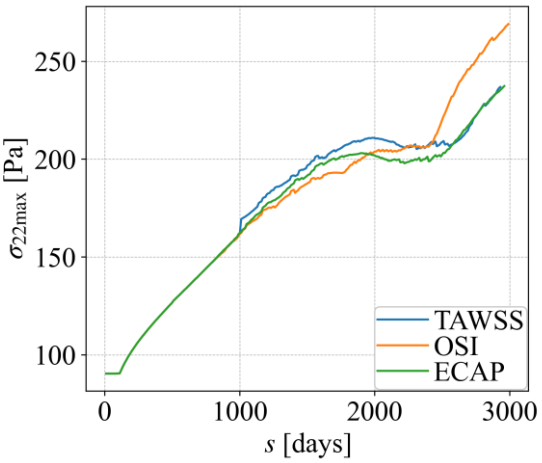

Figure 5.12 Maximal stress over time for TAWSS, OSI and ECAP parameters used as ILT deposition criteria.

All three cases exhibit similar stress distributions. Over the last 500 days, OSI shows higher stress values because the aneurysm did not deposit ILT in the lower region, unlike TAWSS and ECAP, which occurred along the entire inner wall. This observation is further illustrated in Figure 5.11 *c*).

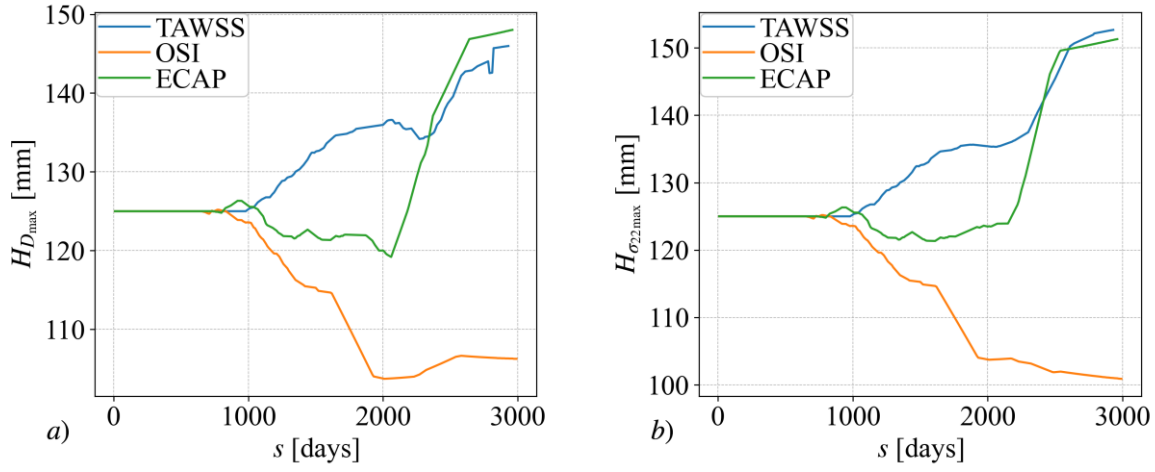

Figure 5.13 Maximal diameter height *a*), maximal circumferential stress *b*) over time for TAWSS, OSI and ECAP as ILT deposition parameter

In Figure 5.13 *a*) and *b*), $H_{D_{\max}}$ and $H_{\sigma_{22,\max}}$ exhibit very similar trends for all three cases. Therefore, it can be inferred that this pattern will persist across all models, once ILT initiation occurs and the growth direction remains unchanged. As anticipated, TAWSS and ECAP showcase opposite locations for maximal stress and diameter compared to the OSI case, as evident in both Figure 5.13 *a*) and *b*), as well as in the ILT and inner wall contour diagrams. However, between the 1000th and 2000th day, TAWSS and ECAP diverge. ECAP maintains nearly constant values for the height of $H_{D_{\max}}$ and $H_{\sigma_{22,\max}}$ while TAWSS experiences an increase over time. This discrepancy is also observable in contour diagrams for different maximal inner radii and time points.

5.6. Summary on FSG Parameters

In this chapter, the primary focus was on investigating the impact of various numerical model settings on disease development and numerical stability. Recognizing the potential for significant differences with even minor alterations, the chapter presented key indicators such as inner and ILT contours for early-stage AAA with ILT deposition and stress. These parameters provide valuable insights into the dynamic changes in diameter and ILT volume over time, playing a crucial role in guiding decisions related to patient treatment and predicting the disease's future course. The work further highlighted how factors such as the blood viscosity model, TAWSS threshold values, and the Δz_{MED} geometrical parameter influencing the AAA shape contribute to shaping the trajectory of the disease.

Before conclusion, it's crucial to acknowledge certain imperfections in the model. One notable limitation is the relatively large element size in FEAP. The presence of straight edges in the elements may lead to abrupt flow separations, whereas real-life AAAs typically have smooth surfaces without sharp edges. These elements could potentially yield unrealistic results, allowing ILT deposition to progress further than expected. Unfortunately, the incorporation of the entire G&R theory makes it impractical to refine the mesh. Consequently, it becomes essential to scrutinize the differences between model thresholds and assess their impact on the final stage of the simulation.

Rheology is indeed an exceedingly complex field, and a relatively simple viscosity model like Casson may struggle to reliably capture all the phenomena occurring in AAA. The intricacies of blood flow, intricately connected to ILT formation, pose challenges for any deposition criterion, introducing potential discrepancies. For instance, the ideal representation of ILT would be a cohesive mass without possible missing parts, a characteristic not met in cases such as TAWSS = 0.45 Pa. These intricacies highlight the need for more sophisticated models to better capture the nuanced behaviour of blood flow and ILT formation in AAA. A comprehensive comparison was conducted of the three most widely recognized ILT deposition criteria. This analysis posed considerable challenges, primarily stemming from the limited data available in the literature and the inherent complexity of our model, which integrates both G&R and CFD models. As demonstrated earlier, even subtle variations in CFD simulations can result in significant differences in outcomes. Furthermore, the mesh cannot be excessively refined due to computational constraints, further influencing the precision of the model.

Determining the blood viscosity model remains challenging due to its dependence on shear rate, which evolves over time. The analysis of two different geometries suggests that the most suitable viscosity model is Casson, as the shear rate falls within the Casson range. In the Newtonian model, viscosity is directly linked to wall-shear stress, and only a range of kinematic values $\nu = 3-6\cdot10^{-6}\,\mathrm{m^2/s}$ viscosity can be confirmed. However, even minor changes in the input parameters lead to substantial differences in TAWSS, making precise analysis challenging. Casson and Bird-Carreau models, falling between Newtonian models, exhibit notable differences in ILT volume and shape. The significant impact of viscosity models on the direction of AAA growth necessitates separate studies to obtain more accurate values. The viscosity regime introduces the most significant differences to the model. Turbulent flow, characterized by flow separations, alters wall shear stress values, and significantly affects ILT deposition. The challenge lies in determining the real viscosity intensity and its presence, given the perpetual changes in geometry during each G&R simulation. Despite these challenges, experimental examinations could provide valuable insights due to the varying ILT growth tendencies.

Determining whether turbulent or laminar flow prevails necessitates additional data, including experimental observations, as numerical models alone may exhibit significant differences. Following the initial ILT deposition, distinct growth patterns in height position emerge

turbulent models tend to foster ILT growth in the upper region, while laminar models promote growth in the lower region. Consequently, the maximal stress height varies significantly between these models, underscoring their divergence. When compared to the literature, Zambrano et al. [24] showed that ILT starts to deposit at the lower part of aneurysm and then spreads towards upper part, and that statement is closer to the results obtained from the turbulent model. It is noteworthy that the initial phases exhibit similarity, providing a solid foundation for the legitimacy of the model.

The example with geometrical parameter Δz_{MED}, explores the impact on AAA length on ILT output. Interestingly, varying this parameter has a minimal effect on ILT characteristics. While there is an observable difference in ILT volume, larger volumes in longer AAAs, the overall shape, deposition pattern, and location of ILT remain remarkably consistent across different AAA lengths. This underscores the resilience of ILT dynamics to changes in geometrical parameters, emphasizing the robustness of certain aspects of ILT behavior within the modeled scenarios.

The main assessment of the FSG model focused on examining the ILT deposition criteria and their respective threshold values. TAWSS, despite its simplicity, emerged as a robust and widely used ILT deposition parameter, providing a solid foundation for analysis. However, the study revealed that minor variations in TAWSS threshold values could yield significant changes in the model outcomes, due to the accumulation effect. The accepted threshold of 0.4 Pa demonstrated expectedly satisfactory results, effectively guiding ILT deposition. Notably, thrombus did not completely fill the lumen for the Casson viscosity model, even with higher threshold values like 0.45 Pa. Despite these challenges, the analysis offered crucial insights. Specifically, when TAWSS was employed as an ILT deposition criterion, it tended to concentrate ILT in the lower region of the AAA. In contrast, other ILT deposition criteria, such as OSI, exhibited the opposite trend, depositing ILT too far from the AAA center and healthy lumen—an occurrence deemed undesirable in any scenario. This underscores the importance of carefully selecting and fine-tuning ILT deposition criteria to ensure accurate and clinically relevant modeling outcomes.

The third ILT deposition criterion, ECAP, demonstrated highly promising results, standing out as a robust parameter for modelling ILT deposition. Notably, ECAP yielded outcomes that

resembled those obtained with TAWSS, particularly in the later stages of aneurysm growth. This suggests that ECAP, with its comprehensive consideration of both TAWSS and OSI influences, offers a balanced and insightful perspective on ILT deposition. The ILT shape observed under ECAP criteria aligns closely with the patterns seen in TAWSS, reinforcing its potential as a valuable criterion for accurate and clinically relevant modelling of intraluminal thrombus dynamics. ECAP emerged as the most comprehensive criterion among the three, effectively capturing the nuances of the ILT deposition process and providing the most insightful perspective. The results obtained with ECAP showcased its ability to closely align with TAWSS, emphasizing its potential as a valuable criterion for accurate and clinically relevant modelling of ILT dynamics in aneurysms.

Nevertheless, further investigation is needed due to different shape in the beginning of growth process. In this testing phase, several important conclusions have been brought. First is that OSI does not seem to be good ILT deposition parameter. ECAP and TAWSS shows good results and ILT shape has satisfactory form compared to literature. Before this thesis, there was no suggested thesis for ECAP threshold value, so we think that the value 1.54 should be a starting point as ECAP threshold.

Several common observations emerged from the variation of parameters. Firstly, the ILT consistently initiates its growth in the lower neck region of the aneurysm, aligning with existing literature. Regardless of the TAWSS threshold, the starting point of ILT remains constant. ILT progressively occupies the aneurysm from its origin upwards, avoiding intrusion into the healthy lumen area, a critical aspect in line with established knowledge. The ratio of ILT to aneurysm volume is influenced by the chosen TAWSS threshold. Additionally, local ILT thickness correlates with lower stress values, as the ILT assumes part of the stress from the blood vessel wall. The critical point, where there is a large radius and no ILT deposition, shifts upward over time, reflecting the growth tendency of ILT in the lower region of the aneurysm.

6. DISCUSSION AND CONCLUSION

6.1. Conclusion

Computational biomechanics is becoming increasingly important as a tool for investigation of complex phenomena in the field of vascular health. Use of computational analysis could give doctors and clinicians a huge advantage in better understanding the process of origin and development of disease. To account for the complexity of blood vessel behavior, a comprehensive model should incorporate a wide range of parameters, each carefully considered and integrated to accurately describe the vessel's behavior. Indeed, many parameters are needed to describe blood vessel constituents, which are embedded into matrix with its own prestretch coefficient, degradation, and production parameters etc. For example, collagen fibers are organized into bundles at different angels, in non-axisymmetric directions. The complex morphology of AAAs is mainly attributed to the elastin degradation process, characterized by a spatio-temporal function defined by multiple parameters. Also, perturbation of wall shear stress, caused by blood flow, has an impact on smooth muscle cells' active response. Most of the large AAAs contain ILT, whose deposition is predominantly influenced by blood flow image, with each aspect affecting the other in a reciprocal manner. Selecting the appropriate rheological model is critical in understanding the formation and deposition of ILT, which in turn influences the strength of blood vessels.

Although the scientific field of biomechanics is relatively new, there is a significant number of papers which describe several related topics. Introduction to G&R theory was given by Humphrey and Rajagopal, back in 2002. Substantial advancements have been made since then, yet there still isn't a comprehensive model that fully describes the behavior, origin, and development of AAA. This includes the lack of an integrative model that combines the numerical G&R of the blood vessel, CFD analysis of blood flow, and ILT deposition in accordance with the blood flow. Furthermore, a substantial gap in research lies in ILT deposition criteria, as the presently predominant metric, TAWSS, fails to offer comprehensive insights.

This thesis introduces a detailed 3D FSG model capable of describing the alterations in the aortic wall due to aging and various disease-related changes, with a focus on its application to the growth of AAA. Model considers G&R model of the wall and ILT, CFD analysis of blood flow and finding best possible criteria for ILT formation and deposition, based on several different blood flow parameters. In addition, the behavior of blood vessel and ILT must have incompressibility component. As previously mentioned, such a comprehensive model has not existed in literature up to this point and can be considered as a big advancement in our quest to unravel the intricacies of blood vessel behavior. To address the identified gap in research, an additional section discussing the influence of geometry on AAA rupture has been included. This section provides valuable insights into the shapes of AAAs that are more susceptible to rupture, enhancing our understanding of this critical aspect. This is particularly relevant since the most used criteria for assessing rupture risk are still the maximal diameter and clinicians' experience. Standard G&R parameters set was chosen, already used in published paper "The risk of rupture and abdominal aortic aneurysm morphology : A computational study" [13]. Most of them were kept constant to obtain results that are most relevant, while also minimizing excessive variations in the AAA growth process.

Various rheological models were tested in the CFD and FSG simulations, allowing for different settings. Ultimately, the Casson model was selected as the most suitable option among them. This finding is consistent with initial shear rate analyses, which reveal that blood flow in AAAs predominantly aligns with the characteristics of the Casson regime. In contrast, selecting an approximate Newtonian viscosity coefficient proves to be a challenging task due to geometry changes, which impact the viscosity coefficient value. For the second CFD model choice, there is an option to select either a laminar or turbulent model based on specific requirements. In this case, the turbulent model has shown to be appropriate choice. This decision was based on the observation, and although there was no significant pronounced difference in blood velocity in a single simulation case, there was a difference in ILT origin location, size, and shape between the two FSG models. Additionally, due to the optimal solver settings, computational efficiency was maintained without excessive demands, ensuring that the computational time was reasonable in terms of cost-benefit analysis.

The analysis of diverse ILT deposition criteria within the FSG model stands as the most significant contribution of this thesis, particularly due to the substantial gap in the field. While current models and studies predominantly rely on TAWSS as the sole parameter, this work aims

to build upon that foundation and broaden the scope of investigation in this area, challenging OSI and ECAP. OSI represents the oscillatory behavior that is very important in ILT formation according to Bhagavan [26]. ECAP is the ratio of OSI and TAWSS values and combines these two influences. However, the biggest challenge was that there is not any referent value in the literature for this ILT criteria that could be used in numerical simulations. After implementing criteria, the first step in the research was to examine severe values to get more detailed information. The process of comparison OSI and ECAP values to matching TAWSS critical values was guided according to ILT size, formation area and lately some literature experience. To match the TAWSS critical values of 0,4 Pa, referent value for OSI is 0.4575, and for ECAP 1,54. However, OSI has a bit different morphology than ECAP which is much more like TAWSS and other literature findings. The most significant disparity lies in the fact that the OSI tends to initiate aneurysm in the upper region, which is not the desirable and expected outcome. Given its broader applicability, ECAP should be regarded as a more suitable choice, as it demonstrates better alignment with other results and findings.

Although a lot of effort has been put into making the most comprehensive model possible, several existing limitations must be mentioned. The foremost concern lies in the model's lack of robustness. Its vulnerability primarily stems from the fact that even small parameter adjustments can lead to substantial discrepancies in the model's output. For instance, modifying the ILT deposition criteria threshold value results in significant variations in ILTs' volume and morphology, subsequently affecting the overall blood flow dynamics in CFD simulations. Furthermore, it's essential to acknowledge that neither TAWSS nor ECAP can be regarded as flawless criteria, indicating the need for the exploration of additional options. Similarly, alterations in the CFD rheology viscosity model, turbulence model, and sac shape parameters yield analogous disparities in the results. Moreover, it's important to note that the idealized geometry of the aortas used in the model does not accurately reflect the complexities of real-world anatomy, potentially leading to variations in the model's outcomes. Obtaining patient-specific geometry for each case is a labor-intensive process, requiring substantial time and effort. Nevertheless, achieving precise model parameters for these cases remains an impractical endeavor. In future research, a more nuanced and potentially combined set of rupture criteria could be explored, offering a more detailed and comprehensive analysis of ILT deposition. The implementation and addition of a biochemomechanical model could provide an even more comprehensive and expansive perspective. During this phase, it will be pivotal to validate theoretical models by comparing them with experiments conducted by clinicians, ensuring a

robust and clinically relevant foundation for the research. Following this validation process, the discussion of future steps and potential advancements in the research can be explored.

During the development of the FSG model, it became evident that there is a notable gap in research regarding rupture prediction parameters. This discovery underscores the necessity for more in-depth exploration in this field, particularly in applying the model to address a significant medical challenge that currently lacks practical and effective predictive solutions. By primarily relying on maximal diameter and clinicians' opinions as the key criteria for AAA rupture assessment, we aimed to introduce a fresh perspective grounded in numerical analysis. Considering a comprehensive list of 25 geometrical indices, which encompass AAA maximum diameter, length, volume, ILT volume, and various others, goal was to establish a more intricate indicator for AAA rupture, recognizing that a single criterion alone may not be sufficient. Through extensive simulations and data analysis, limitations of traditional geometric indices were revealed in predicting rupture and introduced new parameters: Geometrical rupture potential index (GRPI) and normalized aneurysmal length (NAL). Upon conducting an analysis, it became evident that both indices emerged as more reliable indicators for rupture, confirmed by statistical analysis. A limitation to mention is that the AAA cases analyzed in this study did not include ILT, which could have a notable impact on the rupture outcome and potentially introduce additional parameters for consideration. However, this study not only provides valuable insights into the matter but also unveils new possibilities for potential treatments and interventions, presenting opportunities for significant benefits.

In conclusion, this research endeavor delves deeply into the complexities of vascular health, biomechanics, and AAA rupture, guiding us towards a future enriched by innovative models and criteria that promise enhanced diagnostics and treatments. The meticulous exploration of numerical simulations, development of novel indices, and analysis of ILT deposition criteria have opened doors to unprecedented insights and solutions, contributing significantly to the evolving field of medical research and intervention. At the same time, the creation of this comprehensive model marks a substantial advancement in understanding AAA dynamics and lays a solid foundation for future refinements. However, to fully realize its potential, more detailed research, complemented by corresponding experimental examples, is essential.

6.2. Original scientific contribution

1. A 3D FSG numerical framework designed for simulating lesions, especially aneurysms, that incorporates ILT dynamics and incompressible behavior.
2. Analysis of ILT deposition parameters and their proposed critical values.
3. The introduction of two indicators for predicting aneurysm rupture, with a statistical analysis of their reliability and accuracy

BIBLIOGRAPHY

[1] A. J. Boyd, "Intraluminal thrombus: Innocent bystander or factor in abdominal aortic aneurysm pathogenesis?," *JVS Vasc. Sci.*, vol. 2, pp. 159–169, 2021, doi: 10.1016/j.jvssci.2021.02.001.

[2] E. Simão Da Silva, A. J. Rodrigues, E. Magalhães Castro De Tolosa, C. J. Rodrigues, G. Villas Boas Do Prado, and J. C. Nakamoto, "Morphology and diameter of infrarenal aortic aneurysms: A prospective autopsy study," *Cardiovasc. Surg.*, vol. 8, no. 7, pp. 526–532, 2000, doi: 10.1016/S0967-2109(00)00060-0.

[3] J. P. Vande Geest, D. E. Schmidt, M. S. Sacks, and D. A. Vorp, "The effects of anisotropy on the stress analyses of patient-specific abdominal aortic aneurysms," *Ann. Biomed. Eng.*, vol. 36, no. 6, pp. 921–932, 2008, doi: 10.1007/s10439-008-9490-3.

[4] J. Tong, T. Cohnert, P. Regitnig, and G. A. Holzapfel, "Effects of age on the elastic properties of the intraluminal thrombus and the thrombus-covered wall in abdominal aortic aneurysms: Biaxial extension behaviour and material modelling," *Eur. J. Vasc. Endovasc. Surg.*, vol. 42, no. 2, pp. 207–219, Aug. 2011, doi: 10.1016/j.ejvs.2011.02.017.

[5] J. Shum *et al.*, "Quantitative assessment of abdominal aortic aneurysm geometry," *Ann. Biomed. Eng.*, vol. 39, no. 1, pp. 277–286, 2011, doi: 10.1007/s10439-010-0175-3.

[6] E. K. Rodriguez, A. Hoger, and A. D. Mcculloch, "Stress-dependent finite growth in soft elastic tissues," *Pergamon .I. Biomchanics*, vol. 21, no. 4, pp. 455–467, 1994.

[7] J. D. Humphrey and K. R. Rajagopal, "A constrained mixture model for growth and remodelling of soft tissues," *Math. Model. Methods Appl. Sci.*, vol. 12, no. 03, pp. 407–430, 2002, doi: 10.1142/S0218202502001714.

[8] G. A. Holzapfel, "Computational Biomechanics of Soft Biological Tissue," *Encycl. Comput. Mech. Ed.*, vol. 2 Solids a, pp. 605–635, 2004, doi: 10.1002/0470091355.ecm041.

[9] S. Baek, A. Valentín, and J. D. Humphrey, "Biochemomechanics of cerebral vasospasm and its resolution: II. Constitutive relations and model simulations," *Ann. Biomed. Eng.*, vol. 35, no. 9, pp. 1498–1509, 2007, doi: 10.1007/s10439-007-9322-x.

[10] I. Karšaj, J. Sorić, and J. D. Humphrey, "A 3-D framework for arterial growth and remodeling in response to altered hemodynamics," *Int. J. Eng. Sci.*, vol. 48, no. 11, pp. 1357–1372, 2010, doi: 10.1016/j.ijengsci.2010.06.033.

[11] N. Horvat, L. Virag, G. A. Holzapfel, J. Sorić, and I. Karšaj, "A finite element implementation of a growth and remodeling model for soft biological tissues: Verification and application to abdominal aortic aneurysms," *Comput. Methods Appl. Mech. Eng.*, vol. 352, pp. 586–605, 2019, doi: 10.1016/j.cma.2019.04.041.

[12] N. Horvat, L. Virag, G. A. Holzapfel, and I. Karšaj, "Implementation of collagen fiber dispersion in a growth and remodeling model of arterial walls," *J. Mech. Phys. Solids*, vol. 153, p. 104498, Aug. 2021, doi: 10.1016/j.jmps.2021.104498.

[13] J. Živić, L. Virag, N. Horvat, and I. Karšaj, "The risk of rupture and abdominal aortic aneurysm morphology : A computational study," *Int J Numer Meth Biomed Engng*, vol. 38, no. 2, p. e3566, 2021, doi: 10.1002/cnm.3566.

[14] N. Horvat, L. Virag, and I. Karšaj, "Mechanical role of intraluminal thrombus in aneurysm growth: A computational study," *Biomech. Model. Mechanobiol.*, vol. 20, no. 5, pp. 1819–1832, 2021, doi: 10.1007/s10237-021-01478-w.

[15] C. J. Cyron, R. C. Aydin, and J. D. Humphrey, "A homogenized constrained mixture

(and mechanical analog) model for growth and remodeling of soft tissue," *Biomech. Model. Mechanobiol.*, vol. 15, no. 6, pp. 1389–1403, 2016, doi: 10.1007/s10237-016-0770-9.

[16] F. Inzoli *et al.*, "Biomechanical Factors in Abdominal Aortic Aneurysm Rupture," *Eur J Vasc Surg*, vol. 7, no. 6, pp. 667–674, Nov. 1993.

[17] D. H. J. Wang, M. S. Makaroun, M. W. Webster, and D. A. Vorp, "Effect of intraluminal thrombus on wall stress in patient-specific models of abdominal aortic aneurysm," *J. Vasc. Surg.*, vol. 36, no. 3, pp. 598–604, 2002, doi: 10.1067/mva.2002.126087.

[18] F. Ene *et al.*, "In vitro evaluation of the effects of intraluminal thrombus on abdominal aortic aneurysm wall dynamics," *Med. Eng. Phys.*, vol. 33, no. 8, pp. 957–966, 2011, doi: 10.1016/j.medengphy.2011.03.005.

[19] F. Riveros, G. Martufi, T. Gasser, and J. Rodriguez, "Influence of Intraluminal Thrombus Topology on AAA Passive Mechanics," *Comput. Cardiol. (2010).*, vol. 40, pp. 899–902, 2013.

[20] C. Behr-Rasmussen, N. Grondal, M. B. Bramsen, M. D. Thomsen, and J. S. Lindholt, "Mural thrombus and the progression of abdominal aortic aneurysms: A large population-based prospective cohort study," *Eur. J. Vasc. Endovasc. Surg.*, vol. 48, no. 3, pp. 301–307, 2014, doi: 10.1016/j.ejvs.2014.05.014.

[21] W. M. P. F. Bosman *et al.*, "Influence of aneurysm wall stiffness and the presence of intraluminal thrombus on the wall movement of an aneurysm - An in vitro study," *Vascular*, vol. 20, no. 4, pp. 203–209, 2012, doi: 10.1258/vasc.2011.oa0324.

[22] D. H. J. Wang *et al.*, "Mechanical Properties and Microstructure of Intraluminal Thrombus From Abdominal Aortic Aneurysm," *J. Biomech. Eng.*, vol. 123, no. 6, p. 536, Dec. 2001, doi: 10.1115/1.1411971.

[23] L. Virag, J. S. Wilson, J. D. Humphrey, and I. Karšaj, "A computational model of biochemomechanical effects of intraluminal thrombus on the enlargement of abdominal aortic aneurysms," *Ann. Biomed. Eng.*, vol. 43, no. 12, pp. 2852–2867, 2015, doi: 10.1007/s10439-015-1354-z.

[24] B. A. Zambrano *et al.*, "Association of Intraluminal Thrombus, Hemodynamic Forces, and Abdominal Aortic Aneurysm Expansion Using Longitudinal CT Images," *Ann. Biomed. Eng.*, vol. 44, no. 5, pp. 1502–1514, 2016, doi: 10.1007/s10439-015-1461-x.

[25] P. Di Achille, G. Tellides, C. A. Figueroa, and J. D. Humphrey, "A haemodynamic predictor of intraluminal thrombus formation in abdominal aortic aneurysms," *Proc. R. Soc. A Math. Phys. Eng. Sci.*, vol. 470, no. 2172, pp. 20140163–20140163, 2014, doi: 10.1098/rspa.2014.0163.

[26] D. Bhagavan, P. Di Achille, and J. D. Humphrey, "Strongly coupled morphological features of aortic aneurysms drive intraluminal thrombus," *Sci. Rep.*, vol. 8, no. 1, pp. 1–18, 2018, doi: 10.1038/s41598-018-31637-6.

[27] J. D. Humphrey and C. A. Taylor, "Intracranial and Abdominal Aortic Aneurysms: Similarities, Differences, and Need for a New Class of Computational Models," *Annu. Rev. Biomed. Eng.*, vol. 10, pp. 221–246, 2008, doi: 10.1146/annurev.bioeng.10.061807.160439.

[28] C. A. Figueroa *et al.*, "A Computational Framework for Fluid-Solid-Growth Modeling in Cardiovascular Simulations," *Comput Methods Appl Mech Eng*, vol. 198, no. 45–46, pp. 3583–3602, 2009, doi: 10.1016/j.cma.2008.09.013.

[29] P. N. Watton, N. B. Raberger, G. A. Holzapfel, and Y. Ventikos, "Coupling the Hemodynamic Environment to the Evolution of Cerebral Aneurysms: Computational Framework and Numerical Examples," *J. Biomech. Eng.*, vol. 131, no. 10, Oct. 2009, doi: 10.1115/1.3192141.

[30] J. Wu and S. C. Shadden, "Coupled simulation of hemodynamics and vascular growth

and remodeling in a subject-specific geometry," *Ann. Biomed. Eng.*, vol. 43, no. 7, pp. 1543–1554, 2015, doi: 10.1007/s10439-015-1287-6.

[31] A. Grytsan, P. N. Watton, and G. A. Holzapfel, "A thick-walled fluid–solid-growth model of abdominal aortic aneurysm evolution: application to a patient-specific geometry," *J. Biomech. Eng.*, vol. 137, no. 3, p. 031008, 2015, doi: 10.1115/1.4029279.

[32] A. Selimovic, Y. Ventikos, and P. N. Watton, "Modelling the evolution of cerebral aneurysms: Biomechanics, mechanobiology and multiscale modelling," *Procedia IUTAM*, vol. 10, pp. 396–409, 2013, doi: 10.1016/j.piutam.2014.01.034.

[33] F. S. Teixeira, E. Neufeld, N. Kuster, and P. N. Watton, "Modeling intracranial aneurysm stability and growth : an integrative mechanobiological framework for clinical cases," *Biomech. Model. Mechanobiol.*, vol. 19, no. 6, pp. 2413–2431, 2020, doi: 10.1007/s10237-020-01351-2.

[34] S. J. Mousavi *et al.*, "Coupling hemodynamics with mechanobiology in patient-specific computational models of ascending thoracic aortic aneurysms," *Comput. Methods Programs Biomed.*, vol. 205, p. 106107, 2021, doi: 10.1016/j.cmpb.2021.106107.

[35] M. Latorre, J. M. Szafron, A. B. Ramachandra, and J. D. Humphrey, "In vivo development of tissue engineered vascular grafts: a fluid-solid-growth model," *Biomech. Model. Mechanobiol.*, vol. 21, no. 3, pp. 827–848, 2022, doi: 10.1007/s10237-022-01562-9.

[36] H. Yamamoto, K. Kawamura, K. Omura, and S. Tokudome, "Development of a compact-sized falling needle rheometer for measurement of flow properties of fresh human blood," *Int. J. Thermophys.*, vol. 31, no. 11–12, pp. 2361–2379, 2010, doi: 10.1007/s10765-010-0842-5.

[37] T. C. Gasser, R. W. Ogden, and G. A. Holzapfel, "Hyperelastic modelling of arterial layers with distributed collagen fibre orientations," *J. R. Soc. Interface*, vol. 3, no. 6, pp. 15–35, 2006, doi: 10.1098/rsif.2005.0073.

[38] X. Houard *et al.*, "Retention and Activation of Blood-Borne Proteases in the Arterial Wall. Implications for Atherothrombosis," *Journal of the American College of Cardiology*, vol. 48, no. 9 SUPPL. pp. A3–9, 2006, doi: 10.1016/j.jacc.2006.04.098.

[39] C.-Y. Chen, R. Antón, M. Hung, P. Menon, E. A. Finol, and K. Pekkan, "Effects of Intraluminal Thrombus on Patient-Specific Abdominal Aortic Aneurysm Hemodynamics via Stereoscopic Particle Image Velocity and Computational Fluid Dynamics Modeling," *J. Biomech. Eng.*, vol. 136, no. 3, p. 031001, 2014, doi: 10.1115/1.4026160.

[40] I. Bijelonja, I. Demirdžić, and S. Muzaferija, "Mixed finite volume method for linear thermoelasticity at all Poisson's ratios," *Numer. Heat Transf. Part A Appl.*, vol. 72, no. 3, pp. 215–235, 2017, [Online]. Available: https://www.scopus.com/inward/record.uri?eid=2-s2.0-85029759877&doi=10.1080%2F10407782.2017.1372665&partnerID=40&md5=6131964ca2d2d7896770a51d62a3d620.

[41] R. Skalak, "Growth as A Finite Displacement Field," in *Proceed IUTAM Symposium Finite Elasticity*, 1981, pp. 347–355.

[42] J. S. Wilson, L. Virag, P. Di Achille, I. Karšaj, and J. D. Humphrey, "Biochemomechanics of Intraluminal Thrombus in Abdominal Aortic Aneurysms," *J. Biomech. Eng.*, vol. 135, no. 2, p. 021011, 2013, doi: 10.1115/1.4023437.

[43] D. J. A. Scott *et al.*, "Clot architecture is altered in abdominal aortic aneurysms and correlates with aneurysm size," *Arterioscler. Thromb. Vasc. Biol.*, vol. 31, no. 12, pp. 3004–3010, Dec. 2011, doi: 10.1161/ATVBAHA.111.236786.

[44] J. P. Vande Geest, M. S. Sacks, and D. A. Vorp, "A planar biaxial constitutive relation for the luminal layer of intra-luminal thrombus in abdominal aortic aneurysms," *J.*

Biomech., vol. 39, no. 13, pp. 2347–2354, Jan. 2006, doi: 10.1016/j.jbiomech.2006.05.011.

[45] M. J. O'Rourke, J. P. McCullough, and S. Kelly, "An investigation of the relationship between hemodynamics and thrombus deposition within patient-specific models of abdominal aortic aneurysm," *Proc. Inst. Mech. Eng. Part H J. Eng. Med.*, vol. 226, no. 7, pp. 548–564, 2012, doi: 10.1177/0954411912444080.

[46] J. Biasetti, F. Hussain, and T. C. Gasser, "Blood flow and coherent vortices in the normal and aneurysmatic aortas: a fluid dynamical approach to intra-luminal thrombus formation," *J. R. Soc. Interface*, vol. 8, pp. 1449–1461, 2011, doi: 10.1098/rsif.2011.0041.

[47] J. T. Willerson, "Inflammation as a Cardiovascular Risk Factor," *Circulation*, vol. 109, no. 21_suppl_1, pp. II-2-II–10, 2004, doi: 10.1161/01.CIR.0000129535.04194.38.

[48] A. M. Malek and S. L. Alper, "Hemodynamic Shear Stress and Its Role in Atherosclerosis," *JAMA*, vol. 282, no. 21, pp. 2035–2042, 1999.

[49] S. C. Shadden and S. Hendabadi, "Potential fluid mechanic pathways of platelet activation," *Biomech Model Mechanobiol*, vol. 12, pp. 467–474, 2013, doi: 10.1007/s10237-012-0417-4.

[50] A. Arzani, G.-Y. Suh, R. L. Dalman, and S. C. Shadden, "A longitudinal comparison of hemodynamics and intraluminal thrombus deposition in abdominal aortic aneurysms," *Am. J. Physiol. Circ. Physiol.*, vol. 307, no. 12, pp. H1786–H1795, 2014, doi: 10.1152/ajpheart.00461.2014.

[51] K. Tzirakis, Y. Kamarianakis, E. Metaxa, N. Kontopodis, C. V. Ioannou, and Y. Papaharilaou, "A robust approach for exploring hemodynamics and thrombus growth associations in abdominal aortic aneurysms," *Med. Biol. Eng. Comput.*, vol. 55, no. 8, pp. 1493–1506, 2017, doi: 10.1007/s11517-016-1610-x.

[52] P. Di Achille, G. Tellides, and J. D. Humphrey, "Hemodynamics-driven deposition of intraluminal thrombus in abdominal aortic aneurysms," *Int. j. numer. method. biomed. eng.*, vol. 33, no. 5, pp. 1–17, 2017, doi: 10.1002/cnm.2828.

[53] A. Sheidaei, S. C. Hunley, S. Zeinali-Davarani, L. G. Raguin, and S. Baek, "Simulation of abdominal aortic aneurysm growth with updating hemodynamic loads using a realistic geometry," *Med. Eng. Phys.*, vol. 33, no. 1, pp. 80–88, 2011, doi: 10.1016/j.medengphy.2010.09.012.

[54] R. Virmani *et al.*, "Effect of Aging on Aortic Morphology in Populations with High and Low Prevalence of Hypertension and Atherosclerosis Comparison Between Occidental and Chinese Communities," *Am. J. Pathol.*, vol. 139, no. 5, pp. 1119–1129, 1991.

[55] A. Grytsan, T. S. E. Eriksson, P. N. Watton, and T. C. Gasser, "Growth description for vessel wall adaptation: a thick-walled mixture model of abdominal aortic aneurysm evolution," *Materials (Basel).*, vol. 10, no. 9, p. e994, 2017, doi: 10.3390/ma10090994.

[56] J. S. Wilson, S. Baek, and J. D. Humphrey, "Parametric study of effects of collagen turnover on the natural history of abdominal aortic aneurysms," *Proc. R. Soc. A Math. Phys. Eng. Sci.*, vol. 469, no. 2150, p. 20120556, 2012, doi: 10.1098/rspa.2012.0556.

[57] P. Matusik, P. Mazur, E. Stępień, R. Pfitzner, J. Sadowski, and A. Undas, "Architecture of intraluminal thrombus removed from abdominal aortic aneurysm," *J. Thromb. Thrombolysis*, vol. 30, pp. 7–9, 2010, doi: 10.1007/s11239-009-0430-3.

[58] R. Taylor, "FEAP - Finite Element Analysis Program, Version 8.4." University of California at Berkeley, Berkeley (CA)., 2013.

[59] N. Horvat, L. Virag, and I. Karšaj, "Finite Element Growth Model of Abdominal Aortic Aneurysm," in *Proceedings of the 9th International Congress of Croatian Society of Mechanics*, 2018.

[60] "K. Siau: 'Composition of blood', retrieved from

https://twitter.com/drkeithsiau/status/1435631529372393476."
[61] "Encyclopedia Britannica, Blood anatomy, retrieved from https://www.britannica.com/science/heart."
[62] A. Skiadopoulos, P. Neofytou, and C. Housiadas, "Comparison of blood rheological models in patient specific cardiovascular system simulations," *J. Hydrodyn.*, vol. 29, no. 2, pp. 293–304, 2017, doi: 10.1016/S1001-6058(16)60739-4.
[63] D. Liepsch, S. Sindeev, and S. Frolov, "An impact of non-Newtonian blood viscosity on hemodynamics in a patient-specific model of a cerebral aneurysm," *J. Phys. Conf. Ser.*, vol. 1084, no. 1, 2018, doi: 10.1088/1742-6596/1084/1/012001.
[64] A. Fuchs, N. Berg, and L. Prahl Wittberg, "Blood rheology modeling effects in aortic flow simulations," no. 2012, pp. 1–19, 2020.
[65] J. B. Mendieta *et al.*, "The importance of blood rheology in patient-specific computational fluid dynamics simulation of stenotic carotid arteries," *Biomech. Model. Mechanobiol.*, vol. 19, no. 5, pp. 1477–1490, 2020, doi: 10.1007/s10237-019-01282-7.
[66] R. Agarwal, A. Sarkar, S. Paul, and S. Chakraborty, "A portable rotating disc as blood rheometer," *Biomicrofluidics*, vol. 13, no. 6, 2019, doi: 10.1063/1.5128937.
[67] H. G. Weller, G. Tabor, H. Jasak, and C. Fureby, "techniques A tensorial approach to computational continuum mechanics using object-oriented techniques," vol. 12, no. 620, 1998, doi: 10.1063/1.168744.
[68] C. Greenshields, "OpenFOAM: user guide version 6," *OpenFOAM Found. Ltd*, vol. 6, no. 10th, p. 237, 2018, [Online]. Available: https://cfd.direct/openfoam/user-guide/.
[69] M. J. Collins and H. Shuman, "Prediction of transient wall movement of an incompressible elastic tube using a finite volume procedure," *WIT Trans. Biomed. Heal.*, vol. 1, 1993.
[70] I. Karšaj and J. D. Humphrey, "A multilayered wall model of arterial growth and remodeling," *Mech. Mater.*, vol. 44, pp. 110–119, 2012, doi: 10.1016/j.mechmat.2011.05.006.
[71] Ž. Tuković and H. Jasak, "Updated Lagrangian finite volume solver for large deformation dynamic response of elastic body," *Trans. Famena*, 2007.
[72] C. B. Washington, J. Shum, S. C. Muluk, and E. A. Finol, "The Association of Wall Mechanics and Morphology: A Case Study of Abdominal Aortic Aneurysm Growth," *J. Biomech. Eng.*, vol. 133, no. 10, p. 104501, 2011, doi: 10.1115/1.4005176.
[73] F. A. M. V. I. Hellenthal, W. A. Buurman, W. K. W. H. Wodzig, and G. W. H. Schurink, "Biomarkers of abdominal aortic aneurysm progression. Part 2: inflammation," *Nat. Rev. Cardiol.*, vol. 6, pp. 543–552, 2009, doi: 10.1038/nrcardio.2009.102.
[74] J. A. Tavares Monteiro, E. S. Da Silva, M. L. Raghavan, P. Puech-Leão, M. De Lourdes Higuchi, and J. P. Otoch, "Histologic, histochemical, and biomechanical properties of fragments isolated from the anterior wall of abdominal aortic aneurysms," *J. Vasc. Surg.*, vol. 59, no. 5, 2014, doi: 10.1016/j.jvs.2013.04.064.
[75] J. A. Niestrawska, P. Regitnig, C. Viertler, T. U. Cohnert, A. R. Babu, and G. A. Holzapfel, "The role of tissue remodeling in mechanics and pathogenesis of abdominal aortic aneurysms," *Acta Biomater.*, vol. 88, no. xxxx, pp. 149–161, 2019, doi: 10.1016/j.actbio.2019.01.070.
[76] F. A. M. V. I. Hellenthal, W. A. Buurman, W. K. W. H. Wodzig, and G. W. H. Schurink, "Biomarkers of AAA progression. Part 1: extracellular matrix degeneration," *Nat. Rev. Cardiol.*, vol. 6, pp. 464–474, 2009, doi: 10.1038/nrcardio.2009.80.
[77] J. H. N. Lindeman, T. J. Rabelink, and J. H. Van Bockel, "Immunosuppression and the abdominal aortic aneurysm: Doctor jekyll or mister hyde?," *Circulation*, vol. 124, no. 18, pp. 3–6, 2011, doi: 10.1161/CIRCULATIONAHA.110.008573.
[78] S. S. Hans, O. Jareunpoon, M. Balasubramaniam, and G. B. Zelenock, "Size and location

of thrombus in intact and ruptured abdominal aortic aneurysms," *J. Vasc. Surg.*, vol. 41, no. 4, pp. 584–588, 2005, doi: 10.1016/j.jvs.2005.01.004.

[79] A. Parr, M. McCann, B. Bradshaw, A. Shahzad, P. Buttner, and J. Golledge, "Thrombus volume is associated with cardiovascular events and aneurysm growth in patients who have abdominal aortic aneurysms," *J. Vasc. Surg.*, vol. 53, no. 1, pp. 28–35, 2011, doi: 10.1016/j.jvs.2010.08.013.

[80] J. Golledge, V. Iyer, J. Jenkins, B. Bradshaw, O. Cronin, and P. J. Walker, "Thrombus volume is similar in patients with ruptured and intact abdominal aortic aneurysms," *J. Vasc. Surg.*, vol. 59, no. 2, pp. 315–320, 2014, doi: 10.1016/j.jvs.2013.08.036.

[81] D. A. Vorp *et al.*, "Association of intraluminal thrombus in abdominal aortic aneurysm with local hypoxia and wall weakening," *J. Vasc. Surg.*, vol. 34, no. 2, pp. 291–299, 2001, doi: 10.1067/mva.2001.114813.

[82] A. Domonkos, R. Staffa, and L. Kubíček, "Effect of intraluminal thrombus on growth rate of abdominal aortic aneurysms," *Int. Angiol.*, vol. 38, no. 1, pp. 39–45, 2019, doi: 10.23736/S0392-9590.18.04006-3.

[83] J. Shum, A. Xu, I. Chatnuntawech, and E. A. Finol, "A framework for the automatic generation of surface topologies for abdominal aortic aneurysm models," *Ann. Biomed. Eng.*, vol. 39, no. 1, pp. 249–259, 2011, doi: 10.1007/s10439-010-0165-5.

[84] A. Kitagawa, T. M. Mastracci, R. Von Allmen, and J. T. Powell, "The role of diameter versus volume as the best prognostic measurement of abdominal aortic aneurysms," *J. Vasc. Surg.*, vol. 58, no. 1, pp. 258–265, 2013, doi: 10.1016/j.jvs.2013.05.001.

[85] M. L. L. Raghavan, D. A. Vorp, M. P. Federle, M. S. Makaroun, and M. W. Webster, "Wall stress distribution on three-dimensionally reconstructed models of human abdominal aortic aneurysm," *J. Vasc. Surg.*, vol. 31, no. 4, pp. 760–769, 2000, doi: 10.1067/mva.2000.103971.

[86] J. Tong, T. Cohnert, and G. A. Holzapfel, "Diameter-related variations of geometrical, mechanical, and mass fraction data in the anterior portion of abdominal aortic aneurysms," *Eur. J. Vasc. Endovasc. Surg.*, vol. 49, no. 3, pp. 262–270, 2015, doi: 10.1016/j.ejvs.2014.12.009.

[87] D. A. Vorp and J. P. Vande Geest, "Biomechanical determinants of abdominal aortic aneurysm rupture," *Arterioscler. Thromb. Vasc. Biol.*, vol. 25, pp. 1558–1566, 2005, doi: 10.1161/01.ATV.0000174129.77391.55.

[88] J. P. Vande Geest, E. S. Di Martino, A. Bohra, M. S. Makaroun, and D. A. Vorp, "A biomechanics-based rupture potential index for abdominal aortic aneurysm risk assessment: Demonstrative application," *Ann. N. Y. Acad. Sci.*, vol. 1085, pp. 11–21, 2006, doi: 10.1196/annals.1383.046.

[89] M. Xenos and D. Bluestein, "Biomechanical Aspects of Abdominal Aortic Aneurysm (AAA) and its Risk of Rupture: Fluid Structure Interaction (FSI) Studies," *FSI Stud. AAA Biomech.*, pp. 181–220, 2011, doi: 10.1007/8415_2011_72.

[90] J. D. Humphrey, "Constrained Mixture Models of Soft Tissue Growth and Remodeling – Twenty Years After," *J. Elast.*, vol. 145, no. 1–2, pp. 49–75, 2021, doi: 10.1007/s10659-020-09809-1.

[91] A. Valentín and J. D. Humphrey, "Parameter sensitivity study of a constrained mixture model of arterial growth and remodeling," *J. Biomech. Eng.*, vol. 131, no. 10, p. 101006, 2009, doi: 10.1115/1.3192144.

[92] J. S. Wilson, S. Baek, and J. D. Humphrey, "Importance of initial aortic properties on the evolving regional anisotropy, stiffness and wall thickness of human abdominal aortic aneurysms," *J. R. Soc. Interface*, vol. 9, no. 74, pp. 2047–2058, 2012, doi: 10.1098/rsif.2012.0097.

[93] R. L. Taylor, "A Finite Element Analysis Program, Version 8.4." University of

California: Berkeley, 2014.
[94] S. M. Arribas, A. Hinek, and M. C. González, "Elastic fibres and vascular structure in hypertension," *Pharmacol. Ther.*, vol. 111, pp. 771–791, 2006, doi: 10.1016/j.pharmthera.2005.12.003.
[95] F. A. Braeu, A. Seitz, R. C. Aydin, and C. J. Cyron, "Homogenized constrained mixture models for anisotropic volumetric growth and remodeling," *Biomech. Model. Mechanobiol.*, vol. 16, no. 3, pp. 889–906, 2017, doi: 10.1007/s10237-016-0859-1.
[96] W. J. Lin, M. D. Iafrati, R. A. Peattie, and L. Dorfmann, "Growth and remodeling with application to abdominal aortic aneurysms," *J. Eng. Math.*, vol. 109, no. 1, pp. 113–137, 2017, doi: 10.1007/s10665-017-9915-9.
[97] J. Tong *et al.*, "Variations of dissection properties and mass fractions with thrombus age in human abdominal aortic aneurysms," *J. Biomech.*, vol. 47, no. 1, pp. 14–23, 2014, doi: 10.1016/j.jbiomech.2013.10.027.
[98] A. Valentin *et al.*, "Complementary vasoactivity and matrix remodelling in arterial adaptations to altered flow and pressure," *J. R. Soc. Interface*, vol. 6, no. 32, pp. 293–306, 2009, doi: 10.1098/rsif.2008.0254.
[99] A. Burke and G. A. FitzGerald, "Oxidative stress and smoking-induced vascular injury," *Prog. Cardiovasc. Dis.*, vol. 46, no. 1, pp. 79–90, 2003, doi: 10.1016/S0033-0620(03)00076-8.
[100] J. T. Powell, "Vascular damage from smoking: disease mechanisms at the arterial wall.," *Vasc. Med.*, vol. 3, no. 1, pp. 21–28, 1998, doi: 10.1191/135886398670269973.
[101] T. Länne *et al.*, "Diameter and compliance in the male human abdominal aorta: influence of age and aortic aneurysm," *Eur J Vasc Surg*, vol. 6, pp. 178–184, 1992.
[102] S. S. Yang and W. S. Yun, "Changes in the normal infrarenal aortic length and tortuosity in elderly people," *Vasc. Spec. Int.*, vol. 36, no. 1, pp. 15–20, 2020, doi: 10.5758/vsi.2020.36.1.15.
[103] S. Brandstaeter, S. L. Fuchs, J. Biehler, R. C. Aydin, W. A. Wall, and C. J. Cyron, "Global Sensitivity Analysis of a Homogenized Constrained Mixture Model of Arterial Growth and Remodeling," *J. Elast.*, vol. 145, no. 1–2, pp. 191–221, 2021, doi: 10.1007/s10659-021-09833-9.
[104] A. A. Ahimastos, M. Formosa, A. M. Dart, and B. A. Kingwell, "Gender Differences in Large Artery Stiffness Pre- and Post Puberty," *J. Clin. Endocrinol. Metab.*, vol. 88, no. 11, pp. 5375–5380, 2003, doi: 10.1210/jc.2003-030722.
[105] G. Martufi, E. S. Di Martino, C. H. Amon, S. C. Muluk, and E. A. Finol, "Three-Dimensional Geometrical Characterization of Abdominal Aortic Aneurysms: Image-Based Wall Thickness Distribution," *J. Biomech. Eng.*, vol. 131, no. 6, p. 061015, 2009, doi: 10.1115/1.3127256.
[106] J. Shum *et al.*, "Semiautomatic vessel wall detection and quantification of wall thickness in computed tomography images of human abdominal aortic aneurysms," *Med. Phys.*, vol. 37, no. 2, pp. 638–648, 2010, doi: 10.1118/1.3284976.
[107] N. Horvat, B. Zambrano, S. Baek, and I. Karšaj, "Numerical modeling of fluid solid growth in abdominal aortic aneurysm," in *Proceedings of 5th International Conference on Computational and Mathematical Biomedical Engineering*, 2017, pp. 172–175.

BIOGRAPHY

Josip Živić was born in 1993 in Slavonski Brod, Croatia. He completed secondary school, Gymnasium "Matija Mesić" in Slavonski Brod in 2012, then entered the Faculty of Mechanical Engineering and Naval Architecture at the University of Zagreb. He obtained a Bachelor of Mechanical Engineering degree in 2015 and a Master of Mechanical Engineering degree in 2018.

After obtaining his master's degree, he began working at the Faculty of Mechanical Engineering and Naval Architecture as a project assistant on the "Model rasta aneurizme temeljen na biokemijskim i mehaničkim podražajima" project, and later on the "Eksperimentalna platforma za simulaciju endovaskularnog liječenja intrakranijskih aneurizmi". He also enrolled in doctoral studies at the Faculty of Mechanical Engineering and Naval Architecture at the University of Zagreb.

He has authored a scientific journal article and presented seven papers at international conferences. As part of his doctoral work, he attended two doctoral workshops at the Faculty of Mechanical Engineering and Naval Architecture and participated in two international summer schools organized by the University of Barcelona and Frankfurt University of Applied Science.

Scientific papers:

a) Papers referenced in CC/SCI (WoS)

- Živić, J; Virag, L; Horvat; Smoljkić, M; N; Karšaj, I (2021) *The risk of rupture and abdominal aortic aneurysm morphology : A computational study*, International Journal for Numerical Methods in Biomedical Engineering, vol. 38, no. 2, p. e3566, 2021, doi: 10.1002/cnm.3566.

b) Conference papers

- Živić, J.; Horvat, N.; Karšaj, I.; (2022) *Fluid-Solid-Growth model of thrombus deposited Abdominal Aortic Aneurysm.* Euromech Colloquium 627 "Current challenges in soft tissue mechanics" Njemačka, Frankfurt am Main, summary, oral presentation.
- Živić, J.1; Virag, L.; Horvat, N.; Smoljkić, M.; Karšaj, I. (2021) *Rizik rupture i morfologija aneurizme abdominalne aorte*, 11. susret Hrvatskog društva za mehaniku, Rijeka, Hrvatska, summary, oral presentation.
- Živić, J.; Batistić, I.; Horvat, N.; Karšaj, I. (2020) *Modeliranje strujanja u aneurizmatičnoj abdominalnoj aorti korištenjem metode kontrolnih volumena*, 10. susret Hrvatskog društva za mehaniku, Zagreb, Hrvatska, summary, oral presentation
- Živić J.; Karšaj I. (2019), *Biochemomechanical Finite Volume Model of Dissecting Aorta*, 5th Annual FAMENAPhD Workshop, Zagreb, Hrvatska, summary, oral presentation.
- Živić, J.; Batistić, I.; Tuković, Ž.; Karšaj, I., (2019) *Modeliranje nestlačivosti metodom kontrolnih volumena i njena primjena u području biomehanike*, 9. susret Hrvatskog društva za mehaniku, Zagreb, Hrvatska, summary, oral presentation.
- Živić, J.; Tomić, Z.; Škugor, T.; Smoljkić, M.; Karšaj, I., (2019) *Towards mechanically realistic 3D printed arterial replicas*, MPLAS 2019: XV International Conference on Computational Plasticity, Barcelona, Spain, summary, oral presentation.